



Review

On the Exploitation of Remote Sensing Technologies for the Monitoring of Coastal and River Delta Regions

Qing Zhao ^{1,2,3,*} , Jiayi Pan ^{4,5,6} , Adam Thomas Devlin ^{4,5,6}, Maochuan Tang ^{1,2,3}, Chengfang Yao ^{1,2,3}, Virginia Zamparelli ⁷ , Francesco Falabella ^{7,8,9} and Antonio Pepe ⁷

- ¹ Key Laboratory of Geographical Information Science, Ministry of Education, East China Normal University, Shanghai 200241, China; 51193901043@stu.ecnu.edu.cn (M.T.); mliu@geo.ecnu.edu.cn (C.Y.)
 - ² School of Geographic Sciences, East China Normal University, Shanghai 200241, China
 - ³ Key Laboratory of Spatial-Temporal Big Data Analysis and Application of Natural Resources in Megacities, Ministry of Natural Resources, Shanghai 200241, China
 - ⁴ Key Laboratory of Poyang Lake Wetland and Watershed Research of Ministry of Education, Nanchang 330022, China; panj@cuhk.edu.hk (J.P.); atdevlin@jxnu.edu.cn (A.T.D.)
 - ⁵ School of Geography and Environment, Jiangxi Normal University, Nanchang 330022, China
 - ⁶ Institute of Space and Earth Information Science, The Chinese University of Hong Kong, Shatin, Hong Kong, China
 - ⁷ Institute for Electromagnetic Sensing of the Environment (IREA), Italian National Research Council, 328, Diocleziano, 80124 Napoli, Italy; zamparelli.v@irea.cnr.it (V.Z.); pepe.a@irea.cnr.it (A.P.)
 - ⁸ Institute of Methodologies for Environmental Analysis (IMAA), Italian National Research Council, Tito Scalo, 85050 Potenza, Italy
 - ⁹ School of Engineering, University of Basilicata, 85100 Potenza, Italy; francesco.falabella@unibas.it
- * Correspondence: qzhao@geo.ecnu.edu.cn; Tel.: +86-21-62224459



Citation: Zhao, Q.; Pan, J.; Devlin, A.T.; Tang, M.; Yao, C.; Zamparelli, V.; Falabella, F.; Pepe, A. On the Exploitation of Remote Sensing Technologies for the Monitoring of Coastal and River Delta Regions. *Remote Sens.* **2022**, *14*, 2384. <https://doi.org/10.3390/rs14102384>

Academic Editors: Halina Kaczmarek and Manon Besset

Received: 8 March 2022

Accepted: 10 May 2022

Published: 16 May 2022

Publisher's Note: MDPI stays neutral with regard to jurisdictional claims in published maps and institutional affiliations.



Copyright: © 2022 by the authors. Licensee MDPI, Basel, Switzerland. This article is an open access article distributed under the terms and conditions of the Creative Commons Attribution (CC BY) license (<https://creativecommons.org/licenses/by/4.0/>).

Abstract: Remote sensing technologies are extensively applied to prevent, monitor, and forecast hazardous risk conditions in the present-day global climate change era. This paper presents an overview of the current stage of remote sensing approaches employed to study coastal and delta river regions. The advantages and limitations of Earth Observation technology in characterizing the effects of climate variations on coastal environments are also presented. The role of the constellations of satellite sensors for Earth Observation, collecting helpful information on the Earth's system and its temporal changes, is emphasized. For some key technologies, the principal characteristics of the processing chains adopted to obtain from the collected raw data added-value products are summarized. Emphasis is put on studying various disaster risks that affect coastal and megacity areas, where heterogeneous and interlinked hazard conditions can severely affect the population.

Keywords: Earth Observation; remote sensing; coastal regions; river deltas; disaster risk management

1. Introduction

Coastal regions are essential for the socio-economic well-being of many nations [1–4]. Low-elevation coastal zones within 10-m topographic relief contain about 10% of the Earth's population, and 44% of the population lives within 150 km of the coast, with a density expected to grow about 25% by 2050. Coastal areas are often large population centers with multiple uses, needs, and opportunities. They are particularly exposed to extreme natural and anthropogenically driven disaster phenomena exacerbated by global climate change [5–11]. Many vital sectors are affected by long-term effects in these zones, such as monitoring of public/private infrastructures, cultural/natural heritage preservation, risk management, and agriculture. The cumulative effect of sea level rise (SLR) [12–26], tidal evolution [27–30], and modulated ocean currents and extreme events [31–36] can have numerous impacts on coasts, river deltas and inland water zones, including water management, which can also lead to unpredictable effects on other sectors. As sea level

increases globally, tides have also shown worldwide changes. These risks are accompanied by concerns about the increasing urbanization of coastal regions and related hazards (e.g., tidal-induced nuisance flooding, storm surge). The global sea level has drastically risen during the last century and is expected to increase and possibly accelerate by at least ~60 cm by 2100 because of ocean warming and glacier melt, but these projections are spatially dependent, and some regions may expect larger increases [37,38]. Projections of future sea-level-rise (SLR) at any coastal location of the world up until the year 2150 under various Shared Socioeconomic Pathway (SSP) scenarios as determined by the IPCC Sixth Assessment Report can be interactively explored using the NASA Sea Level Projection Tool (<https://sealevel.nasa.gov/ipcc-ar6-sea-level-projection-tool>) (accessed on 1 January 2021). SLR results in negative impacts, including coastal erosion [39–41], flooding [42–44], freshwater salinization [45–47], and wetland loss [48]. However, SLR is not uniformly spatially distributed [49,50] and, consequently, vertical rates of ground subsidence coupled with global SLR pose variable hazards and risks for many coastal population centers. Moreover, anthropogenic processes (e.g., land subsidence connected to groundwater extraction [51], the effects of large land reclamation projects [52], the presence of artificial seawalls) and natural hazards (e.g., storms and storm surge, cyclones and hurricanes, extreme precipitation and flooding) exacerbate the disaster risks in coastal zones and coastal cities, amplifying the vulnerability of the local population. Thus, a detailed understanding of the combined risk of SLR, tidal evolution, storm surge, and ground subsidence in river deltas and coastal regions is of great relevance for reducing disaster risk and fostering resilience.

Earth Observation (EO) technologies (e.g., [52–66]) have been proven to be highly useful for obtaining consistent and frequently updated information on environmental conditions and their temporal variations. Several works have encompassed the study of the atmosphere [67–69], the ground surface [62,70–76], and the sea [77–79]. The products of these investigations can help monitor the evolution of natural and anthropogenic calamities that affect the population and help local authorities and the national governments design, maintain, and manage effective disaster plans. Disaster management [80–85] aims to limit the effects of potential losses from hazards, guarantee timely support to victims of disasters, and accomplish a rapid and effective recovery. It is well known that an effective disaster management cycle is composed of four main phases [86–89]: mitigation and preparedness, which occur before a disaster, and response and recovery, which happen after the occurrence of a disaster. The availability of spatially distributed data concerning the potential conditions of risk and the knowledge of the technologies used to recover these data is strategic for making societies more resilient to natural, anthropogenic, and technological disasters. In this framework, the need to collect, process, and interpret large amounts of data to obtain synthetic but comprehensive indicators of the state of a society that is subject to multi-hazard risks is crucial [90,91]. Spatial Data Infrastructures (SDI) [92,93] have been established to overcome some of the shortcomings related to a specific data source, improve data sharing, and develop technologies and standards used by disaster management officers.

EO technologies play a significant role in all disaster phases, especially in the mitigation and preparedness ones, by guaranteeing the development of extended investigations on the state of the observed scenes, searching for precursor signals of potential disasters, and forecasting future evolutions of natural phenomena, and for identifying critical conditions. Constellations of satellite sensors working from microwave to optical wavelengths are systematically used to monitor changes in the Earth system and obtain valuable information about the critical needs. The interest in the analysis of Earth's environment through EO systems is also testified by the increased number of publications over the last 25 years which address the use of EO methods for disaster risk management, especially for coastal regions.

This paper addresses current state-of-the-art RS technologies that can be exploited to detect changes in coastal environments and study their interactions with sea surface characteristics and global ocean circulations and dynamics. Particular emphasis is on

investigations carried out over the most extended river deltas worldwide. Although land areas of river deltas only comprise 5% of the global area, they are intensively developed and densely populated areas; river delta regions are where thirteen of the world's biggest cities are found. The broad investigations performed by multiple studies demonstrate that river delta regions are seriously affected by SLR and other natural disasters, justifying the need for extended analyses of natural and human-made events pertinent to coastal areas [94].

2. Remote Sensing Technologies for the Monitoring of Coastal and River Delta Regions

The exploitation of Remote Sensing (RS), Geographic Information Systems (GIS), and Global Navigation Satellite System (GNSS) techniques are crucial to maintaining efficient natural disaster management chains, and the knowledge of these methodologies allows the identification of potential gaps existing in the usability of the collected data and encourages the development of new approaches. It is widely accepted that satellite-based EO observations complement traditional in situ measurements. They are valuable tools that allow geospatial products to support decision support systems for different natural calamities. Over the last two decades, we have witnessed a growing availability of RS satellite constellations. The knowledge of natural catastrophes [90,95–101] has been improved using many images with various spatial, spectral, and radiometric resolutions.

Historically, optical remote sensing satellites using moderate and high spatial resolutions have commonly been used for observing coastal environment evolution. The Landsat satellites have continuously been in operation since 1972, which provides a continuity of high-quality Earth Observations and measurements, with spatial resolutions of about 30 m. The unique continuity and reliability of the Landsat data allow long-period time series analyses to investigate the global evolution of coastal regions [102,103]. Advanced approaches applying spatial and temporal data fusion models have recently been developed to combine Landsat imagery with lower frequency but higher spatial resolution observations and MODIS and VIIRS observations with a low spatial resolution and higher temporal resolution [104]. In this context, a significant role is now played by the “Landsat-like” Sentinel-2 constellation that consists of the two Sentinel-2A/B sensors and routinely provides a global revisit interval of 5 days at a spatial resolution of 10–60 m. Virtual satellite constellations can be designed by combining Landsat, Sentinel-2, and other optical remote sensing satellite data with similar resolutions, effectively increasing the global revisit interval. For example, Landsat-8, Sentinel-2A, and Sentinel-2B data can yield a comprehensive revisit period of 2.9 days [99,105,106]. It can map dynamic coastal geomorphological changes at a fine temporal resolution, directly benefiting coastal evolution mapping [107].

Moreover, RS technologies operating at the microwave band of the electromagnetic spectrum are also extensively employed to recover information about the geometrical and electromagnetic properties of an imaged scene. Synthetic Aperture Radar (SAR) represents a uniquely useful microwave instrument for EO, as it can acquire high-resolution data from the Earth with the potential to operate day and night and in any weather condition [108]. Sequences of SAR data are exploited by interferometric SAR techniques (InSAR) [109–119] for coastal mapping and monitoring to determine regions where severe changes have occurred over time, and correlate these changes with shoreline changes, coastal erosion, groundwater exploitation, etc. Other methodologies, such as measurement of the Doppler Centroid Anomaly (DCA) [120], can provide a viable and accurate estimation of sea surface displacements based on a single SAR image, which are related to currents and wind.

Nonetheless, InSAR systems have some limitations that need to be taken into consideration, as they can limit the reliability of the final products to some extent. These include noise introduced by wind [121], heavy precipitation [122], atmospheric perturbations [123], decorrelation phenomena [124], topography decorrelation [125], and other limitations that may arise from an incorrect data processing. If not well understood, the above limitations can be responsible for unreliable results, which could lead scholars to unreal and biased analyzes.

The remainder of this section provides technical details on the principal RS technologies, including both optical and microwave methods, emphasizing their role in the monitoring of major coastal regions and river deltas, and considers various disaster risk conditions, such as ground subsidence, flooding, coastal erosion, SLR, and extreme climatic events. Figure 1 shows the worldwide geographical distribution of major coastal regions and the major river deltas considered here.

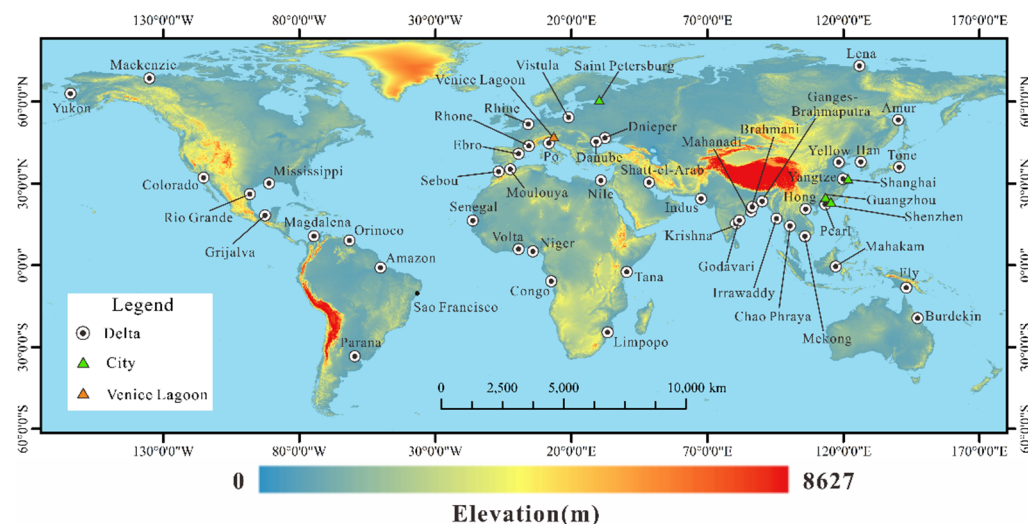


Figure 1. Map of the spatial distribution of the 48 most critical river deltas worldwide considered here [126]. The base map is a global map of lands surface elevation [taken from the GEBCO_2020 Grid [127]] with a spatial resolution of 15 arc s.

2.1. Remote Sensing Technologies for Deriving Land-Use and Land-Cover (LULC) Changes

Optical remote sensing imaging, including multi-spectral and hyperspectral RS imaging, is beneficial for extracting coastline information [128–132], deriving long-term land use and land cover change [133], retrieving nearshore bathymetry [134], mapping coastal wetlands [135,136], and detecting coastal erosion [137].

Numerous archived images with coarse, moderate, and high resolution from optical remote sensing satellites, including Terra/Aqua MODIS, Landsat, Sentinel, SPOT, IKONOS, WorldView, etc., have principally been utilized for long-term monitoring of land-cover and land-use modifications in river deltas [138]. Many studies have presented extended investigations of coastal and river delta zones using optical remote sensing image time series [138–144]. For instance, Seto et al. [139] monitored the land-use change in the Pearl River Delta using Landsat TM data from 1988 to 1996, revealing that urban areas increased by more than 300%. The work of [145] investigated land cover changes, magnitude, and urbanization of Jing-Jin-Ji, the Yangtze River Delta, and the Pearl River Delta, relying on the classification of Landsat TM and HJ-1A/B images. The results show that urban land areas have increased by about 28,000 km², and coastal wetlands and cropland have simultaneously decreased from 1990 to 2010. The authors of [146] used Landsat and HJ-1B images to detect the spatio-temporal dynamics of land-use and land-cover Mekong Delta from 1979 to 2015. During this period, large-scale inland planting land has been transformed into aquaculture ponds. Landsat images taken during the period from 1995 to 2010 show that the Yellow River Delta landscape has dramatically been changed with increases in urban and cultivated aquatic areas displacing naturally vegetated areas [142]. Landsat images from 1999 to 2013 were used to identify land-cover alterations in the Parana River Delta in South America [143]. However, a presentation of accurate and long-term multi-class land-cover and land-use products of the world deltas is rare. Land-cover and land-use change maps of global deltas with 10 to 30 m spatial resolution would be needed using data generated from Landsat, Sentinel-2, and SAR satellites. Acquiring cloud-free images with optical remote sensors for coastal areas located in cloudy and rainy areas is

particularly challenging. However, other observation techniques, such as SAR, are not typically hindered by cloud cover.

Unlike primarily applied to images acquired by optical satellites, a rapidly advancing research field concerns the development and application of change detection methods with SAR images at the microwave band [147,148]. SAR data are, thus, used for mapping the changes of Earth's surface due to natural phenomena or linked to anthropic activities. In this context, SAR microwave images are exploited because they bring complementary information, being the electromagnetic radiation of microwaves able to penetrate forest canopies. Many features can be extracted from sets of SAR images and the most commonly used estimator for the extraction of changes is the backscattering coefficient [149], a fundamental indicator of the ground conditions which is sensitive to surface roughness and depends on the polarization of the transmitting/receiving waves. Polarimetric decomposition through eigenvalue analysis of the complex data allows the identification and categorization of the type and contribution of the involved scattering mechanisms. These studies provide meaningful and thorough exploitation of SAR polarimetry [150], including the phase information discarded in studies using the backscattering coefficient. An alternative to using SAR backscattering to detect and map surface changes is exploiting interferometric SAR products, such as the coherence. Coherent change detection (CCD) techniques make use of the cross-correlation between the interfering pairs of complex SAR images [151]. A change of the scene can lead to a sensible variation of the coherence, and the coherence can be used as an additional way to discover and map such variations. A component of the coherence that is more difficult to model and relate to physical parameters is the temporal decorrelation [150,152], resulting in a combination between natural random changes and those possibly associated with events that are desired to track and study over time. In coherent change detection (CCD), ambiguity remains when coherence changes are not causally related to the events are misinterpreted. Thus, poor change detection performances are obtained. Further efforts to model the different causes of decorrelation in a coherence map are still required to discriminate and isolate the temporal decorrelation signals not causally related to the events under investigation. Tracking coherence differences between couples of SAR images were used to study different phenomena. A non-exhaustive but nearly comprehensive discussion of applications using CCD technologies, with a specific focus on those related to the monitoring of coastal and deltaic regions, can be found in [151,153–158].

2.2. Mapping Coastal Wetlands

Wetlands are highly diverse ecosystems that can provide necessary ecological goods and services. However, wetlands are threatened by intensive anthropogenic activities, and wetland loss is a global public concern [159]. In the Parana River Delta, one-third of wetlands once covered by freshwater marshes have been modified into pastures and forestry in the past 14 years, as revealed by Landsat images [143]. In the Gulf of Mexico, many woody wetland regions were replaced by urban land between 2001 and 2006, as quantified by optical remote sensing satellite imagery [141]. Optical remote sensing has advantages of inventory and monitoring wetlands over large geographic areas. Landsat, SPOT, NOAA AVHRR, IRS-1B, and other major satellite systems can be used for wetland identification and discrimination [160]. Additionally, radar imagery can distinguish between flooded and non-flooded areas, and radar can work in all weather conditions. The integration of radar and optical remote sensing images provides a promising methodology for improving wetland identification and classification.

2.3. Remote Sensing for Coastline Change Extraction

Optical RS technology can help efficiently extract and measure coastline changes with high accuracy over large areas [161–165]. These changes can be stimulated by natural phenomena, such as SLR, the effects of hurricanes and possibly, in case of large ruptures, the impacts of coastal earthquakes. Coastline changes can also be due to the direct involvement of humans. With RS techniques, the change detection of the coastline's orientation,

position, and shape [166] can retrieve valuable information on the inter-relationships between SLR and tidal currents, wave energy, land subsidence, and human intervention. Thus, the mapping of coastline changes is fundamental for coastal management, land use land change investigations, autonomous navigation, coastal erosion study, the planning of protection infrastructures, and an overall assessment of the increased risk of inundation at the coast. Coastline extraction is related to boundary extraction and image segmentation and belongs to the class of machine vision approaches [166,167]. Coastline changes have manually been outlined by expert photo interpreters who have visually inspected aerial photographs for many decades. However, these operations were costly and time-consuming. The frequently used automatic interpretation-based methods are mainly based on edge detection, index analysis, threshold segmentation, region growth, neural network, and sub-pixel [128,130,168–174]. Landsat imagery has efficiently been applied to monitor coastline evolution using dozens of years of data [175,176]. Long-term coastal changes of the Yellow River Delta have been determined based on decades of Landsat imagery. Sediment siltation, erosion, and human activities drive the dramatic deltaic coastline change [176].

Detecting coastal erosion with optical remote sensing imagery strongly depends on the accuracy and frequency of coastline extraction. High resolution optical remote sensing imaging methods, such as IKONOS, WorldView-2, WorldView-3, QuickBird, and GF-1, have been applied to extract coastline changes and geomorphology changes and map coastal erosion at a fine resolution [135,177–179]. Twenty-nine deltas of the world are in a state of overall erosion, determined by complementary analysis and quantification of coastline changes using satellite images of Landsat, SPOT-5, and SPOT-6 taken from 1972 to 2015 [131].

Although many coastline extraction methods using optical remote sensing imagery have been developed over the decades, there is no universally valid coastline extraction technique. All existing algorithms are applied to images of individual satellites or for applications. It is also challenging to choose an algorithm for an application, because there is still no established theory for this purpose and no index for comparing and evaluating the performance of different methods in other specific cases. Complete automatic coastline extraction methods and algorithms using high-resolution optical remote sensing imagery still need to be developed, and time series images of “30 m MODIS” and virtual satellite constellations promise future research directions. Despite the advantages of optical satellite remote sensing, there are also some obvious limitations due to cloud coverage on rainy days, solar illumination, and natural meteorological conditions. Microwave data can circumvent these problems, because they are not significantly affected by these factors. As clarified below, the exploitation of independent information from sets of radar images helps obtain accurate coastline change maps. Some approaches also use coherence information between couples of complex-valued synthetic aperture radar (SAR) images to discriminate the land and sea boundaries [180].

2.4. Ground Deformation Analyses

In coastal and river delta regions, ground deformations due to subsidence are poorly understood in many cases. Ground subsidence of deltas can occur naturally due to sediment compaction, peat oxidation, and tectonics [94], but can be highly exacerbated by anthropogenic activities, such as reduced sedimentation due to embankments, over the withdrawal of sub-surface fluid [181], underground construction [182], and land reclamation [183–187]. Coastal subsidence can cause an increase in relative sea level rise (RSLR), increased flooding frequency and areal extent, permanent loss of land elevation, subsequent coastal line retreat, failure of coastal defenses, wetland loss, and amplified groundwater salinization. In some cases, the amplitude of ground subsidence may be much larger than absolute SLR, which may amplify local RSLR. Precise measurements of the Earth’s surface deformations are routinely recovered by exploiting the Interferometric synthetic aperture radar (InSAR) technology. It relies on extracting the phase difference between complex-valued SAR images collected at separate times and from slightly different illumination

angles [188–190]. Many advanced interferometric SAR methodologies [116,118,191,192] have been developed to process heterogeneous sets of SAR acquisitions collected from different orbiting SAR constellation sensors during the last two decades. These research techniques have greatly advanced from the investigation of single deformation events [193,194] to follow the time evolution of the ground deformations through multi-temporal differential InSAR (MT-InSAR) techniques [110–113,116,118,119,195–197]. Historically, pioneering works developed for the analysis of ground deformations of coherent, pointwise targets (i.e., permanent scatters (PS)) were made by Ferretti et al. [197,198]. Many other PS-related works have been developed [112,114,199–202], which increased the attainable measurement points' density. Other PS-like approaches have been used, e.g., [203–205]. Among the various techniques, the Small Baseline Subset (SBAS) algorithm [110] was developed to produce a ground displacement time series of distributed scatterers (DS) on the ground by processing multi-look interferograms. Many alternative methods for the analysis of DS targets [111,115,195,206–213], and the generation of 2D (3D) displacement maps from multi-satellite/orbit data [214,215] have been designed. In the work of [216,217], a methodology was also proposed to employ the phase values of intermittent coherent DS targets. The recent work of [119] proposed an extension of the canonical SBAS approach to better operate in mid-to-low coherent scenarios, based on Weighted-SVD (WSVD), which exacerbates the concept of intermittent coherent targets and produces reliable displacement time series with variable sample length. Recently, another class of InSAR methods that explore the temporal relationships of a set of interferograms has also been proposed to enhance the InSAR performance [109,218–223]. InSAR products are primarily used to monitor ground stability and perform analyses of the potential risk in zones subjected to natural or anthropogenic causes of ground displacements. Interested readers can find an in-depth description of such methods and a series of applications in heterogeneous scenarios in [76,190,224–245]. Coastal ground subsidence has been investigated worldwide, in locations such as Houston (U.S.) [246], Mexico City, the Mississippi River delta (U.S.) [247], Norfolk and Miami Beach on the U.S. Atlantic coast [248], the Ionian coast of south-eastern Sicily (Italy) [249], the Volturno River Plain (Italy) [250], the Friuli Venezia Giulia coastal plain (Italy) [251], the Venice coastland (Italy) [252], the Gippsland Basin (Australia), and many other locations. Deltaic regions are significantly more susceptible to subsidence than other coastal areas. Previous studies have reported that many modern river delta regions are sinking due to ground subsidence and SLR [253], such as the Ganges–Brahmaputra–Meghna delta, the Mekong Delta [51], the Mississippi River Delta [254], the Yellow River Delta [255,256], the Yangtze River Delta, and the Pearl River Delta [257]. The Ganges–Brahmaputra–Meghna delta is the second largest globally, with over 100 million residents. A wide range of subsidence rates has been reported in the literature; however, the causes of subsidence in the delta are still not well understood, and reliable subsidence data for the whole region are scarce [258]. Ground subsidence has also been reported in the Yellow River Delta, mainly due to oil extraction and sediment consolidation and compaction [255,256]. Excessive groundwater withdrawal, rapid urbanization, sediment consolidation, and compaction are responsible for the ground subsidence of the Yangtze River Delta [182,259]. Ground subsidence in densely populated deltas is also a significant source of uncertainty in RSLR calculations.

To show the potential of InSAR methodologies, we portray in Figure 2 some examples of ground displacement maps. Specifically, Figure 2 shows the mean ground displacement velocity maps of the Saint Petersburg (a), Shenzhen (b1,b2), and Shanghai (c) regions, respectively. As detailed in [240,260,261], the ground deformation in these coastal regions is mainly due to terrain subsidence linked to land reclamation projects.

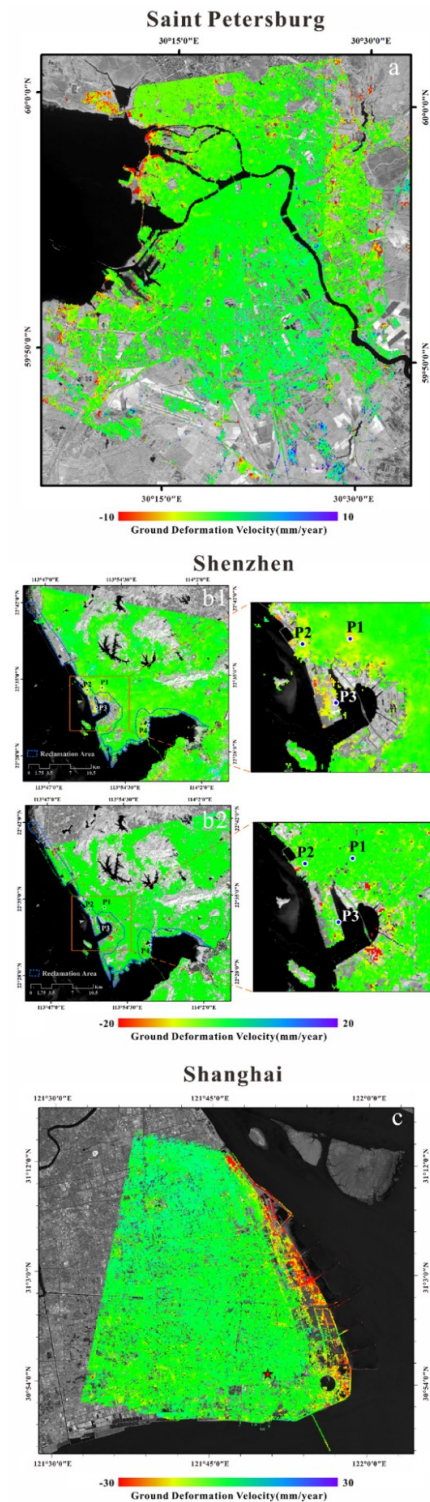


Figure 2. The geocoded mean ground displacement velocity maps of the coastal regions of Saint Petersburg (a), Shenzhen (b1,b2), and Shanghai (c). (a) The geocoded mean line-of-sight deformation velocity map of Saint Petersburg retrieved using Sentinel-1A/B descending track images acquired from 2016 to 2018 (refer to [261]); (b1) The map of 2007–2010 vertical (subsidence/uplift) deformation velocity derived from ENVISAT ASAR images (refer to [240]); (b2) The map of vertical mean deformation velocity derived from Sentinel-1A data acquired from June 2019 to June 2020; (c) The LOS mean displacement velocity map retrieved by the COSMO-SkyMed dataset acquired from 2013 to 2016 (refer to [240]).

2.5. Sea Surface Monitoring through SAR-Based Approaches

Sea surface can be evaluated by studying and estimating sea state parameters, such as bathymetry, waves, currents, wind vectors, etc. [262]. Several sea state observation instruments are available for marine monitoring, such as waveform buoys, weather stations, scatterometers, anemometric stations, etc. Such instruments can provide continuously acquired data but only at fixed locations, usually installed in specific strategic coastal areas. In recent years, SAR has allowed a new and exciting direction of remote monitoring, thanks to its synoptic vision and the ability to provide data covering large areas [263]. Hence, SAR features overcome limits related to some of the classic in situ instruments, and SAR images have been integrated with optical or multispectral images. Furthermore, SAR can be mounted on different platforms, such as aircraft or satellites [108]; this opportunity can provide other techniques and applications to monitor the sea surface state [120].

In the context of marine monitoring, existing satellite SAR systems are widely used to detect oil spills, and there are many other surface characteristics (such as wind, current characteristics, natural films, surface temperature patterns, rain cells) that provide oil-like radar signatures.

However, operational use of SAR (satellite or airborne) is limited by some factors. Satellite sensors move along orbits, and therefore, they are governed by celestial laws; this implies, first of all, that the revisiting time, after which the same region is imaged again, is fixed and cannot be changed in the case of emergencies. Moreover, the orbits covered by remote sensing satellites, cannot allow north-south deformation detections. Accordingly, spaceborne sensors could be not flexible enough to be helpful in catastrophe management. In this context, airborne SAR platforms could allow overcoming the above-mentioned limits while also assuring spatial resolutions higher than those of some satellite SAR sensors, due to smaller acceptable dimensions of transmitting antennas. Airborne SAR sensors were developed due to their flexibility and lower cost; hence, they are more efficient than the much more expensive satellite missions [264].

Nevertheless, airborne raw data are affected by the so-called motion errors, which are due to the presence of atmospheric turbulences that produce sensor track deviations from an ideal straight track. Motion errors, if not properly accounted for during the SAR focusing procedure, may seriously damage the quality of the final image. Accordingly, the so-called Motion Compensation (briefly MOCO) algorithms are commonly applied within the SAR focusing step with the aim of achieving the same image accuracy usually reached with spaceborne SAR data [265,266].

Consequently, the choice of the SAR platform is made based on the type of analysis to be developed.

The use of SAR data to estimate sea state parameters is based on the computation of the SAR signal backscattered to the radar instrument from the sea, which is governed by the interaction between the transmitted electromagnetic waves and short surface waves. The development of algorithms to extract surface currents from a collected SAR image's amplitude signal is a somewhat complicated issue. Furthermore, the SAR intensity's exclusive use is not enough for the direct measurement of sea currents due to many variables that globally influence the sea backscattering, such as the wind, bathymetry, etc. Therefore, the joint use of amplitude and phase information embedded in the SAR images provides the means to access more direct measurements of interest parameters [120,267].

Marine surface current velocities are a crucial sea state parameter that can also be estimated through SAR sensors, thanks to many research efforts in this field in the last years [120,267–272]. Today, SAR-based applications are relatively well-established for estimating waves and the derivation of wind over the sea surface [273–275].

Surface current velocities can be estimated using two different SAR data processing techniques: the Along-Track Interferometry (ATI) [271] and Doppler Centroid Anomaly (DCA) method [120]. Both methods only measure the radial component of the sea surface velocity, i.e., the radar-to-target line-of-sight (LOS) component. However, it is worth noting that the radar Doppler frequency results from several factors, e.g., ocean currents, wind

fields, ocean waves, and wave–current and wave–wave interactions [120,269,270], and extra work is required to separate the various mechanisms.

For ocean current estimation, it is necessary to integrate data acquired from SAR with wind models, ocean models, and real data obtained from in situ instruments (when available), such as buoys, to get a quantitative and precise description of the current sea state [276,277]. Currently, only a limited number of operational services exist; thus, research in this field is substantial. Consequently, many efforts are still required to foster SAR data for coastal applications, considering the potential social and economic returns: regional coastal protection, ship traffic monitoring, electrical energy generation from the sea, etc. Additionally, the results obtained in this framework could also be helpful for the analysis and characterization of meteorological phenomena.

ATI requires that the SAR images be achieved from along-track displaced antenna phase centers [278]. The ATI technique typically operates on a SAR data pair, which allows for the combination of two (or more) SAR data points collected over an identical area; data are collected from different orbital positions but separated by a physical baseline along the azimuth direction. The estimated phase differences are proportional to the Doppler shifts of the backscattered radar echoes [279]. More specifically, when two SAR antennas are dislocated along the radar flight track (azimuth direction), the radar signal related to the identical target is collected by the different antennas within a short time lag. Accordingly, the targets' movements translate to phase shifts on the interferometric phase difference [268,280].

In the framework of marine observation, examples of fast-varying phenomena are sea current surface velocity and vehicle fluxes in marine environments; hence, their monitoring necessitates a technique, such as ATI, able to measure changes in the observed scene over a short time scale [280,281].

This technique has undergone significant development in recent years. Still, it requires unique sensor characteristics: namely, the possibility of having two antennas spaced along the azimuth direction, which can achieve images with a short time lag. For this reason, this technique is often successful in using SAR sensors mounted on airborne platforms.

The DCA technique, unlike ATI, exploits a single SAR image and relies on measuring the Doppler shifts induced on the SAR images by the LOS component due to the sea surface velocity [120]. The DCA is obtained by subtracting from the Doppler Centroid the term corresponding to a "stationary" scene, e.g., the scene where all scatterers move at the same velocity associated with the Earth's rotation [275]. Depending on the radar wavelength, the sea surface velocity can be obtained from DCA using a given factor. Furthermore, in the literature, some studies have used DCA to analyze the sea state by considering surface currents and wind influence [273–275,282].

The DCA has the potential to obtain information on the surface current with a single SAR image, acquired with any sensor and platform. Therefore, the use of this technique is very flexible.

Sea state is generally defined for the ocean where statistical characteristics of the wave field do not vary appreciably [262]; therefore, ocean areas typically represent the starting point. Hence, several SAR technology applications consider case-study areas in oceans or coastal regions [120,263,270].

Current interest has also been oriented to inland seas, where currents occur in a much-limited range. The Mediterranean Sea represents an interesting case study for estimating sea surface currents with the SAR techniques [275,281,283,284]. Furthermore, recently, the use of SAR images has been applied for the analysis of inland waters. In the literature, SAR applications on lakes are mainly limited to the analysis of the backscattered signal amplitude. In these cases, the SAR amplitude is used as a support for optical or thermal imagery [285–287]; moreover, there are some studies that show the potential of using SAR images to recover the size of surface eddies in large lakes [288] and information distributed in space on the intensity of the wind [289]. Finally, a preliminary study was also presented

in which the possibility of recovering surface water velocity from SAR Doppler analysis in medium-sized lakes is investigated [265].

To show the potential of these methodologies in an operational context, we show in Figure 3 some results related to an acquisition performed in January 2013 in an area along the south coast of Italy that includes the Volturno river estuary (see the zoomed-in area of Figure 3). The test area covers about $7 \text{ km} \times 3 \text{ km}$ (azimuth and range) along the coastline. Data were collected in January 2013 by an airborne SAR system, the InSAeS4 system (also called TELAR), an Italian-operated, InSAR-oriented airborne platform operating at the X-Band [290,291]. The area encompasses the Volturno river estuary (see the zoomed-in area in Figure 3). The test area covers about $7 \text{ km} \times 3 \text{ km}$ (azimuth and range) along the coastline. On the right side of Figure 3 is the estimated sea surface velocity map. The mean value decreases toward the coast, which is expected behavior for a marine environment.

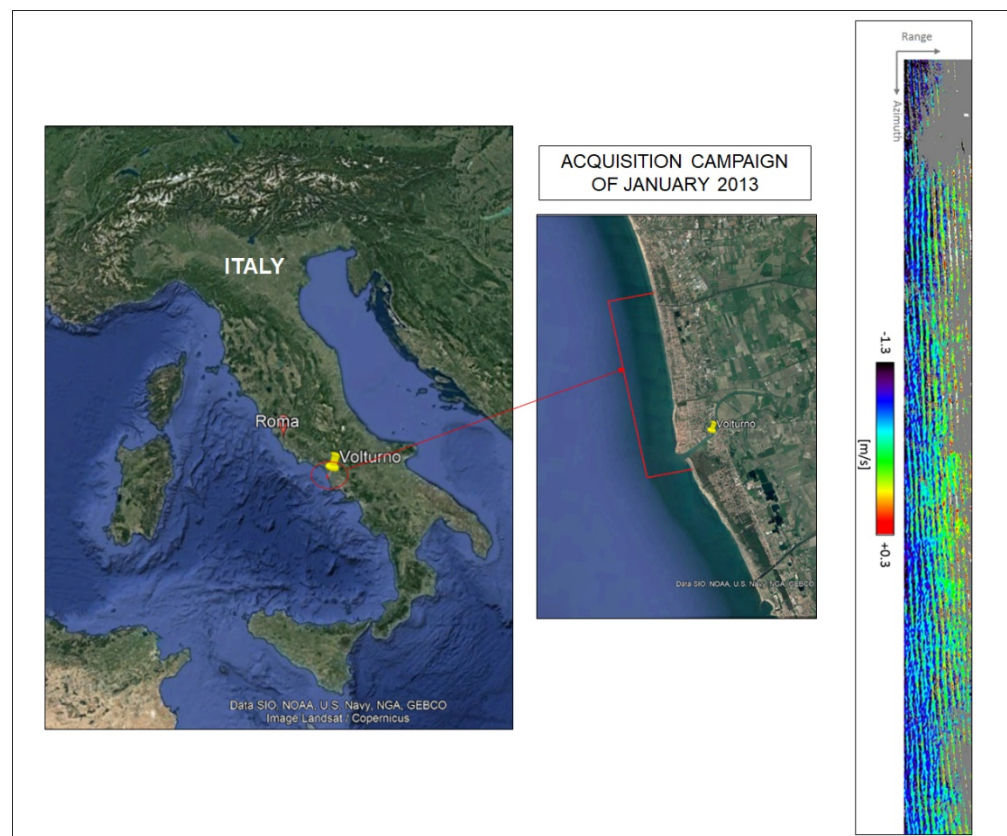


Figure 3. Test site presented in [281], situated along the coast of southern Italy. The middle panel displays a zoomed-in view of the area of interest. The right panel shows the sea surface velocity map obtained from the ATI technique [281].

A further example of applying the DCA technique in the Mediterranean Sea can be found in [275]. The analysis proposed in this work was oriented to understand the influence of wind on the sea surface radial velocity estimated from the Doppler analysis of SAR. This methodology is based on the joint use of three modules exploiting SAR data: the DCA map, wind information (e.g., speed and direction), and the Doppler map associated with wind. The results demonstrate that the use of DCA for estimating surface speed can provide valuable results for the internal seas, and the integrated use with wind analysis represents a helpful methodology for a precise estimation of the sea surface velocity. The results shown in Figure 4 and obtained from DCA evidence there is a relatively good correspondence between the surface velocity obtained from DCA and the surface velocity due to the wind contribution.

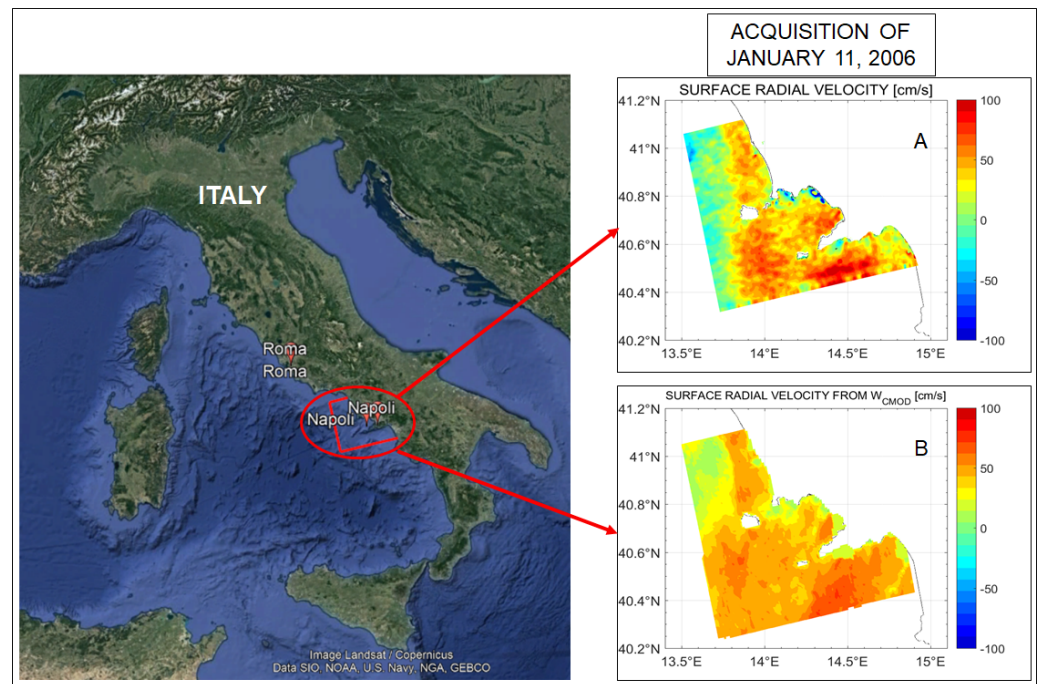


Figure 4. The test site presented in [275], is situated in southern Italy near the Gulf of Naples and is indicated by red on the left panel. On the right, panel (A) presents the surface radial velocity map, and panel (B) displays the surface radial velocity due to the wind, both obtained from the DCA technique [275]. The results are obtained from an ASAR ENVISAT acquisition on 11 January 2006.

3. Experiments

In this section, we address two main topics: (i) the exploitation of advanced RS techniques to evaluate the impacts of global climate change and anthropogenic activities on the coast of large river delta regions and (ii) the study of the interactions between the ocean and the coast using RS methods and the evaluation of their implications in response to projected climate change. We summarize the main findings of some recent case studies for selected areas, including major river deltas in China and Eastern Asia, the Po River Delta and the Venice Lagoon in Italy, the St. Petersburg Bay in Russia, the Nile Delta in Egypt, the Mississippi River Delta in the U.S., and the Amazon River in Brazil (see Figure 5). Of great concern is that most major river deltas are sinking at a larger rate than SLR [253], which significantly increases the impact of relative sea level rise. Many deltas are extremely sensitive and vulnerable to the cascading effects and increased risks of global climate change, local ground subsidence, and intensive human activities. The acceleration in global mean sea level, increasing frequencies of extreme weather events, ground subsidence, declining upstream sediment fluxes, and decreasing wetland areas impact the integrity of the delta regions of the world. Recently, the work of [126] has systematically assessed the changing risk profiles of 48 coastal deltas and found that most coastal deltas are at an elevated risk level. Here, we emphasize how RS technologies are valuable instruments for detecting, monitoring, and quantifying risk conditions and the potential impacts on land and population centers. The following sub-sections address specific natural and/or anthropogenic phenomena that affect coastal regions, including the risks due to coastal erosion, coastal flooding and extreme meteorological events, sea level rise, and storm surge. Next, we will focus on selected delta river zones and provide a brief overview of recent investigations performed in these regions.

3.1. Coastal Erosion Risk

Accelerated coastal erosion due to human activities, such as a global reduction in sediment flux induced by dams, oil and gas extraction in alluvial plains and nearshore

regions, illegal sand excavation, etc., and an ongoing warming climate are now common issues for all coasts of the world [292]. Coastal erosion can increase groundwater salinity and saltwater intrusion. Over half of the delta regions of the world have conditions of overall erosion in terms of reduced river sediment loads [131]. River bed diversions induced by oil industry activities have caused the shoreline dynamics of the Yellow River Delta to undergo erosion and accretion of 13 to greater than 21 km over four decades, as observed by Landsat observations [163]. In total, 68% of the Mekong delta shoreline is undergoing erosion because of the Mekong River's reduced sediment loads, mainly caused by an increased number of dams and large-scale sand mining [293]. Coastal erosion rates have generally increased in the entirety of the Russian Arctic [294]. Around 85% of the river deltas of the world shrank over temporal and spatial scales in the first decade of the 2000s due to sediment load decline, and this trend is expected to become more severe in the following decades [253]. Intensive human activities have dramatically reduced coastal wetland areas. Accelerated SLR could also exacerbate saltwater intrusion. Higher saltwater levels can contaminate fresh surface and groundwater resources by infiltrating coastal aquifers. Increased salinity intrusion could significantly threaten local ecosystems, crop yield, tree production, etc. By analyzing about 250,000 coastal groundwater wells in the U.S, Jasechko et al. [295] found that the groundwater levels of a majority of the observed wells located along more than 15% of the contiguous coastline are currently below sea level.

3.2. Flood Risk

Coastal flood risk and adaptation are worldwide concerns [296,297]. Previous studies suggest that about 40 million people living in coastal port cities are likely to be subject to at least one major coastal flooding event each century [298]. Using global re-analysis products of storm surge and extreme sea levels and a hydrodynamic model, Muis et al. [299] estimated 76 million people could be subjected to a once a century flood event. The most significant inundation mainly occurs in the delta regions of Asia and Europe, especially China, the Netherlands, Vietnam, and Egypt, all of which have relatively sensitive flood exposure. European coasts will be strongly impacted by climate-induced flood risk [11]. It has been estimated that by the end of 2100, five million Europeans will be under the threat of a 100-year extreme sea level event [11]. Previous investigations have documented that low-lying river deltas, especially cities, are significant flood risk hotspots [299–301]. Global climate change and local ground subsidence can significantly increase the exposure to coastal flooding risk. Previous research has employed different approaches (e.g., GIS-based method, RS, hydrodynamic models, etc.) to map and simulate flood inundation in floodplains [302–316]. Various numerical models have also been developed for floodplain delineation/flood inundation and flow simulation [317–320].

Satellite RS is a valuable tool for detecting and monitoring flood phenomena [318,321], allowing the differentiation between inundated and non-inundated areas. Flood risk increases due to urban growth, land subsidence, and climate change [322]. Identifying areas that are more prone to extreme floods helps optimize urban planners' civil protection actions and evaluate damage [323]. To reliably estimate the losses in affected regions, comprehensive maps of the flooded areas and the computation of the water level and flow velocity are required [324–327]. Recent advances in RS technology have allowed the generation of rapid damage prediction maps and associated models helpful in a flood event [e.g., the Copernicus Emergency Management Service (<https://emergency.copernicus.eu/>) (accessed on 1 May 2021)]. Satellite RS data are beneficial to detect the impact of severe floods at distinctive spatio-temporal resolutions, using multispectral [328–332] or SAR [333–339] images. SAR data are beneficial for sub-tropical cloud-prone areas, and consecutive SAR time series help a multifaceted understanding of flood regimes. For instance, Kuenzer et al. [321] used ENVISAT ASAR-WSM time series with a spatial ground resolution of about 150 m for analyzing flood dynamics and floodwater progression in the Mekong River Delta. Associated with coastal flooding risk is the growing worldwide occurrence of extreme weather events and rapidly evolving flash floods that overpower the capacity of coastal

populations to develop effective responses [340,341]. RS satellite data are widely used to monitor rapid flash floods' effects and forecast their occurrence and strength. For instance, a recent study has documented a remarkable increasing tendency of extreme rainfall in the vicinity of major Chinese delta rivers, including the cities of Shanghai, Suzhou, and Nanjing, from 1998 to 2015 [342]. Several advanced applications of RS technology for the evaluation of the effects of extreme rainfall have recently been proposed [343–346]. Finally, it is also worth highlighting that weather radar has assisted predictions for more than 50 years by providing rainfall estimates and helping develop proper hydrological models (see, for instance, [347,348]).

3.3. Sea Level Rise and Tidal Evolution

3.3.1. Sea Level Rise

Global sea levels are increasing and likely accelerating worldwide, escalating impacts on coasts. Additional risks are brought by the increased probabilities of erosion, tidal flooding, and modulations in annual or seasonal cycles related to weather and storms. Low relief and low elevation deltas are regions particularly susceptible to the effects of global SLR. Some deltas are already experiencing submergence risk because of the combined impact of land loss, reduced sedimentation rates, and SLR [349]. Hinkel et al. [296] found that damage due to coastal flooding events is likely to increase significantly, and the risks to populations and coastal assets in the coastal floodplain will magnify. Another critical factor is that tidal range may often vary in river delta regions due to the combined consequences of alterations in background water levels and improvements to harbors and other coastal infrastructure projects that can modify friction and resonance. Changes in annual cycles may also occur in some locations, which may amplify the seasonal effects of water levels. Mean sea level (MSL) changes can often be severe in low-lying coastal regions, especially true for population hubs located in estuaries and river delta regions. The combined changes of MSL, tidal evolution, and annual variability can lead to higher rates of “total” water levels, known as peak extended water levels (PEWL). A recent global survey of PEWL at long-period tide gauges demonstrated that rates of PEWL can often be much larger than MSL, up to 8 mm yr^{-1} , which is over twice the global average of MSL [350]. Figure 5 displays PEWL rates and the difference between mean extended water level rates (MEWL; a time-variable expression of MSL) over the past 50 years, showing significant differences between the two estimates in the western Atlantic and Pacific Oceans. These changes may trigger various local water depth changes in coastal regions, impacting entire coastal ecosystems.

3.3.2. Tidal Evolution

The water depth changes brought by SLR may, in turn, modulate the response of tides via resonance changes, frictional changes, and other mechanisms [29,351]. Changes in tidal range, tidal currents, and energy distribution can induce severe adverse effects on human society, since the economy of the estuarine population depends on the stability of the coastal ecosystem, including fisheries, farming, and tourism. Extreme storm events (e.g., hurricanes, typhoons, or tsunamis) may lead to catastrophic consequences to estuarine cities through extensive damage to critical coastal infrastructure and disturbance of the local economy. However, both hurricanes and tsunamis are short-lived, and estuarine and coastal societies have developed knowledge about such extreme events that allow them to respond promptly and quickly recover from natural disasters. Many local populations have implemented estuarine developments, including harbors, roads, and public infrastructures. Storms and other extreme events can have severe short-term impacts on coastal environments, but on longer timescales, the average characteristics of the coastal zones, such as MSL and local tidal range, have historically remained relatively constant. However, under the present-day scenarios of increasing SLR accompanied by the associated changes in tidal range, many coastal communities are now experiencing an alteration of “stable background” water levels, and prior assumptions and measures adopted to face worst-case scenarios may no longer be valid, making coastal defense infrastructures insufficient to

mitigate upcoming extreme events. In some locations, the changes in MSL and tidal range might occur rapidly, such as that seen in the developed harbor regions of Hong Kong [352]. Thus, it is difficult to predict future coastal flooding events without a careful individual analysis of each coastal location. The combined response of MSL and tidal range can vary significantly by location.

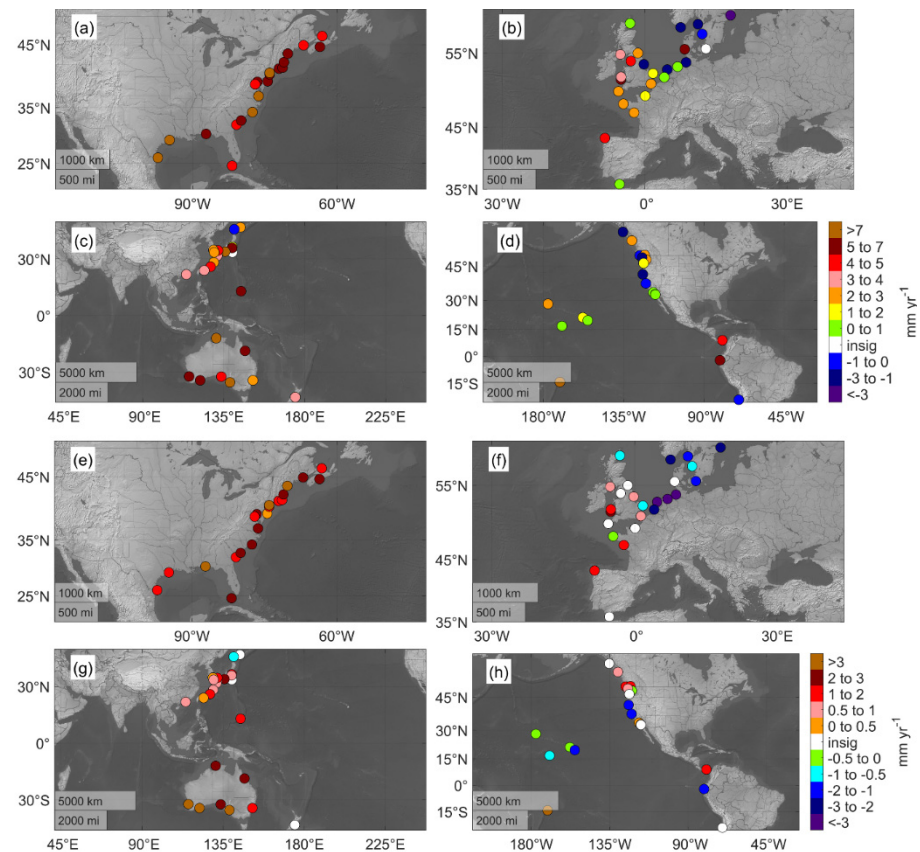


Figure 5. (a–d) Peak extended water level trends over the past 50 years (PEWL50). (e–h) Differences between PEWL and MEWL trends (EWL50_diff). All units are in mm yr⁻¹ following the color bars at the bottom right; different color scales are used in other plots (from [350]).

Tides are evolving at different rates in many coastal zones due to non-astronomical mechanisms [353–355]. Regionally based investigations have investigated changes in the diurnal and semi-diurnal tides of the Eastern Pacific [27], the Gulf of Maine, [356], the North Atlantic [354,357], in China [358,359] and Japan [360], and of different Pacific islands [361]. Tidal evolution might result from harbor modifications [196,362–366], often due to land reclamation or channel deepening. MSL may directly influence tidal evolution or be related to tidal variability through secondary mechanisms in several ways and at different scales, from a local to a basin-wide (amphidromic) level. Some possible mechanisms include a “coupled oscillator” effect between the open ocean and the continental shelves [367,368], through warming of the upper ocean [33], which may lead to internal changes in stratification properties and modulation of thermocline depth, and modifications of the surface manifestation of internal tides [369].

3.3.3. Tidal Anomaly Correlations (TAC)

Short-term tidal evolution can be as important to coastal zone dynamics as long-term changes in tides and SLR. The relationship of tidal sensitivity to short-term sea level fluctuations has been previously explored using the tidal anomaly correlation (TAC) method [29,351,370,371]. Surveys of the Pacific and the Atlantic Ocean have shown TACs to be significant at over 90% of locations analyzed, with the most considerable changes often

being found in estuarine or deltaic regions. Hong Kong, located near the Pearl River Delta, shows a significantly positive tidal sensitivity, further investigated in a focused regional study [352]. Tidal anomaly correlations (TACs) respond to short-term tidal variability to short-term MSL fluctuations, which express individual tidal components' sensitivity to any given sea level perturbation. A parallel approach can combine the largest tidal amplitude variabilities and be summed as a proxy for the change in tidal range or the highest astronomical tide (δ -HAT). Both TACs and δ -HATs can be helpful to understand how tidal evolution can complicate the future overall behavior of total water levels at coastal and estuarine locations as SLR continues. Locations with strong positive values can indicate where tidal changes are reinforced as MSL increases and suggest the most extensive positive feedback to total sea levels, thus showing higher probabilities of flooding coastal and estuarine locations. In Hong Kong, near the Pearl River Delta, some of the most substantial variability of the tidal range was observed [352], and some results of this study are shown below in Figure 6. Individual TAC results are widely observed and mixed between positive and negative at the Hong Kong tide gauge network (comprising 12 separate locations), but the δ -HATs are only significant at less than half of these gauges, with substantial positive values seen at the harbor locations of Quarry Bay and Tai Po Kau, which have been significantly modified over the past century. This demonstrates the impacts that anthropogenic modifications can have on coastal zones.

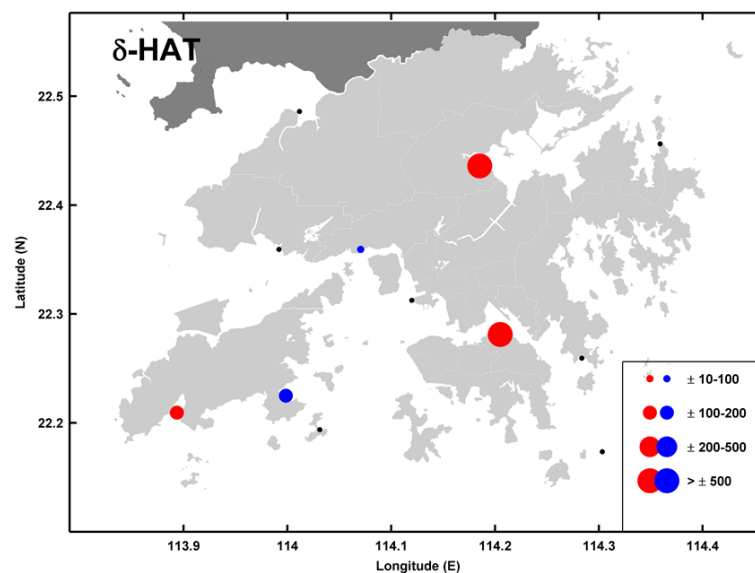


Figure 6. δ -HAT map for the Hong Kong tide gauge network [352]. Size of the markers shows the relative magnitude according to the legend, expressed in units of mm m⁻¹. Red/blue colors indicate positive/negative TACs, and black markers indicate insignificant values.

The variability of tides with MSL variability can also be dependent on frequency. A new study [372] analyzed the tidal variability in the Indian Ocean on multiple timescales, considering seasonal, annual, and interannual modulations of tides and MSL separately. The separation of different timescales is helpful to understand the reasons for the variability, and the most prevalent correlations seen were in the annual frequency band, which may indicate that the relevant mechanisms have to do with seasonal meteorological variability. For instance, the Indian monsoon system and its pattern of changing winds and extreme rainfall is likely the reason behind the strongly positive tidal variability observed in the Ganges Delta region. Figure 7 displays these results for the M_2 tide (the twice a day lunar tide). In another recent study, the long-period (monthly and fortnightly) tides' behavior in estuaries was considered in the Yangtze River case [373]. Whereas incoming high-frequency tides will quickly diminish while travelling upstream in a river due to friction from working against the outgoing river discharge, it was revealed that low-frequency

tidal components might amplify when moving upstream, potentially adding an extra 0.5 to 1.0 m to an upstream river stage level for hundreds of kilometers. This effect may be a severe complication during high river flood events, particularly for the Yangtze River watershed, which saw its worst flooding season in decades in 2020 and can undoubtedly increase flood risk and waterlogging in the estuary tidal flat regions.

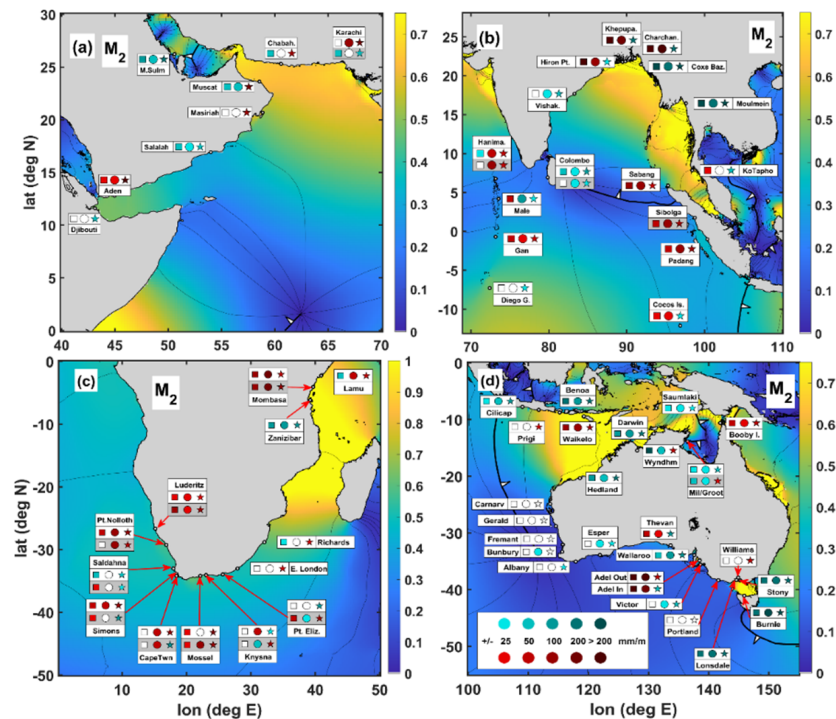


Figure 7. M_2 TACs in four different regions of the Indian Ocean: (a) the Arabian Sea, (b) the Bay of Bengal, (c) Africa, and (d) the Australian region. Symbols inside boxes indicate three different frequency bands: squares are the sub-annual (SA) band, circles are the annual (ANN) band, and stars are the interannual (IA) band. Station names are also indicated. Color shading of the symbols indicates positive (shades of red) and negative (shades of blue) TACs, according to the legend at the bottom right. Background colors show tidal amplitudes (corresponding to the color bar at the right of each subplot in units of meters) and phases (solid lines, in increments of 30°) from the TPXO 7.2 global solution [374]. The figure is taken from [372].

3.4. Storm Surge

Storm surge is the most severe impact of tropical cyclones in river deltas. The combined consequences of high winds and water levels are responsible for considerable property damage and high causality rates in densely populated delta river regions worldwide [298,375]. In total, 26 of 48 major coastal deltas are located in tropical areas (see Figure 5), making them vulnerable to cyclonic storms. The IBTrACS database (v04r00) (downloaded from the IBTrACS website <https://www.ncdc.noaa.gov/ibtracs/index.php?name=ibtracs-data>; IBTrACS-All data v04r00 all storms points shapefile (accessed on 1 January 2021)), which contains complete global datasets of historical tropical cyclone tracks from 1842 to 2019, is used to calculate the density of all tropical cyclone tracks, shown in Figure 8. Many previous studies have documented a substantial global increase in severe cyclones and a consistent shift of the latitude of maximum tropical cyclone intensity, which agrees with the projections of future climate models [376]. Many studies have also assessed the potential risk of tropical cyclones in the coming decades and centuries in densely populated river delta cities/regions. Table 1 shows the risk rate index of 48 major coastal cities, and Table 2 summarizes the risk conditions of the world's most significant river delta regions.

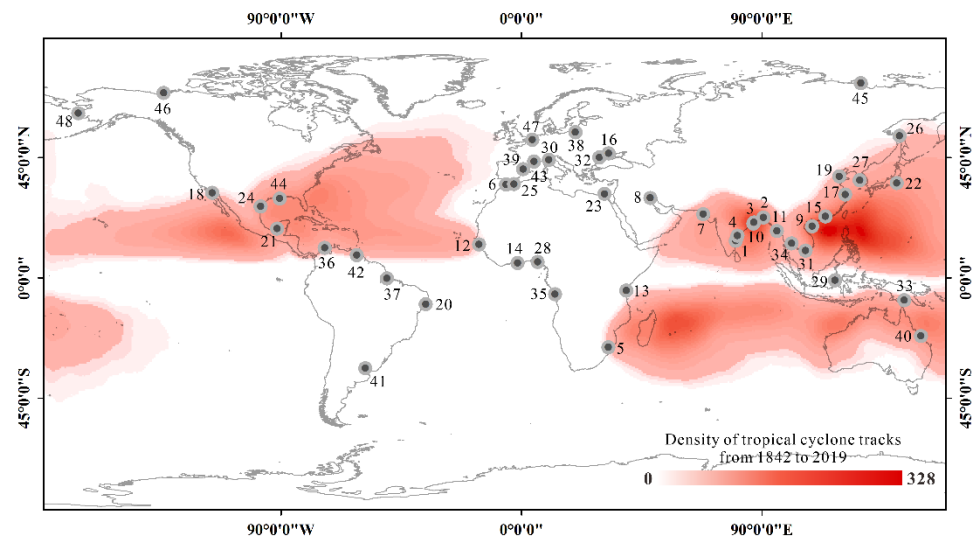


Figure 8. Locations of 48 major coastal deltas collectively hold over 340 million inhabitants [377]. The labeled number of each delta represents the risk rank trend due to increasing exposure associated with anthropogenic relative sea level rise, as estimated by [126], and the risk rate of change index (rank) is listed in Table 1. The Krishna delta (Rank 1) has the highest risk trend. All deltas are listed in Table 1. According to the color bar at the bottom right, the density of all tropical cyclone tracks from 1842 to 2019, as determined by the IBTrACS database, is overlaid in red contours.

The work of [378] examined the spatio-temporal patterns and the return periods of tropical storms and hurricane landfalls along the East and Gulf Coasts of the United States by analyzing 105 years (1901–2005) of tropical cyclone strikes. A tropical hazard index (THI) was developed to estimate the vulnerability of these regions from a geographic perspective. The THI of the Mississippi River Delta has a value of approximately 130. The work of [379] analyzed tropical cyclones that affected the Yangtze River Delta and the Pearl River Delta from 1951 to 2010 and found that the frequency of tropical cyclones has varied harmonically, with periods ranging from 2 to 6 years.

Table 1. The world's 48 major coastal deltas.

Delta (Country)	Risk Rate of Change Index ¹ (Rank)	If the Delta Is in Tropical Regions or Not
Krishna (India)	0.28(1)	Yes
Ganges-Brahmaputra-Meghna (Bangladesh)	0.22(2)	Yes
Brahmani (India)	0.22(3)	Yes
Godavari (India)	0.21(4)	Yes
Limpopo (Mozambique)	0.21(5)	Yes
Sebou (Morocco)	0.19(6)	No
Indus (Pakistan)	0.19(7)	Yes
Shatt-el-Arab (Iraq)	0.16(8)	No
Hong (Vietnam)	0.16(9)	Yes
Mahanadi (India)	0.16(10)	Yes
Irrawaddy (Myanmar)	0.15(11)	Yes
Senegal (Senegal/Mauritania)	0.13(12)	Yes
Tana (Kenya)	0.13(13)	No
Volta (Ghana)	0.12(14)	No
Pearl (China)	0.12(15)	Yes
Dnieper (Ukraine)	0.11(16)	No
Yangtze (China)	0.10(17)	Yes

Table 1. Cont.

Delta (Country)	Risk Rate of Change Index ¹ (Rank)	If the Delta Is in Tropical Regions or Not
Colorado (Mexico)	0.10(18)	Yes
Yellow (China)	0.097(19)	Yes
Sao Francisco (Brazil)	0.095(20)	No
Grijalva (Mexico)	0.085(21)	Yes
Tone (Japan)	0.083(22)	Yes
Nile (Egypt)	0.082(23)	No
Rio Grande (USA/Mexico)	0.078(24)	Yes
Moulouya (Morocco)	0.076(25)	No
Amur (Russia)	0.069(26)	Yes
Han (South Korea)	0.068(27)	Yes
Niger (Nigeria)	0.067(28)	No
Mahakam (Indonesia)	0.061(29)	No
Po (Italy)	0.060(30)	No
Mekong (Vietnam)	0.057(31)	Yes
Danube (Romania)	0.056(32)	No
Fly (Papua New Guinea)	0.054(33)	Yes
Chao Phraya (Thailand)	0.049(34)	Yes
Congo (Democratic Republic of Congo/Angola)	0.048(35)	No
Magdalena (Columbia)	0.047(36)	Yes
Amazon (Brazil)	0.044(37)	No
Vistula (Poland)	0.043(38)	No
Ebro (Spain)	0.040(39)	No
Burdekin (Australia)	0.040(40)	Yes
Parana (Argentina)	0.036(41)	No
Orinoco (Venezuela)	0.033(42)	Yes
Rhone (France)	0.030(43)	No
Mississippi (USA)	0.025(44)	Yes
Lena (Russia)	0.019(45)	No
Mackenzie (Canada)	0.016(46)	No
Rhine (Netherlands)	0.014(47)	No
Yukon (USA)	0.005(48)	No

¹ Risk rate of change index of each delta was estimated in [126].

Table 2. Significant risks for eight critical deltas (refer to [133,253,258,380–405]).

Delta	Ground Subsidence	Flood Risk	Erosion Risk	Tidal Wetland Decline	Extreme Rainfall	Storm Surge	Urbanization and Over-Population
Mississippi Delta	An average subsidence rate of 5.2 ± 0.9 mm/y was measured by GPS [380].	Significant drowning is inevitable [381].	The sediment load is insufficient. Upstream dams trap ~50% of the total sediment load [381,382].	>25% of deltaic wetlands have disappeared [383].	The largest floods in the last century principally resulted from heavy rainfall in the lower Mississippi Delta [384]. El Niño generates a positive precipitation anomaly over the lower Mississippi Basin [385].	The Mississippi Deltas are especially susceptible to storm surge [386].	Urbanization has increased substantially over the past five decades. Population growth has increased in the past decades [387].
Po River Delta	The Po River Delta has experienced serious ground subsidence in the late 19th century [388]. The maximum deformation velocities are in the order of -30 mm/y. It is mainly caused by compaction of highly compressible sediments and heavy extraction of methane water [389].	Flooding events along with episodes of storm surge have increased, enhanced by climate variations [388]. Disastrous floods occurred in last century [391].	Severe coastal erosion was triggered by ground subsidence, and promoted by reduced sediment loads of the rivers.	The natural wetlands were mainly converted to agricultural and urban areas in the last century [390].	N/A	Climate changes makes the influence of storm surges and flooding more alarming [388].	Urbanization increased by agriculture settlement in the last century. Agricultural activities were a major driver of wetland loss in last century, and it increased agricultural settlement [390].
Mekong Delta	The ground subsidence rates are around 1–4 cm/y based on InSAR measurements [392].	Threatened by the increased inundation hazard.	Mekong River Delta experienced dramatic evolution. Coastlines retreated toward land in low-lying areas [393].	Wetland degradation is caused by resettlement and economic development policies, population growth and urbanization, demand for food and reclaiming for agriculture, construction of canals and dykes, expansion of travel systems [394].	Extreme rainfall events occurred more frequently in the northern areas, indicating the northern region is facing high risk of flooding [395].	N/A	Experienced fast pace of urban development [396]. Densely populated.
Yangtze River Delta	Shanghai, a representative megacity situated in deltas, records the greatest ground subsidence in China. Ground subsidence has been also found in the other cities of the delta, including Suzhou, Wuxi, and Changzhou. Over-pumping groundwater and rapid urbanization are the major causes.	The delta is highly sensitive to increasing flood risk. The interaction of sea level rise, land subsidence, and storm surges may lead to more abrupt flood disasters.	The Yangtze River Delta is also facing erosion risk in the context of reduction of sediment load from upstream.	Intensive reclamation has caused degradation and loss of tidal wetland [397].	The regional yearly extreme precipitation events cause floods [398].	Yangtze River Delta is with the highest risk of storm surge [399].	Fast urbanization and expansion. Densely populated.

Table 2. Cont.

Delta	Ground Subsidence	Flood Risk	Erosion Risk	Tidal Wetland Decline	Extreme Rainfall	Storm Surge	Urbanization and Over-Population
Pearl River Delta	Three regional subsidence bowls has been detected by InSAR and multi-platform SAR imagery [400].	Flood risks of the middle and lower delta were enhanced with analysis of the historical flood records [401].	Anthropogenic activities like dredging, sand mining, and sediment disposal increase erosion risk.	Wetland loss has occurred due to rapid urbanization.	Extreme rainfall events increased at a significant pace in the most recent ten years.	Pearl River Delta is with the highest risk of storm surge [399].	Fast urbanization. Densely populated.
Yellow River Delta	The average subsidence rate is -5 mm/y, while the highest subsidence rate of -33 mm/y.	Flood events occur frequently.	Increased coastal erosion due to reduced sediment load [253,402].	Newly created wetland enlarges by 25 km ² each year [403].	N/A	The coasts of Yellow River Delta are with the highest risk of storm surge [399].	Intensive urbanization, oil industry. Densely populated.
Ganges-Brahmaputra-Meghna	The reported subsidence rates are variable: A mean of 5.6 mm/y, and median of 2.9 mm/y [258].	Around 80% of the delta area is floodplain, with floods occurring every six years or so.	Erosion is mainly due to insufficient sediment supply and extreme events.	Large of mangrove areas have been converted into paddy fields and shrimp farms [404].	Rainfall is dominated by the monsoon season. The delta is highly vulnerable to extreme rainfall events.	Storm surges are a major concern.	Urbanization rate is evident [405]. Highly populated.
Nile Delta	Ground subsidence is strongly localized at big cities.	The coastal areas are prone to be flooded.	Significant coast erosion has occurred.	Wetland were converted to agricultural lands [133].	N/A	N/A	The urban extent has increased. Living more than 50% of the Egyptians.

3.5. Remote Sensing Investigations of Large Rivers Deltas

3.5.1. The Yangtze River Delta

The Yangtze River is the third-largest river globally in terms of length and is one of the world's most important river deltas. The coastal vulnerability of the Yangtze River Delta is currently amplified due to the combined impacts of non-linear land subsidence related to groundwater extraction [259], instabilities of underground infrastructure constructions [182], large-scale land reclamation of ocean areas [397], an accelerated rate of SLR [406], tidal evolution [407], and natural hazards [408,409]. Shanghai, one of the world's largest megacities with 24 million inhabitants, is located within the Yangtze River Delta zone and has an average population density of over 2000 inhabitants per square kilometer. Additionally, a continuous supply of fine-grained suspended sediments from the Yangtze River has yielded the development of extensive tidal flats along the deltaic coast. Large dams, like other large rivers, intensively regulate the Yangtze River. The sediment supply and the high total discharge rate in the Yangtze River Delta have promoted the development of sizeable ocean-land reclamation projects in the intertidal and wetland areas [410,411]. The Yangtze River Delta is also experiencing highly rapid economic and population growth over the last fifty years. Rapid industrial development and urbanization have caused widespread ground subsidence in the delta region, not only in Shanghai but also in the mid-sized cities and many nearby small cities and towns. Homogeneous subsidence in the Shanghai suburban area and exceptionally rapid subsidence along metro lines, highways, and elevated roads have also been observed by InSAR-based time series measurements ([182,412]). The detected land subsidence is mainly caused by groundwater exploitation and rapid urbanization [412]. Shanghai has also performed numerous large-scale ocean-reclamation projects [413]. The new lands are subject to long-lasting subsidence phenomena, which have been extensively studied in recent years using InSAR technology [240,314,414–417]. These investigations have clarified how land subsidence of the reclamation projects combined with SLR can pose severe threats to population centers in the future [308,314,418]. The newly reclaimed lands may also advance the shoreline dozens of kilometers inland. Simultaneously, it is difficult to predict how the subsidence trend will continue, and the magnitude of cumulative land deformation depends highly on the localized drivers and responses. RS technology permits us to monitor the land continuously and apply corrective measures. However, the penetration of these technologies into local administrations is still lacking and has to be further promoted.

The mean Yangtze River water discharge and mean sediment flux of the Yangtze River had declined since 2003 when the Three Gorges Dam began operation [419]. The decline of water and sediment discharges is attributable to climate change and human activities, such as decreased precipitation, construction of reservoir dams, and soil conservation. On the other hand, the Yangtze River Delta, especially the Yangtze Estuary, is highly susceptible to SLR. In particular, it has been predicted that 40% of the terrestrial area of the Chongming Dongtan Nature Reserve, at the mouth of the Yangtze Estuary, will likely be submerged by 2100, given the expected 0.88 m of SLR [420]. The effects of SLR might be even worse due to ground subsidence [421].

3.5.2. The Pearl River Delta

The Pearl River Delta is the third-largest delta in China, located on the southern coast of mainland China on the South China Sea and is one of the world's most urbanized and industrialized regions [422]. The river delta and many surrounding areas are below local high tide storm surge levels. Over the last 50 years, reclaimed lands have been merged into over one hundred enclosures protected by flood defense measures. However, many coastal areas remain under threat from natural hazards, such as river flooding, waterlogging, typhoons, and tidal-induced flooding [401,423–427]. Over recent decades, extensive land reclamation projects have been carried out to keep up with urbanization and industrial development. The delta region is exposed to natural disasters, such as ground

subsidence caused by soft soil compaction, Karst geomorphology, and regional tectonic effects [257,400,428]. Guangzhou, one of the major metropolitan regions in the Pearl River Delta, has continuously experienced ground subsidence and ground collapse accidents in recent decades. The increase in geological hazards has also caused casualties [429]. Sudden ground collapse accidents occurred near metro lines, which were under construction at the time, due to over-pumping of underground water, compaction of soft soil, concentrated underground construction, and Karst geomorphology. Noticeable ground subsidence has also been observed in the other mega-cities of the delta, such as Macao, Shenzhen, and Hong Kong [240,430,431].

The Pearl River Delta is also facing increased inundation threats due to SLR and has experienced a high frequency of flooding disasters in the last century [401,432]. Long time series tidal records and long-term geological subsidence suggest that relative sea level may experience a 30 cm rise at the mouth of the estuary by 2030, and extensive coastal areas will be heavily and severely affected by the potential risk of tidal inundation [433]. The tidal range has also been observed to have a strong sensitivity to sea level variability in this region, as tide gauges in Hong Kong show that the increase in the tidal range may increase by up to 0.6 m for every 1 m of SLR [352]. Additionally, indiscriminate sand excavation throughout the Pearl River region since the 1980s directly affects annual extreme water levels, further increasing the risk of flooding [434].

3.5.3. The Yellow River Delta

The Yellow River ranks second globally in sediment load, and the second-largest oilfield (Shengli Oilfield) in China is located in the Yellow River Delta. Similar to the Yangtze River Delta, the runoff and sediment load have exhibited declining trends in the first decade of this century. These trends are mainly due to water and soil conservation measures, reservoir and dam construction, increased water consumption, and inter-annual fluctuations of rainfall caused by climate change. Although the runoff and sediment load has decreased, the Yellow River Delta area and the length of the coastline in the delta have increased [435]. Ground subsidence has also occurred in the Yellow River Delta as monitored by InSAR analysis and spirit levelling [255,256]. It is mainly caused by oil extraction, sediment consolidation, and compaction. The Yellow River Delta also experiences the highest worldwide erosion rate. By analyzing Landsat archives acquired over four decades, net erosion areas of shoreline retreat have been observed to be greater than 13 km, and net accretion areas of shoreline advance are greater than 21 km [163].

3.5.4. The Mekong Delta

The Mekong Delta is vital to the economy of Vietnam. Extensive floods severely influenced the delta during the last century [436]. It now faces significant changes due to the development of new infrastructures and facilities for irrigation, flood prevention, and electricity generation that have led to substantial hydrological alterations [437–440]. In particular, the over-exploitation of groundwater in the Mekong Delta has caused the widespread hydraulic head decline and ground subsidence over a region of ~1000 km² [392]. In [321], the flood risk in the Mekong river delta was analyzed via ENVISAT SAR images acquired from 2007 to 2011, which applied incoherent change detection algorithms. Those results showed that flooded areas most often coincided with the two-season rice crop areas in the delta. Another critical risk condition in this ecosystem is salinity intrusion, which occurs during the dry season.

3.5.5. The Ganges–Brahmaputra–Meghna Delta

The Ganges–Brahmaputra–Meghna delta is especially vulnerable to flooding, ground subsidence, and increased sea salinity intrusion [441]. Salinity intrusion has occurred due to a massive reduction in river inflow caused by dams, barrages, embankments, and SLR. As a result, people have had to travel further upstream to find suitable fresh water in the coastal city of Khulna. Additionally, increased salinity has adversely affected coastal

vegetation and animals, such as the death of Sundari trees, the loss of shrimp farming, and the impacts on a wide range of biodiversity. The Sundarban wetland located in the delta is one of the most extensive coastal wetlands globally, covering over 100 km². Over the past centuries, the Sundarban mangroves have been modified into paddy lands and shrimp farms, which has accelerated salinity intrusion in the region.

3.5.6. The Po River Delta and the Venice Lagoon

The North Adriatic coastal area in Italy is a large area of geophysical and historical relevance. It includes Venice's city and its lagoon, the Po River delta, and the Emilia Romagna region. The Po River delta is the largest in Italy and is highly threatened by SLR [442–444]. The Po River Delta has experienced widespread shoreline retreat and salinity intrusion due to anthropogenic-induced subsidence and SLR [445,446]. Land subsidence of the delta is the most severe in Italy [388,389]. The irreversible sinking due to the over-extraction of methane water from Quaternary strata in the last century caused average subsidence of approximately 50 cm to 3 m [388]. Consequently, some flat coastal areas have become inundated.

Sea level in the Venice lagoon is subject to seasonal and long-lasting periodic changes, with fluctuations over a few hundred years and cycles alternating between cold-wet and warm-dry periods. These phenomena are amplified by present-day climate change, and the vulnerability risk increases [447]. The locally known phenomenon of “Acqua Alta” in the city of Venice refers to the excessive-high tides responsible for episodic flood events [see, for instance, the recent flooding events that occurred in November 2019 [448,449]]. This phenomenon has a cascading effect on the media, society, and the scientific community due to the Venice lagoon having a historical and fragile ecosystem. However, recent studies on the land subsidence of the Venice lagoon carried out by using multi-temporal/multi-satellite interferometric SAR analyses at different wavelengths and spatial scales [389,443] have confirmed that the historical city of Venice is essentially tectonically stable now. In contrast, the northern sector of the lagoon, see Figure 3 in [443], is subject to an average ground displacement of up to 3 cm/year, as observed from 1992 to 2017. Although the amplitude of subsidence reduced in the last few decades, the low-lying coastal areas are still threatened by the combined flooding risk of SLR and elevation loss.

3.5.7. Saint Petersburg

The city of St. Petersburg is located along the banks of the Neva River, on the Gulf of Finland in the Baltic Sea. The city's topography is nearly flat, with an elevation range of 1–5 m. Regular floods have historically impacted the city's coastal area [450]. From 1703 to 2010, 339 flood events have been recorded [261,451]. An average of one flood per year was recorded from 1703 to 1975, and this rate has approximately doubled in the last forty years [261]. The sea level of Neva bay was calculated in [450] for three floods in Saint Petersburg on 21 November–2 December 2011, on 20 December 2011–1 January 2012, and on 19–30 October 2013, using the BALT-P hydrodynamic flooding model. This revealed a maximum water column height of about 183 cm in December 2010. To prevent significant economic losses due to frequent floods and efficiently manage land subsidence and its joint risk with SLR, a flood prevention facility complex was designed and built by the municipal government [452]. The recent land subsidence of the Saint Petersburg Bay has recently been investigated in [261] through the multiple-satellite Minimum Acceleration (MinA) combination technique [215], which allows the discrimination of east-west and up-down deformation time series, relying on two sets of Sentinel-1 SAR images collected between 2016 and 2018. An independent investigation of this phenomenon has also been reported elsewhere [453], showing that the ground deformation of the city is nearly steady, except for the western sector of the Neva river delta, where ground deformation associated with considerable land reclamation projects has a maximum rate of about 10 cm/year (see Figure 2).

3.5.8. Nile Delta

The Nile Delta supports 63% of Egypt's agricultural land and accommodates about 45% of its population. Erosion, land subsidence, and deterioration of natural habitats have influenced the coastal areas of the Nile Delta [133]. Severe erosion has occurred along the Nile Delta coast due to reduced sediment supply after dam construction on the river, with estimated maximum shoreline recession rates of about 100 m/year [454,455]. InSAR techniques has been used to retrieve land subsidence of the delta; most of the big cities in the delta are suffering from land subsidence, which are mainly due to ground water pumping [456]. The subsidence of the deltaic region has led to land-use change and land loss for agriculture and aquaculture activities. Coherence data obtained from ERS-1/ERS-2 SAR data's tandem mission were also utilized to delineate the border between the water and land [457].

3.5.9. Mississippi Delta

The Mississippi River and its delta is the most extensive river system in North America, draining 41% of the water of the continental United States [458]. For millennia, the river delta has been relatively stable, though subject to continuous accommodation processes resulting from SLR and ground subsidence [459]. From the mid-1950s to the mid-1970s, a progressive loss of wetlands, including the formation of holes in the delta plain and the transformation of wetlands to open water, has occurred [460–463]. Since the 1990s, satellite measurements have been widespread to investigate the Mississippi River plume structure, sediment transport, and water circulation [464]. Multi-scale temporal analyses of remotely sensed imageries were demonstrated to be a useful tool capable of precise measurements of land changes in wetland environments [160,465]. Furthermore, the possibility of using SAR interferometry to predict future flood events in the river floodplain has been demonstrated [e.g., [466]]. The Great Mississippi/Atchafalaya river flood of 2001 [467] demonstrated that massive floods significantly change the seasonality of sediment discharge, requiring an update to flood management plans, and changes are likely more significant due to the numerous systems of levees and dams established to constrain the discharge to the ocean. The results also show that InSAR methods can develop and test hydrodynamic models to prevent future flood events and efficient risk management in near-real-time profit from parallel computation architectures. Additional information and extensive studies related to the region of the Mississippi River and the northern coastal area of the Gulf of Mexico through satellite remote sensing techniques can be found in [464,468] and references are contained therein.

3.5.10. The Amazon River Delta

The Amazon River is one of the major axial alluvial rivers on the planet, characterized by a massive volume of water and sediment seasonally exchanged through complex channel floodplain interactions [e.g., [469–472]]. Understanding and predicting water storage changes is vital to evaluating the potential impacts of climate change on a continental and worldwide scale. Several remote sensing data studies have been conducted to model the river's hydrodynamics [473–475]. In particular, the work of [476] analyzed rainfall estimates from the Tropical Rainfall Measuring Mission (TRMM) satellite over the Tapajos River basin. They used the data as inputs to a large-scale hydrological model for the whole basin, demonstrating that satellite data are helpful to identify damaged or aberrant rain gauges on a basin-wide scale. The Amazon River floodplain's annual inundation has been comprehensively studied [see, for instance, [477,478]]. The results show that many different water types can enter the floodplain and affect flooding events, including rainfall, flooding of local tributaries, groundwater, or exchange with the main channel [469]. Flooding is also influenced by the local topography, soil characteristics, and the vegetation of the floodplain. RS data to calculate the regional methane emission rates for the Amazonian wetlands are also a topic of great interest to this region and the world. Methane emissions in the atmosphere are generated by the anaerobic degradation of organic matter and

can significantly influence global climatic and environmental changes, land use, and river alterations [479–484]. Amazonian wetlands' flooded forests, lakes, and floating macrophytes are globally significant tropospheric methane sources [483]. RS has made it possible to quantitatively analyze the inundation and vegetation cover in the wetlands of the Amazon basin [473,477,485–488].

4. Discussion

This paper has demonstrated that there is a broad and growing scientific interest in investigating the effects of natural and man-induced disaster risks in coastal and river delta regions. Worldwide coastal regions and river deltas are vulnerable environments experiencing many pressures and are subject to numerous natural and human-made threats, some of which are triggered by global climate changes. EO technologies have proven valuable tools for local authorities and national governments to design, maintain, and manage effective disaster plans and obtain consistent and frequently updated information about environmental conditions and their temporal variations. Additionally, we remark that the growing availability of EO datasets has led in recent years to a significant shift in the perceptivity of RS technologies and the role of GIS [489–491] for the planning and organization of suitable disaster management cycles. EO instruments can contribute significantly to management of major technological and natural disasters and help during humanitarian crises. The increased scientific interest in the design and maintenance of effective disaster management plans in coastal communities is also demonstrated by the increased number of publications addressing this research theme in the literature. The paper has addressed the different conditions of risk in coastal and river delta environments.

Coastal flood risk and adaptation are a worldwide concern. Significant inundation is increasingly common in many delta regions of Asia and Europe, including China, the Netherlands, Vietnam, and Egypt, subject to relatively high flood exposure. Global climate change can significantly increase the population's exposure to coastal flooding risk. Satellite RS is a valuable tool for detecting and monitoring flood phenomena, allowing for the rapid differentiation between inundated and non-inundated areas. Extreme rainfall can also cause flooding, enormous economic losses, and civilian casualties. Another generator of flooding in coastal regions is storm surges associated with tropical cyclones. The combined effects of high winds and water levels are responsible for considerable damage to property and casualties in densely populated river delta regions worldwide.

Coastal flood risk is due to total sea levels, not just mean sea level, and the effects of tidal evolution can make the influences of MSL rise much more severe. The tidal anomaly correlation method (TACs) described above demonstrate that changes in tidal evolution that may accompany sea level rise can amplify the magnitude of total water levels, which can, in turn, strengthen all the detrimental risks to coastal regions and deltas described in this review. The TACs and δ -HATs observed from worldwide surveys show that nearly half of all locations are significant. However, large-magnitude tidal responses (which can either be positive or negative) are predominantly found in coastal regions, mainly in delta and estuarine regions.

Local ground subsidence can significantly increase the exposure to coastal flooding risk. Ground subsidence has become a significant global problem for world coasts. River delta regions are considerably more susceptible to subsidence than other coastal areas, partially due to the increased urbanization rates. The causes of ground subsidence in different deltas are numerous. Most major river deltas are sinking much faster than historical sea level rise rates. However, the mechanisms behind the subsidence are still not well understood, and reliable subsidence data for entire regions are scarce. Long-term and large-scale subsidence measurements for the most important delta regions are still lacking.

Accelerated coastal erosion is also a common issue nowadays on the world's coasts. Over half of the world's delta regions are in overall erosion due to reduced river sediment loads. Intensive human activities have dramatically reduced coastal wetland areas. Accelerated sea level rise may also exacerbate saltwater intrusion.

5. Conclusions

This work summarized some recent applications of RS technologies in major coastal and river delta regions of the world, including major river deltas in China and Eastern Asia, the Po River Delta, the Venice Lagoon in Italy, the St. Petersburg Bay in Russia, the Nile Delta in Egypt, the Mississippi Delta River in the U.S., and the Amazon River in Brazil. Advanced RS techniques can evaluate the impacts of climate change and anthropogenic activities on the coasts and large river delta regions. RS methods can also study the interactions between the ocean and the coast and evaluate their implications in response to projected climate change. RS technologies can also measure and map the long-term evolution of coastal and deltaic environments, providing updated information on environmental variations, assessing hazards and risks, and understanding the relevant mechanisms. Many new RS satellite programs are being scheduled and deployed, and many new methods are being developed in concert. One such example is the integration of many similar satellite sensors, such as Sentinel-2 and Landsat, to establish a virtual constellation that allows frequent observations of highly dynamic environments. Combining optical and microwave RS images will make it possible to frequently and efficiently observe coastal environment evolution in cloudy and rainy areas, including the extraction of coastline information, deriving long-term land use and land cover change, and retrieving nearshore bathymetry, mapping coastal wetlands, and detecting coastal erosion.

Author Contributions: Conceptualization, Q.Z., J.P., A.T.D. and A.P.; Data curation, A.T.D., M.T., C.Y., V.Z. and F.F.; Formal analysis, Q.Z., A.T.D., M.T., C.Y., V.Z., F.F. and A.P.; Funding acquisition, Q.Z.; Methodology, Q.Z., J.P., A.T.D. and A.P.; Project administration, Q.Z. and A.P.; Resources, Q.Z., J.P., A.T.D. and A.P.; Supervision, A.P. and A.T.D.; Visualization, A.T.D., M.T., C.Y., V.Z. and F.F.; Writing—original draft, Q.Z., A.T.D., J.P. and A.P.; Writing—review and editing, Q.Z., A.T.D. and A.P. All authors have read and agreed to the published version of the manuscript.

Funding: This research was funded by the Natural Science Foundation of China, grant number 41801337; by the Research Grants of Science and Technology Commission of Shanghai Municipality, grant number 18ZR1410800; by the Fundamental Research Funds for the Central Universities of China; and by the Fund of the Director of the Key Laboratory of Geographic Information Science (Ministry of Education), East China Normal University, grant no. KLGIS2017C03.

Institutional Review Board Statement: Not applicable.

Informed Consent Statement: Not applicable.

Acknowledgments: This work was also performed within the Dragon 5 ESA project ID 58351, entitled “Global Climate Change, Sea Level Rise, Extreme Events and Local Ground Subsidence Effects in Coastal and River Delta Regions through Novel and Integrated Remote Sensing Approaches (GREENISH)”. Sentinel and Landsat datasets were downloaded from the ESA Sentinel Hub and USGS Earth Explorer sites, respectively.

Conflicts of Interest: The authors declare no conflict of interest.

References

1. Xu, Y.; Zhang, D.; Shen, S.; Chen, L. Geo-hazards with characteristics and prevention measures along the coastal regions of China. *Nat. Hazards* **2009**, *49*, 479–500. [[CrossRef](#)]
2. Gogoberidze, G. Tools for comprehensive estimate of coastal region marine economy potential and its use for coastal planning. *J. Coast. Conserv.* **2012**, *16*, 251–260. [[CrossRef](#)]
3. Fedorov, G.; Korneevets, V. Socioeconomic typology of Russia’s coastal regions. *Balt. Reg.* **2015**, *4*, 121–134. (In Russian) [[CrossRef](#)]
4. Ayyam, V.; Palanivel, S.; Chandrakasan, S. Climate Change and Its Impact on the Coastal Region. In *Coastal Ecosystems of the Tropics—Adaptive Management*; Springer: Singapore, 2019; pp. 219–245.
5. Janekovic, I.; Mihanovic, H.; Vilibic, I.; Tudor, M. Extreme cooling and dense water formation estimates in open and coastal regions of the Adriatic Sea during the winter of 2012. *J. Geophys. Res.-Oceans* **2014**, *119*, 3200–3218. [[CrossRef](#)]
6. Barnard, P.L.; Short, A.D.; Harley, M.D.; Splinter, K.D.; Vitousek, S.; Turner, I.L.; Allan, J.; Banno, M.; Bryan, K.R.; Doria, A.; et al. Coastal vulnerability across the Pacific dominated by El Nino/Southern Oscillation. *Nat. Geosci.* **2015**, *8*, 801–807. [[CrossRef](#)]
7. Rani, N.N.V.S.; Satyanarayana, A.N.V.; Bhaskaran, P.K. Coastal vulnerability assessment studies over India: A review. *Nat. Hazards* **2015**, *77*, 405–428. [[CrossRef](#)]

8. Cid, A.; Menendez, M.; Castanedo, S.; Abascal, A.J.; Mendez, F.J.; Medina, R. Long-term changes in the frequency, intensity and duration of extreme storm surge events in southern Europe. *Clim. Dyn.* **2016**, *46*, 1503–1516. [[CrossRef](#)]
9. Forzieri, G.; Feyen, L.; Russo, S.; Vousdoukas, M.; Alfieri, L.; Outten, S.; Migliavacca, M.; Bianchi, A.; Rojas, R.; Cid, A. Multi-hazard assessment in Europe under climate change. *Clim. Chang.* **2016**, *137*, 105–119. [[CrossRef](#)]
10. Vitousek, S.; Barnard, P.L.; Fletcher, C.H.; Frazer, N.; Erikson, L.; Storlazzi, C.D. Doubling of coastal flooding frequency within decades due to sea-level rise. *Sci. Rep.* **2017**, *7*, 1399. [[CrossRef](#)]
11. Vousdoukas, M.I.; Mentaschi, L.; Voukouvalas, E.; Verlaan, M.; Feyen, L. Extreme sea levels on the rise along Europe's coasts. *Earth's Future* **2017**, *5*, 304–323. [[CrossRef](#)]
12. Nicholls, R.J.; Hoozemans, F.M.J.; Marchand, M. Increasing flood risk and wetland losses due to global sea-level rise: Regional and global analyses. *Glob. Environ. Chang.* **1999**, *9*, S69–S87. [[CrossRef](#)]
13. Arendt, A.A.; Echelmeyer, K.A.; Harrison, W.D.; Lingle, C.S.; Valentine, V.B. Rapid wastage of Alaska glaciers and their contribution to rising sea level. *Science* **2002**, *297*, 382–386. [[CrossRef](#)] [[PubMed](#)]
14. Lambeck, K.; Esat, T.M.; Potter, E.K. Links between climate and sea levels for the past three million years. *Nature* **2002**, *419*, 199–206. [[CrossRef](#)] [[PubMed](#)]
15. Morris, J.T.; Sundareshwar, P.V.; Nietch, C.T.; Kjerfve, B.; Cahoon, D.R. Responses of coastal wetlands to rising sea level. *Ecology* **2002**, *83*, 2869–2877. [[CrossRef](#)]
16. Lambeck, K.; Antonioli, F.; Purcell, A.; Silenzi, S. Sea-level change along the Italian coast for the past 10,000 yr. *Quat. Sci. Rev.* **2004**, *23*, 1567–1598. [[CrossRef](#)]
17. Ericson, J.P.; Vorosmarty, C.J.; Dingman, S.L.; Ward, L.G.; Meybeck, M. Effective sea-level rise and deltas: Causes of change and human dimension implications. *Glob. Planet. Chang.* **2006**, *50*, 63–82. [[CrossRef](#)]
18. Rahmstorf, S. A semi-empirical approach to projecting future sea-level rise. *Science* **2007**, *315*, 368–370. [[CrossRef](#)]
19. Craft, C.; Clough, J.; Ehman, J.; Joye, S.; Park, R.; Pennings, S.; Guo, H.; Machmuller, M. Forecasting the effects of accelerated sea-level rise on tidal marsh ecosystem services. *Front. Ecol. Environ.* **2009**, *7*, 73–78. [[CrossRef](#)]
20. Tol, R.S.J. The economic effects of climate change. *J. Econ. Perspect.* **2009**, *23*, 29–51. [[CrossRef](#)]
21. Vermeer, M.; Rahmstorf, S. Global sea level linked to global temperature. *Proc. Natl. Acad. Sci. USA* **2009**, *106*, 21527–21532. [[CrossRef](#)]
22. Nicholls, R.J.; Cazenave, A. Sea-Level rise and its impact on coastal zones. *Science* **2010**, *328*, 1517–1520. [[CrossRef](#)] [[PubMed](#)]
23. Church, J.A.; White, N.J. Sea-Level rise from the late 19th to the early 21st century. *Surv. Geophys.* **2011**, *32*, 585–602. [[CrossRef](#)]
24. Jacob, T.; Wahr, J.; Pfeffer, W.T.; Swenson, S. Recent contributions of glaciers and ice caps to sea level rise. *Nature* **2012**, *482*, 514–518. [[CrossRef](#)] [[PubMed](#)]
25. Neumann, B.; Vafeidis, A.T.; Zimmermann, J.; Nicholls, R.J. Future coastal population growth and exposure to sea-level rise and coastal flooding—A global assessment. *PLoS ONE* **2015**, *10*, e0118571. [[CrossRef](#)]
26. DeConto, R.M.; Pollard, D. Contribution of Antarctica to past and future sea-level rise. *Nature* **2016**, *531*, 591–597. [[CrossRef](#)]
27. Jay, D.A. Evolution of tidal amplitudes in the eastern Pacific Ocean. *Geophys. Res. Lett.* **2009**, *36*, L04603. [[CrossRef](#)]
28. Griffiths, S.D.; Hill, D.F. Tidal Modeling. In *Handbook of Sea-Level Research*; John Wiley & Sons: Hoboken, NJ, USA, 2015; pp. 438–451.
29. Devlin, A.T.; Jay, D.A.; Zaron, E.D.; Talke, S.A.; Pan, J.; Lin, H. Tidal variability related to sea level variability in the Pacific Ocean. *J. Geophys. Res.-Ocean.* **2017**, *122*, 8445–8463. [[CrossRef](#)]
30. Wei, X. On the evolution of global ocean tides. *Geophys. Astrophys. Fluid Dyn.* **2021**, *115*, 184–191. [[CrossRef](#)]
31. Rouault, M.; White, S.A.; Reason, C.J.C.; Lutjeharms, J.R.E.; Jobard, I. Ocean-atmosphere interaction in the Agulhas Current region and a south African extreme weather event. *Weather. Forecast.* **2002**, *17*, 655–669. [[CrossRef](#)]
32. Cayan, D.R.; Bromirski, P.D.; Hayhoe, K.; Tyree, M.; Dettinger, M.D.; Flick, R.E. Climate change projections of sea level extremes along the California coast. *Clim. Chang.* **2008**, *87*, 57–73. [[CrossRef](#)]
33. Domingues, C.M.; Church, J.A.; White, N.J.; Gleckler, P.J.; Wijffels, S.E.; Barker, P.M.; Dunn, J.R. Improved estimates of upper-ocean warming and multi-decadal sea-level rise. *Nature* **2008**, *453*, 1090–1093. [[CrossRef](#)] [[PubMed](#)]
34. Wang, S.; McGrath, R.; Hanafin, J.; Lynch, P.; Semmler, T.; Nolan, P. The impact of climate change on storm surges over Irish waters. *Ocean Model.* **2008**, *25*, 83–94. [[CrossRef](#)]
35. Oke, P.R.; Griffin, D.A. The cold-core eddy and strong upwelling off the coast of New South Wales in early 2007. *Deep. Sea Res. Part II Top. Stud. Oceanogr.* **2011**, *58*, 574–591. [[CrossRef](#)]
36. Bernardes, M.C.; Knoppers, B.A.; Rezende, C.E.; Souza, W.F.L.; Ovalle, A.R.C. Land-sea interface features of four estuaries on the South America Atlantic coast. *Braz. J. Biol.* **2012**, *72*, 761–774. [[CrossRef](#)] [[PubMed](#)]
37. Fox-Kemper, B.; Hewitt, H.T.; Xiao, C.; Aðalgeirsdóttir, G.D.; Drijfhout, S.S.; Edwards, T.L.G.; Hemer, M.; Kopp, R.E.; Krinner, G.; Mix, A.; et al. Ocean, Cryosphere and Sea Level Change. In *Proceedings of the Climate Change 2021: The Physical Science Basis, Contribution of Working Group I to the Sixth Assessment Report of the Intergovernmental Panel on Climate Change*, Geneva, Switzerland, 26 July–6 August 2021.
38. Garner, G.G.; Hermans, T.; Kopp, R.E.; Slangen, A.B.A.; Edwards, T.L.; Levermann, A.; Nowikci, S.; Palmer, M.D.; Smith, C.; Fox-Kemper, B.; et al. IPCC AR6 Sea-Level Rise Projections. Version 20210809. PO.DAAC, CA, USA. Available online: <https://podaac.jpl.nasa.gov/announcements/2021-08-09-Sea-level-projections-from-the-IPCC-6th-Assessment-Report> (accessed on 1 December 2021).

39. Cai, F.; Su, X.; Liu, J.; Li, B.; Lei, G. Coastal erosion in China under the condition of global climate change and measures for its prevention. *Prog. Nat. Sci.* **2009**, *19*, 415–426. [[CrossRef](#)]
40. van Rijn, L.C. Coastal erosion and control. *Ocean Coast. Manag.* **2011**, *54*, 867–887. [[CrossRef](#)]
41. Roebeling, P.C.; Costa, L.; Magalhaes-Filho, L.; Tekken, V. Ecosystem service value losses from coastal erosion in Europe: Historical trends and future projections. *J. Coast. Conserv.* **2013**, *17*, 389–395. [[CrossRef](#)]
42. Macdonald, D.; Dixon, A.; Newell, A.; Hallaways, A. Groundwater flooding within an urbanised flood plain. *J. Flood Risk Manag.* **2012**, *5*, 68–80. [[CrossRef](#)]
43. Kundzewicz, Z.W.; Pinskiwar, I.; Brakenridge, G.R. Large floods in Europe, 1985–2009. *Hydrol. Sci. J.* **2013**, *58*, 1–7. [[CrossRef](#)]
44. Kvočka, D.; Falconer, R.A.; Bray, M. Flood hazard assessment for extreme flood events. *Nat. Hazards* **2016**, *84*, 1569–1599. [[CrossRef](#)]
45. Jabbar, M.T.; Chen, X. Land degradation due to salinization in arid and semi-arid regions with the aid of geo-information techniques. *Geo-Spat. Inf. Sci.* **2008**, *11*, 112–120. [[CrossRef](#)]
46. Lv, Z.Z.; Liu, G.M.; Yang, J.S.; Zhang, M.M.; He, L.D.; Shao, H.B.; Yu, S.P. Spatial variability of soil salinity in Bohai Sea coastal wetlands, China: Partition into four management zones. *Plant Biosyst.* **2013**, *147*, 1201–1210. [[CrossRef](#)]
47. Wu, J.; Li, P.; Qian, H.; Fang, Y. Assessment of soil salinization based on a low-cost method and its influencing factors in a semi-arid agricultural area, northwest China. *Environ. Earth Sci.* **2014**, *71*, 3465–3475. [[CrossRef](#)]
48. Serran, J.N.; Creed, I.F.; Ameli, A.A.; Aldred, D.A. Estimating rates of wetland loss using power-law functions. *Wetlands* **2018**, *38*, 109–120. [[CrossRef](#)]
49. Merrifield, M.A.; Merrifield, S.T.; Mitchum, G.T. An anomalous recent acceleration of global sea level rise. *J. Clim.* **2009**, *22*, 5772–5781. [[CrossRef](#)]
50. Kopp, R.E.; Kemp, A.C.; Bittermann, K.; Horton, B.P.; Donnelly, J.P.; Gehrels, W.R.; Hay, C.C.; Mitrovica, J.X.; Morrow, E.D.; Rahmstorf, S. Temperature-driven global sea-level variability in the Common Era. *Proc. Natl. Acad. Sci. USA* **2016**, *113*, E1434–E1441. [[CrossRef](#)]
51. Hak, D.; Nadaoka, K.; Patrick Bernado, L.; Le Phu, V.; Hong Quan, N.; Quang Toan, T.; Hieu Trung, N.; Van Ni, D.; Pham Dang Tri, V. Spatio-temporal variations of sea level around the Mekong Delta: Their causes and consequences on the coastal environment. *Hydrol. Res. Lett.* **2016**, *10*, 60–66. [[CrossRef](#)]
52. Zhao, Q.; Pan, J.; Devlin, A.; Xu, Q.; Tang, M.; Li, Z.; Zamparelli, V.; Falabella, F.; Mastro, P.; Pepe, A. Integrated Analysis of the Combined Risk of Ground Subsidence, Sea Level Rise, and Natural Hazards in Coastal and Delta River Regions. *Remote Sens.* **2021**, *13*, 3431. [[CrossRef](#)]
53. Ali, Z.; Barnard, I.; Fox, P.; Duggan, P.; Gray, R.; Allan, P.; Brand, A.; Ste-Mari, R. Description of RADARSAT-2 synthetic aperture radar design. *Can. J. Remote Sens.* **2004**, *30*, 246–257. [[CrossRef](#)]
54. Li, D.; Shan, J.; Gong, J. *Geospatial Technology for Earth Observation*; Springer: New York, NY, USA, 2009.
55. De Leeuw, J.; Georgiadou, Y.; Kerle, N.; de Gier, A.; Inoue, Y.; Ferwerda, J.; Smies, M.; Narrantuya, D. The function of remote sensing in support of environmental policy. *Remote Sens.* **2010**, *2*, 1731–1750. [[CrossRef](#)]
56. Guo, H. Understanding global natural disasters and the role of earth observation. *Int. J. Digit. Earth* **2010**, *3*, 221–230. [[CrossRef](#)]
57. Li, D.; Tong, Q.; Li, R.; Gong, J.; Zhang, L. Current issues in high-resolution earth observation technology. *Sci. China-Earth Sci.* **2012**, *55*, 1043–1051. [[CrossRef](#)]
58. Caltagirone, F.; Capuzi, A.; Coletta, A.; De Luca, G.F.; Scorzafava, E.; Leonardi, R.; Rivola, S.; Fagioli, S.; Angino, G.; L'Abbate, M.; et al. The COSMO-SkyMed dual use earth observation program: Development, qualification, and results of the commissioning of the overall constellation. *IEEE J. Sel. Top. Appl. Earth Obs. Remote Sens.* **2014**, *7*, 2754–2762. [[CrossRef](#)]
59. Lulla, K.; Nellis, M.D.; Rundquist, B. Innovations in geospatial technologies: Cubesats for earth observations. *Geocarto Int.* **2014**, *29*, 821. [[CrossRef](#)]
60. Guo, H.; Zhang, I.; Zhu, L. Earth observation big data for climate change research. *Adv. Clim. Chang. Res.* **2015**, *6*, 108–117. [[CrossRef](#)]
61. Yang, F.; Han, Y.; Xuan, Y. Large-scale earth surface thermal radiative features in space observation. *Opt. Commun.* **2015**, *348*, 77–84. [[CrossRef](#)]
62. Tomas, R.; Li, Z. Earth observations for geohazards: Present and future challenges. *Remote Sens.* **2017**, *9*, 194. [[CrossRef](#)]
63. Peral, E.; Im, E.; Wye, L.; Lee, S.; Tanelli, S.; Rahmat-Samii, Y.; Horst, S.; Hoffman, J.; Yun, S.-H.; Imken, T.; et al. Radar technologies for earth remote sensing from cubesat platforms. *Proc. IEEE* **2018**, *106*, 404–418. [[CrossRef](#)]
64. Leibrand, A.; Sadoff, N.; Maslak, T.; Thomas, A. Using earth observations to help developing countries improve access to reliable, sustainable, and modern energy. *Front. Environ. Sci.* **2019**, *7*, 123. [[CrossRef](#)]
65. Dai, K.; Li, Z.; Xu, Q.; Burgmann, R.; Milledge, D.G.; Tomas, R.; Fan, X.; Zhao, C.; Liu, X.; Peng, J.; et al. Entering the era of earth observation-based landslide warning systems: A Novel and exciting framework. *IEEE Geosci. Remote Sens. Mag.* **2020**, *8*, 136–153. [[CrossRef](#)]
66. Gomes, V.C.F.; Queiroz, G.R.; Ferreira, K.R. An overview of platforms for big earth observation data management and analysis. *Remote Sens.* **2020**, *12*, 1253. [[CrossRef](#)]
67. Platnick, S.; King, M.D.; Ackerman, S.A.; Menzel, W.P.; Baum, B.A.; Riedi, J.C.; Frey, R.A. The MODIS cloud products: Algorithms and examples from Terra. *IEEE Trans. Geosci. Remote Sens.* **2003**, *41*, 459–473. [[CrossRef](#)]

68. Ferguson, C.R.; Wood, E.F. Observed land-atmosphere coupling from satellite remote sensing and reanalysis. *J. Hydrometeorol.* **2011**, *12*, 1221–1254. [[CrossRef](#)]
69. Kato, S.; Rose, F.G.; Sun-Mack, S.; Miller, W.F.; Chen, Y.; Rutan, D.A.; Stephens, G.L.; Loeb, N.G.; Minnis, P.; Wielicki, B.A.; et al. Improvements of top-of-atmosphere and surface irradiance computations with CALIPSO-, CloudSat-, and MODIS-derived cloud and aerosol properties. *J. Geophys. Res. Atmos.* **2011**, *116*. [[CrossRef](#)]
70. Massonnet, D.; Feigl, K.L. Radar interferometry and its application to changes in the earth's surface. *Rev. Geophys.* **1998**, *36*, 441–500. [[CrossRef](#)]
71. Gudmundsson, S.; Sigmundsson, F.; Carstensen, J.M. Three-dimensional surface motion maps estimated from combined interferometric synthetic aperture radar and GPS data. *J. Geophys. Res. Solid Earth* **2002**, *107*, 2250. [[CrossRef](#)]
72. Tralli, D.M.; Blom, R.G.; Zlotnicki, V.; Donnellan, A.; Evans, D.L. Satellite remote sensing of earthquake, volcano, flood, landslide and coastal inundation hazards. *ISPRS-J. Photogramm. Remote Sens.* **2005**, *59*, 185–198. [[CrossRef](#)]
73. Tronin, A.A. Satellite remote sensing in seismology. A review. *Remote Sens.* **2010**, *2*, 124–150. [[CrossRef](#)]
74. Geirsson, H.; LaFemina, P.; Arnadottir, T.; Sturkell, E.; Sigmundsson, F.; Travis, M.; Schmidt, P.; Lund, B.; Hreinsdottir, S.; Bennett, R. Volcano deformation at active plate boundaries: Deep magma accumulation at Hekla volcano and plate boundary deformation in south Iceland. *J. Geophys. Res. Solid Earth* **2012**, *117*, B11409. [[CrossRef](#)]
75. Pinel, V.; Poland, M.P.; Hooper, A. Volcanology: Lessons learned from synthetic aperture radar imagery. *J. Volcanol. Geotherm. Res.* **2014**, *289*, 81–113. [[CrossRef](#)]
76. Osmanoglu, B.; Sunar, F.; Wdowinski, S.; Cabral-Cano, E. Time series analysis of InSAR data: Methods and trends. *ISPRS-J. Photogramm. Remote Sens.* **2016**, *115*, 90–102. [[CrossRef](#)]
77. Esaias, W.E.; Abbott, M.R.; Barton, I.; Brown, O.B.; Campbell, J.W.; Carder, K.L.; Clark, D.K.; Evans, R.H.; Hoge, F.E.; Gordon, H.R.; et al. An overview of MODIS capabilities for ocean science observations. *IEEE Trans. Geosci. Remote Sens.* **1998**, *36*, 1250–1265. [[CrossRef](#)]
78. Font, J.; Camps, A.; Borges, A.; Martín-Neira, M.; Boutin, J.; Reul, N.; Kerr, Y.H.; Hahne, A.; Mecklenburg, S. SMOS: The challenging sea surface salinity measurement from space. *Proc. IEEE* **2009**, *98*, 649–665. [[CrossRef](#)]
79. Tyler, A.N.; Hunter, P.D.; Spyarakos, E.; Groom, S.; Constantinescu, A.M.; Kitchen, J. Developments in earth observation for the assessment and monitoring of inland, transitional, coastal and shelf-sea waters. *Sci. Total Environ.* **2016**, *572*, 1307–1321. [[CrossRef](#)]
80. Straub, D.W.; Welke, R.J. Coping with systems risk: Security planning models for management decision making. *MIS Q.* **1998**, *22*, 441–469. [[CrossRef](#)]
81. Comfort, L.K. Risk, security, and disaster management. *Annu. Rev. Political Sci.* **2005**, *8*, 335–356. [[CrossRef](#)]
82. Liliberto, M.; Dario Cardona, O.; Barbat, A.H. A disaster risk management performance index. *Nat. Hazards* **2007**, *41*, 1–20. [[CrossRef](#)]
83. Voigt, S.; Kemper, T.; Riedlinger, T.; Kiefl, R.; Scholte, K.; Mehl, H. Satellite image analysis for disaster and crisis-management support. *IEEE Trans. Geosci. Remote Sens.* **2007**, *45*, 1520–1528. [[CrossRef](#)]
84. Manuj, I.; Mentzer, J.T. Global supply chain risk management strategies. *Int. J. Phys. Distrib. Logist. Manag.* **2008**, *38*, 192–223. [[CrossRef](#)]
85. Birkmann, J.; von Teichman, K. Integrating disaster risk reduction and climate change adaptation: Key challenges-scales, knowledge, and norms. *Sustain. Sci.* **2010**, *5*, 171–184. [[CrossRef](#)]
86. Kaplan, S.; Garrick, B.J. On the quantitative definition of risk. *Risk Anal.* **1981**, *1*, 11–27. [[CrossRef](#)]
87. Alexander, D. From civil defence to civil protection—And back again. *Disaster Prev. Manag.* **2002**, *11*, 209–213. [[CrossRef](#)]
88. Haddow, G.D.; Bullock, J.A. *Introduction to Emergency Management*; Butterworth-Heinemann: Oxford, UK, 2003.
89. Coppola, D.P. *Introduction to International Disaster Management*; Elsevier: Amsterdam, The Netherlands, 2006.
90. Manfre, L.A.; Hirata, E.; Silva, J.B.; Shinohara, E.J.; Giannotti, M.A.; Larocca, A.P.C.; Quintanilha, J.A. An analysis of geospatial technologies for risk and natural disaster management. *ISPRS Int. J. Geo-Inf.* **2012**, *1*, 166–185. [[CrossRef](#)]
91. Gill, J.C.; Malamud, B.D. Hazard interactions and interaction networks (cascades) within multi-hazard methodologies. *Earth Syst. Dyn.* **2016**, *7*, 659–679. [[CrossRef](#)]
92. Molina, M.; Bayarri, S. A multinational SDI-based system to facilitate disaster risk management in the Andean Community. *Comput. Geosci.* **2011**, *37*, 1501–1510. [[CrossRef](#)]
93. Garcia, J.A.; Istomin, E.P.; Slesarev, L.S.; Pena, J.A. Spatial Data Infrastructure for the Management and Risk Assessment of Natural Disasters. In Proceedings of the 6th International Conference on Remote Sensing and Geoinformation of the Environment (RSCy), Paphos, Cyprus, 26–29 March 2018.
94. Higgins, S.A. Review: Advances in delta-subsidence research using satellite methods. *Hydrogeol. J.* **2016**, *24*, 587–600. [[CrossRef](#)]
95. Metternicht, G.; Hurni, L.; Gogu, R. Remote sensing of landslides: An analysis of the potential contribution to geo-spatial systems for hazard assessment in mountainous environments. *Remote Sens. Environ.* **2005**, *98*, 284–303. [[CrossRef](#)]
96. Hong, Y.; Adler, R.F.; Huffman, G. An experimental global prediction system for rainfall-triggered landslides using satellite remote sensing and geospatial datasets. *IEEE Trans. Geosci. Remote Sens.* **2007**, *45*, 1671–1680. [[CrossRef](#)]
97. Myint, S.W.; Yuan, M.; Cerveny, R.S.; Giri, C. Categorizing natural disaster damage assessment using satellite-based geospatial techniques. *Nat. Hazards Earth Syst. Sci.* **2008**, *8*, 707–719. [[CrossRef](#)]

98. Khan, S.I.; Hong, Y.; Wang, J.; Yilmaz, K.K.; Gourley, J.J.; Adler, R.F.; Brakenridge, G.R.; Policelli, F.; Habib, S.; Irwin, D. Satellite remote sensing and hydrologic modeling for flood inundation mapping in Lake Victoria Basin: Implications for hydrologic prediction in Ungauged Basins. *IEEE Trans. Geosci. Remote Sens.* **2011**, *49*, 85–95. [[CrossRef](#)]
99. Drusch, M.; Del Bello, U.; Carlier, S.; Colin, O.; Fernandez, V.; Gascon, F.; Hoersch, B.; Isola, C.; Laberinti, P.; Martimort, P.; et al. Sentinel-2: ESA's optical high-resolution mission for GMES operational services. *Remote Sens. Environ.* **2012**, *120*, 25–36. [[CrossRef](#)]
100. Torres, R.; Snoeij, P.; Geudtner, D.; Bibby, D.; Davidson, M.; Attema, E.; Potin, P.; Rommen, B.; Floury, N.; Brown, M.; et al. GMES Sentinel-1 mission. *Remote Sens. Environ.* **2012**, *120*, 9–24. [[CrossRef](#)]
101. Novellino, A.; Jordan, C.; Ager, G.; Bateson, L.; Fleming, C.; Confuorto, P. Remote sensing for natural or man-made disasters and environmental changes. In *Geological Disaster Monitoring Based on Sensor Networks*; Springer: Singapore, 2019; pp. 23–31.
102. Zhu, Z.; Woodcock, C.E. Continuous change detection and classification of land cover using all available Landsat data. *Remote Sens. Environ.* **2014**, *144*, 152–171. [[CrossRef](#)]
103. Zhu, Z. Change detection using landsat time series: A review of frequencies, preprocessing, algorithms, and applications. *ISPRS-J. Photogramm. Remote Sens.* **2017**, *130*, 370–384. [[CrossRef](#)]
104. Gao, F.; Hilker, T.; Zhu, X.; Anderson, M.C.; Masek, J.G.; Wang, P.; Yang, Y. Fusing Landsat and MODIS data for vegetation monitoring. *IEEE Geosci. Remote Sens. Mag.* **2015**, *3*, 47–60. [[CrossRef](#)]
105. Loveland, T.R.; Irons, J.R. Landsat 8: The plans, the reality, and the legacy. *Remote Sens. Environ.* **2016**, *185*, 1–6. [[CrossRef](#)]
106. Li, J.; Roy, D.P. A global analysis of Sentinel-2A, Sentinel-2B and Landsat-8 data revisit intervals and implications for terrestrial monitoring. *Remote Sens.* **2017**, *9*, 902. [[CrossRef](#)]
107. Wulder, M.A.; Hilker, T.; White, J.C.; Coops, N.C.; Masek, J.G.; Pflugmacher, D.; Crevier, Y. Virtual constellations for global terrestrial monitoring. *Remote Sens. Environ.* **2015**, *170*, 62–76. [[CrossRef](#)]
108. Franceschetti, G.; Lanari, R. *Synthetic Aperture Radar Processing*; CRC Press: Boca Raton, FL, USA, 1999.
109. Ferretti, A.; Fumagalli, A.; Novali, F.; Prati, C.; Rocca, F.; Rucci, A. A new algorithm for processing interferometric data-stacks: SqueeSAR. *IEEE Trans. Geosci. Remote Sens.* **2011**, *49*, 3460–3470. [[CrossRef](#)]
110. Berardino, P.; Fornaro, G.; Lanari, R.; Sansosti, E. A new algorithm for surface deformation monitoring based on small baseline differential SAR interferograms. *IEEE Trans. Geosci. Remote Sens.* **2002**, *40*, 2375–2383. [[CrossRef](#)]
111. Mora, O.; Mallorqui, J.J.; Broquetas, A. Linear and nonlinear terrain deformation maps from a reduced set of interferometric SAR images. *IEEE Trans. Geosci. Remote Sens.* **2003**, *41*, 2243–2253. [[CrossRef](#)]
112. Shanker, P.; Zebker, H. Persistent scatterer selection using maximum likelihood estimation. *Geophys. Res. Lett.* **2007**, *34*, L22301. [[CrossRef](#)]
113. Hooper, A. A multi-temporal InSAR method incorporating both persistent scatterer and small baseline approaches. *Geophys. Res. Lett.* **2008**, *35*, L16302. [[CrossRef](#)]
114. Adam, N.; Rodriguez Gonzalez, F.; Parizzi, A.; Liebhart, W. Wide Area Persistent Scatterer Interferometry. In Proceedings of the IGARSS 2011—2011 IEEE International Geoscience and Remote Sensing Symposium, Vancouver, BC, Canada, 24–29 July 2011; pp. 1481–1484.
115. Hetland, E.A.; Muse, P.; Simons, M.; Lin, Y.N.; Agram, P.S.; DiCaprio, C.J. Multiscale InSAR Time Series (MInTS) analysis of surface deformation. *J. Geophys. Res. Solid Earth* **2012**, *117*, B02404. [[CrossRef](#)]
116. Crosetto, M.; Monserrat, O.; Cuevas-Gonzalez, M.; Devanthery, N.; Crippa, B. Persistent scatterer interferometry: A review. *ISPRS-J. Photogramm. Remote Sens.* **2016**, *115*, 78–89. [[CrossRef](#)]
117. Dong, J.; Zhang, L.; Tang, M.; Liao, M.; Xu, Q.; Gong, J.; Ao, M. Mapping landslide surface displacements with time series SAR interferometry by combining persistent and distributed scatterers: A case study of Jiaju landslide in Danba, China. *Remote Sens. Environ.* **2018**, *205*, 180–198. [[CrossRef](#)]
118. Even, M.; Schulz, K. InSAR deformation analysis with distributed scatterers: A review complemented by new advances. *Remote Sens.* **2018**, *10*, 744. [[CrossRef](#)]
119. Falabella, F.; Serio, C.; Zeni, G.; Pepe, A. On the use of weighted least-squares approaches for differential Interferometric SAR analyses: The weighted adaptive variable-length (WAVE) technique. *Sensors* **2020**, *20*, 1103. [[CrossRef](#)]
120. Chapron, B.; Collard, F.; Arduin, F. Direct measurements of ocean surface velocity from space: Interpretation and validation. *J. Geophys. Res. Oceans* **2005**, *110*, C07008. [[CrossRef](#)]
121. Pierdicca, N.; Pulvirenti, L.; Chini, M. Dealing with flood mapping using SAR data in the presence of wind or heavy precipitation. *SPIE Remote Sens.* **2013**, *8891*, 88910K. [[CrossRef](#)]
122. Danklmayer, A.; Chandra, M. Precipitation induced signatures in SAR images. In Proceedings of the 2009 3rd European Conference on Antennas and Propagation EuCAP, Berlin, Germany, 23–27 March 2009; pp. 3433–3437.
123. Klees, R.; Massonnet, D. Deformation measurements using SAR interferometry: Potential and limitations. *Geol. En Mijnb.* **1998**, *77*, 161–176. [[CrossRef](#)]
124. Just, D.; Bamler, R. Phase statistics of interferograms with applications to synthetic aperture radar. *Appl. Optics* **1994**, *33*, 4361–4368. [[CrossRef](#)]
125. Lee, H.; Liu, J.G. Analysis of topographic decorrelation in SAR interferometry using ratio coherence imagery. *IEEE Trans. Geosci. Remote Sens.* **2001**, *39*, 223–232. [[CrossRef](#)]

126. Tessler, Z.D.; Voeroesmarly, C.J.; Grossberg, M.; Gladkova, I.; Aizenman, H.; Syvitski, J.P.M.; Foufoula-Georgiou, E. Profiling risk and sustainability in coastal deltas of the world. *Science* **2015**, *349*, 638–643. [[CrossRef](#)]
127. GEBCO. *The GEBCO_2020 Grid—A Continuous Terrain Model of the Global Oceans and Land*; British Oceanographic Data Centre, National Oceanography Centre: Liverpool, UK, 2020. [[CrossRef](#)]
128. Zhang, T.; Yang, X.; Hu, S.; Su, F. Extraction of coastline in aquaculture coast from multispectral remote sensing images: Object-Based region growing integrating edge detection. *Remote Sens.* **2013**, *5*, 4470–4487. [[CrossRef](#)]
129. Garcia-Rubio, G.; Huntley, D.; Russell, P. Evaluating shoreline identification using optical satellite images. *Mar. Geol.* **2015**, *359*, 96–105. [[CrossRef](#)]
130. Pardo-Pascual, J.E.; Sanchez-Garcia, E.; Almonacid-Caballer, J.; Palomar-Vazquez, J.M.; Priego de los Santos, E.; Fernandez-Sarria, A.; Balaguer-Beser, A. Assessing the accuracy of automatically extracted shorelines on microtidal beaches from Landsat 7, Landsat 8 and Sentinel-2 imagery. *Remote Sens.* **2018**, *10*, 326. [[CrossRef](#)]
131. Besset, M.; Anthony, E.J.; Bouchette, F. Multi-decadal variations in delta shorelines and their relationship to river sediment supply: An assessment and review. *Earth-Sci. Rev.* **2019**, *193*, 199–219. [[CrossRef](#)]
132. Toure, S.; Diop, O.; Kpalma, K.; Maiga, A.S. Shoreline detection using optical remote sensing: A review. *ISPRS Int. J. Geo-Inf.* **2019**, *8*, 75. [[CrossRef](#)]
133. El-Asmar, H.M.; Hereher, M.E. Change detection of the coastal zone east of the Nile Delta using remote sensing. *Environ. Earth Sci.* **2011**, *62*, 769–777. [[CrossRef](#)]
134. Pacheco, A.; Horta, J.; Loureiro, C.; Ferreira, O. Retrieval of nearshore bathymetry from Landsat 8 images: A tool for coastal monitoring in shallow waters. *Remote Sens. Environ.* **2015**, *159*, 102–116. [[CrossRef](#)]
135. Sun, N.; Zhu, W.; Cheng, Q. GF-1 and Landsat observed a 40-year wetland spatiotemporal variation and its coupled environmental factors in Yangtze River estuary. *Estuar. Coast. Shelf Sci.* **2018**, *207*, 30–39. [[CrossRef](#)]
136. Jiao, L.; Sun, W.; Yang, G.; Ren, G.; Liu, Y. A hierarchical classification framework of satellite multispectral/hyperspectral images for mapping coastal wetlands. *Remote Sens.* **2019**, *11*, 2238. [[CrossRef](#)]
137. Hereher, M.E. Mapping coastal erosion at the Nile Delta western promontory using Landsat imagery. *Environ. Earth Sci.* **2011**, *64*, 1117–1125. [[CrossRef](#)]
138. Kuenzer, C.; Heimhuber, V.; Huth, J.; Dech, S. Remote Sensing for the Quantification of Land Surface Dynamics in Large River Delta Regions-A Review. *Remote Sens.* **2019**, *11*, 1985. [[CrossRef](#)]
139. Seto, K.C.; Woodcock, C.; Song, C.; Huang, X.; Lu, J.; Kaufmann, R. Monitoring land-use change in the Pearl River Delta using Landsat TM. *Int. J. Remote Sens.* **2002**, *23*, 1985–2004. [[CrossRef](#)]
140. Gao, F.; De Colstoun, E.B.; Ma, R.; Weng, Q.; Masek, J.G.; Chen, J.; Pan, Y.; Song, C. Mapping impervious surface expansion using medium-resolution satellite image time series: A case study in the Yangtze River Delta, China. *Int. J. Remote Sens.* **2012**, *33*, 7609–7628. [[CrossRef](#)]
141. Xian, G.; Homer, C.; Bunde, B.; Danielson, P.; Dewitz, J.; Fry, J.; Pu, R. Quantifying urban land cover change between 2001 and 2006 in the Gulf of Mexico region. *Geocarto Int.* **2012**, *27*, 479–497. [[CrossRef](#)]
142. Ottinger, M.; Kuenzer, C.; Liu, G.; Wang, S.; Dech, S. Monitoring land cover dynamics in the Yellow River Delta from 1995 to 2010 based on Landsat 5 TM. *Appl. Geogr.* **2013**, *44*, 53–68. [[CrossRef](#)]
143. Sica, Y.V.; Quintana, R.D.; Radeloff, V.C.; Gavier-Pizarro, G.I. Wetland loss due to land use change in the Lower Parana River Delta, Argentina. *Sci. Total Environ.* **2016**, *568*, 967–978. [[CrossRef](#)]
144. Zhang, L.; Weng, Q. Annual dynamics of impervious surface in the Pearl River Delta, China, from 1988 to 2013, using time series Landsat imagery. *ISPRS-J. Photogramm. Remote Sens.* **2016**, *113*, 86–96. [[CrossRef](#)]
145. Haas, J.; Ban, Y. Urban growth and environmental impacts in Jing-Jin-Ji, the Yangtze, River Delta and the Pearl River Delta. *Int. J. Appl. Earth Obs. Geoinf.* **2014**, *30*, 42–55. [[CrossRef](#)]
146. Liu, S.; Li, X.; Chen, D.; Duan, Y.; Ji, H.; Zhang, L.; Chai, Q.; Hu, X. Understanding Land use/Land cover dynamics and impacts of human activities in the Mekong Delta over the last 40 years. *Glob. Ecol. Conserv.* **2020**, *22*, e00991. [[CrossRef](#)]
147. Vidal, A.; Rocio Moreno, M. Change detection of isolated housing using a new hybrid approach based on object classification with optical and TerraSAR-X data. *Int. J. Remote Sens.* **2011**, *32*, 9621–9635. [[CrossRef](#)]
148. Brisco, B.; Schmitt, A.; Murnaghan, K.; Kaya, S.; Roth, A. SAR polarimetric change detection for flooded vegetation. *Int. J. Digit. Earth* **2013**, *6*, 103–114. [[CrossRef](#)]
149. Ulaby, F.T.; Long, D.G. *Microwave Radar and Radiometric Remote Sensing*; The University of Michigan Press: Ann Arbor, MI, USA, 2014.
150. Lavelle, M.; Simard, M.; Hensley, S. A temporal decorrelation model for polarimetric radar interferometers. *IEEE Trans. Geosci. Remote Sens.* **2012**, *50*, 2880–2888. [[CrossRef](#)]
151. Bouaraba, A.; Younsi, A.; Belhadj-Aissa, A.; Acheroy, M.; Milisavljevic, N.; Closson, D. Robust techniques for coherent change detection using COSMO-SkyMed SAR images. *Prog. Electromagn. Res. M* **2012**, *22*, 219–232. [[CrossRef](#)]
152. Zebker, H.A.; Villasenor, J. Decorrelation in interferometric radar echoes. *IEEE Trans. Geosci. Remote Sens.* **1992**, *30*, 950–959. [[CrossRef](#)]
153. Shinozuka, M.; Ghanem, R.; Houshmand, B.; Mansouri, B. Damage detection in urban areas by SAR imagery. *J. Eng. Mech.* **2000**, *126*, 769–777. [[CrossRef](#)]

154. Sabry, R. A new coherency formalism for change detection and phenomenology in SAR imagery: A field approach. *IEEE Geosci. Remote Sens. Lett.* **2009**, *6*, 458–462. [[CrossRef](#)]
155. Carotenuto, V.; De Maio, A.; Clemente, C.; Soraghan, J.J. Invariant rules for multipolarization SAR change detection. *IEEE Trans. Geosci. Remote Sens.* **2015**, *53*, 3294–3311. [[CrossRef](#)]
156. Cha, M.; Phillips, R.D.; Wolfe, P.J.; Richmond, C.D. Two-Stage change detection for synthetic aperture radar. *IEEE Trans. Geosci. Remote Sens.* **2015**, *53*, 6547–6560. [[CrossRef](#)]
157. Zhang, Q.; Antoniou, M.; Chang, W.; Cherniakov, M. Spatial decorrelation in GNSS-based SAR coherent change detection. *IEEE Trans. Geosci. Remote Sens.* **2015**, *53*, 219–228. [[CrossRef](#)]
158. Ciunozzo, D.; Carotenuto, V.; De Maio, A. On multiple covariance equality testing with application to SAR change detection. *IEEE Trans. Signal Process.* **2017**, *65*, 5078–5091. [[CrossRef](#)]
159. Mahdavi, S.; Salehi, B.; Granger, J.; Amani, M.; Brisco, B.; Huang, W. Remote sensing for wetland classification: A comprehensive review. *GISci. Remote Sens.* **2018**, *55*, 623–658. [[CrossRef](#)]
160. Ozesmi, S.L.; Bauer, M.E. Satellite remote sensing of wetlands. *Wetl. Ecol. Manag.* **2002**, *10*, 381–402. [[CrossRef](#)]
161. Ryu, J.-H.; Kim, C.-H.; Lee, Y.-K.; Won, J.-S.; Chun, S.-S.; Lee, S. Detecting the intertidal morphologic change using satellite data. *Estuar. Coast. Shelf Sci.* **2008**, *78*, 623–632. [[CrossRef](#)]
162. Li, X.; Damen, M.C.J. Coastline change detection with satellite remote sensing for environmental management of the Pearl River Estuary, China. *J. Mar. Syst.* **2010**, *82*, S54–S61. [[CrossRef](#)]
163. Kuenzer, C.; Ottinger, M.; Liu, G.; Sun, B.; Baumhauer, R.; Dech, S. Earth observation-based coastal zone monitoring of the Yellow River Delta: Dynamics in China’s second largest oil producing region over four decades. *Appl. Geogr.* **2014**, *55*, 92–107. [[CrossRef](#)]
164. Li, X.; Zhou, Y.; Zhang, L.; Kuang, R. Shoreline change of Chongming Dongtan and response to river sediment load: A remote sensing assessment. *J. Hydrol.* **2014**, *511*, 432–442. [[CrossRef](#)]
165. Ghosh, M.K.; Kumar, L.; Roy, C. Monitoring the coastline change of Hatiya Island in Bangladesh using remote sensing techniques. *ISPRS-J. Photogramm. Remote Sens.* **2015**, *101*, 137–144. [[CrossRef](#)]
166. Jong-sen, L.; Jurkevich, I. Coastline detection and tracing in SAR images. *IEEE Trans. Geosci. Remote Sens.* **1990**, *28*, 662–668. [[CrossRef](#)]
167. Boak, E.H.; Turner, I.L. Shoreline definition and detection: A review. *J. Coast. Res.* **2005**, *21*, 688–703. [[CrossRef](#)]
168. Liu, H.; Jezek, K.C. Automated extraction of coastline from satellite imagery by integrating Canny edge detection and locally adaptive thresholding methods. *Int. J. Remote Sens.* **2004**, *25*, 937–958. [[CrossRef](#)]
169. Pardo-Pascual, J.E.; Almonacid-Caballer, J.; Ruiz, L.A.; Palomar-Vazquez, J. Automatic extraction of shorelines from Landsat TM and ETM+ multi-temporal images with subpixel precision. *Remote Sens. Environ.* **2012**, *123*, 1–11. [[CrossRef](#)]
170. Li, R.; Liu, W.; Yang, L.; Sun, S.; Hu, W.; Zhang, F.; Li, W. DeepUNet: A deep fully convolutional network for pixel-level sea-land segmentation. *IEEE J. Sel. Top. Appl. Earth Obs. Remote Sens.* **2018**, *11*, 3954–3962. [[CrossRef](#)]
171. Bishop-Taylor, R.; Sagar, S.; Lymburner, L.; Alam, I.; Sixsmith, J. Sub-Pixel waterline extraction: Characterising accuracy and sensitivity to Indices and spectra. *Remote Sens.* **2019**, *11*, 2984. [[CrossRef](#)]
172. Chen, C.; Fu, J.; Zhang, S.; Zhao, X. Coastline information extraction based on the tasseled cap transformation of Landsat-8 OLI images. *Estuar. Coast. Shelf Sci.* **2019**, *217*, 281–291. [[CrossRef](#)]
173. Sanchez-Garcia, E.; Balaguer-Beser, A.; Almonacid-Caballer, J.; Eliseu Pardo-Pascual, J. A new adaptive image interpolation method to define the shoreline at sub-pixel level. *Remote Sens.* **2019**, *11*, 1880. [[CrossRef](#)]
174. Viana-Borja, S.P.; Ortega-Sanchez, M. Automatic methodology to detect the coastline from Landsat Images with a new water index assessed on three different Spanish Mediterranean Deltas. *Remote Sens.* **2019**, *11*, 2186. [[CrossRef](#)]
175. Li, W.; Gong, P. Continuous monitoring of coastline dynamics in western Florida with a 30-year time series of Landsat imagery. *Remote Sens. Environ.* **2016**, *179*, 196–209. [[CrossRef](#)]
176. Wang, K. Evolution of Yellow River Delta coastline based on remote sensing from 1976 to 2014, China. *Chin. Geogr. Sci.* **2019**, *29*, 181–191. [[CrossRef](#)]
177. Di, K.; Wang, J.; Ma, R.; Li, R. Automatic shoreline extraction from high-resolution IKONOS satellite imagery. In Proceedings of the ASPRS 2003 Annual Conference, Anchorage, AK, USA, 5–9 May 2003.
178. Sekovski, I.; Stecchi, F.; Mancini, F.; Del Rio, L. Image classification methods applied to shoreline extraction on very high-resolution multispectral imagery. *Int. J. Remote Sens.* **2014**, *35*, 3556–3578. [[CrossRef](#)]
179. Dai, C.; Howat, I.M.; Larour, E.; Husby, E. Coastline extraction from repeat high resolution satellite imagery. *Remote Sens. Environ.* **2019**, *229*, 260–270. [[CrossRef](#)]
180. Dellepiane, S.; De Laurentiis, R.; Giordano, F. Coastline extraction from SAR images and a method for the evaluation of the coastline precision. *Pattern Recognit. Lett.* **2004**, *25*, 1461–1470. [[CrossRef](#)]
181. Morton, R.A.; Bernier, J.C.; Barras, J.A. Evidence of regional subsidence and associated interior wetland loss induced by hydrocarbon production, Gulf Coast region, USA. *Environ. Geol.* **2006**, *50*, 261–274. [[CrossRef](#)]
182. Perissin, D.; Wang, Z.; Lin, H. Shanghai subway tunnels and highways monitoring through Cosmo-SkyMed Persistent Scatterers. *ISPRS-J. Photogramm. Remote Sens.* **2012**, *73*, 58–67. [[CrossRef](#)]
183. Kim, S.W.; Lee, C.W.; Song, K.Y.; Min, K.D.; Won, J.S. Application of L-band differential SAR interferometry to subsidence rate estimation in reclaimed coastal land. *Int. J. Remote Sens.* **2005**, *26*, 1363–1381. [[CrossRef](#)]

184. Gao, G.D.; Wang, X.H.; Bao, X.W. Land reclamation and its impact on tidal dynamics in Jiaozhou Bay, Qingdao, China. *Estuar. Coast. Shelf Sci.* **2014**, *151*, 285–294. [[CrossRef](#)]
185. Zhao, Q.; Pepe, A.; Gao, W.; Lu, Z.; Bonano, M.; He, M.L.; Wang, J.; Tang, X. A DInSAR investigation of the ground settlement time evolution of ocean-reclaimed lands in Shanghai. *IEEE J. Sel. Top. Appl. Earth Obs. Remote Sens.* **2015**, *8*, 1763–1781. [[CrossRef](#)]
186. Tian, B.; Wu, W.; Yang, Z.; Zhou, Y. Drivers, trends, and potential impacts of long-term coastal reclamation in China from 1985 to 2010. *Estuar. Coast. Shelf Sci.* **2016**, *170*, 83–90. [[CrossRef](#)]
187. Zhao, Q.; Ma, G.; Wang, Q.; Yang, T.; Liu, M.; Gao, W.; Falabella, F.; Mastro, P.; Pepe, A. Generation of long-term InSAR ground displacement time-series through a novel multi-sensor data merging technique: The case study of the Shanghai coastal area. *ISPRS-J. Photogramm. Remote Sens.* **2019**, *154*, 10–27. [[CrossRef](#)]
188. Gens, R.; VanGenderen, J.L. SAR interferometry—Issues, techniques, applications. *Int. J. Remote Sens.* **1996**, *17*, 1803–1835. [[CrossRef](#)]
189. Bamler, R.; Hartl, P. Synthetic aperture radar interferometry. *Inverse Probl.* **1998**, *14*, R1. [[CrossRef](#)]
190. Pepe, A.; Calo, F. A review of interferometric synthetic aperture RADAR (InSAR) multi-track approaches for the retrieval of earth's surface displacements. *Appl. Sci.* **2017**, *7*, 1264. [[CrossRef](#)]
191. Hu, J.; Li, Z.W.; Ding, X.L.; Zhu, J.J.; Zhang, L.; Sun, Q. Resolving three-dimensional surface displacements from InSAR measurements: A review. *Earth-Sci. Rev.* **2014**, *133*, 1–17. [[CrossRef](#)]
192. Xue, F.; Lv, X.; Dou, F.; Yun, Y. A review of time-series interferometric SAR techniques: A tutorial for surface deformation analysis. *IEEE Geosci. Remote Sens. Mag.* **2020**, *8*, 22–42. [[CrossRef](#)]
193. Gabriel, A.K.; Goldstein, R.M.; Zebker, H.A. Mapping small elevation changes over large areas: Differential radar interferometry. *J. Geophys. Res.* **1989**, *94*, 9183–9191. [[CrossRef](#)]
194. Tesauro, M.; Bernardino, P.; Lanari, R.; Sansosti, E.; Fornaro, G.; Franceschetti, G. Urban subsidence inside the city of Napoli (Italy) observed by satellite radar interferometry. *Geophys. Res. Lett.* **2000**, *27*, 1961–1964. [[CrossRef](#)]
195. Lopez-Quiroz, P.; Doin, M.-P.; Tupin, F.; Briole, P.; Nicolas, J.-M. Time series analysis of Mexico City subsidence constrained by radar interferometry. *J. Appl. Geophys.* **2009**, *69*, 1–15. [[CrossRef](#)]
196. Zhang, B.; Wang, R.; Deng, Y.; Ma, P.; Lin, H.; Wang, J. Mapping the Yellow River Delta land subsidence with multitemporal SAR interferometry by exploiting both persistent and distributed scatterers. *ISPRS-J. Photogramm. Remote Sens.* **2019**, *148*, 157–173. [[CrossRef](#)]
197. Ferretti, A.; Prati, C.; Rocca, F. Permanent scatterers in SAR interferometry. *IEEE Trans. Geosci. Remote Sens.* **2001**, *39*, 8–20. [[CrossRef](#)]
198. Ferretti, A.; Prati, C.; Rocca, F. Nonlinear subsidence rate estimation using permanent scatterers in differential SAR interferometry. *IEEE Trans. Geosci. Remote Sens.* **2000**, *38*, 2202–2212. [[CrossRef](#)]
199. Werner, C.; Wegmuller, U.; Strozzi, T.; Wiesmann, A. Interferometric Point Target Analysis for Deformation Mapping. In Proceedings of the IGARSS 2003, Toulouse, France, 21–25 July 2003; pp. 4362–4364.
200. Hooper, A.; Zebker, H.; Segall, P.; Kampes, B. A new method for measuring deformation on volcanoes and other natural terrains using InSAR persistent scatterers. *Geophys. Res. Lett.* **2004**, *31*, L23611. [[CrossRef](#)]
201. Kampes, B.M. *Radar Interferometry*; Springer: Dordrecht, The Netherlands, 2006; Volume 12.
202. Sadeghi, Z.; Zoj, M.J.V.; Dehghani, M. An improved persistent scatterer interferometry for subsidence monitoring in the Tehran Basin. *IEEE J. Sel. Top. Appl. Earth Obs. Remote Sens.* **2013**, *6*, 1571–1577. [[CrossRef](#)]
203. Devanthery, N.; Crosetto, M.; Monserrat, O.; Cuevas-González, M.; Crippa, B. An approach to persistent scatterer interferometry. *Remote Sens.* **2014**, *6*, 6662–6679. [[CrossRef](#)]
204. Foroughnia, F.; Nemati, S.; Maghsoudi, Y.; Perissin, D. An iterative PS-InSAR method for the analysis of large spatio-temporal baseline data stacks for land subsidence estimation. *Int. J. Appl. Earth Obs. Geoinf.* **2019**, *74*, 248–258. [[CrossRef](#)]
205. Zhang, L.; Ding, X.; Lu, Z. Modeling PSInSAR time series without phase unwrapping. *IEEE Trans. Geosci. Remote Sens.* **2011**, *49*, 547–556. [[CrossRef](#)]
206. Schmidt, D.A.; Bürgmann, R. Time-dependent land uplift and subsidence in the Santa Clara valley, California, from a large interferometric synthetic aperture radar data set. *J. Geophys. Res. Solid Earth* **2003**, *108*, 2416. [[CrossRef](#)]
207. Crosetto, M.; Crippa, B.; Biescas, E. Early detection and in-depth analysis of deformation phenomena by radar interferometry. *Eng. Geol.* **2005**, *79*, 81–91. [[CrossRef](#)]
208. Biggs, J.; Wright, T.; Lu, Z.; Parsons, B. Multi-interferogram method for measuring interseismic deformation: Denali fault, Alaska. *Geophys. J. Int.* **2007**, *170*, 1165–1179. [[CrossRef](#)]
209. Blanco-Sanchez, P.; Mallorqui, J.J.; Duque, S.; Monells, D. The Coherent Pixels Technique (CPT): An advanced DInSAR technique for nonlinear deformation monitoring. *Pure Appl. Geophys.* **2008**, *165*, 1167–1193. [[CrossRef](#)]
210. Lauknes, T.R.; Zebker, H.A.; Larsen, Y. InSAR deformation time series using an L-1-norm small-baseline approach. *IEEE Trans. Geosci. Remote Sens.* **2011**, *49*, 536–546. [[CrossRef](#)]
211. Goel, K.; Adam, N. An advanced algorithm for deformation estimation in non-urban areas. *ISPRS-J. Photogramm. Remote Sens.* **2012**, *73*, 100–110. [[CrossRef](#)]
212. Shirzaei, M. A wavelet-based multitemporal DInSAR algorithm for monitoring ground surface motion. *IEEE Geosci. Remote Sens. Lett.* **2013**, *10*, 456–460. [[CrossRef](#)]

213. Verde, S.; Reale, D.; Pauciuillo, A.; Fornaro, G. Improved small baseline processing by means of CAESAR eigen-interferograms decomposition. *ISPRS-J. Photogramm. Remote Sens.* **2018**, *139*, 1–13. [\[CrossRef\]](#)
214. Samsonov, S.; d’Oreye, N. Multidimensional time-series analysis of ground deformation from multiple InSAR data sets applied to Virunga Volcanic Province. *Geophys. J. Int.* **2012**, *191*, 1095–1108. [\[CrossRef\]](#)
215. Pepe, A.; Solaro, G.; Calo, F.; Dema, C. A minimum acceleration approach for the retrieval of multiplatform InSAR deformation time series. *IEEE J. Sel. Top. Appl. Earth Obs. Remote Sens.* **2016**, *9*, 3883–3898. [\[CrossRef\]](#)
216. Sowter, A.; Bateson, L.; Strange, P.; Ambrose, K.; Syafiudin, M.F. DInSAR estimation of land motion using intermittent coherence with application to the South Derbyshire and Leicestershire coalfields. *Remote Sens. Lett.* **2013**, *4*, 979–987. [\[CrossRef\]](#)
217. Bateson, L.; Cigna, F.; Boon, D.; Sowter, A. The application of the Intermittent SBAS (ISBAS) InSAR method to the South Wales Coalfield, UK. *Int. J. Appl. Earth Obs. Geoinf.* **2015**, *34*, 249–257. [\[CrossRef\]](#)
218. Pepe, A.; Lanari, R. On the extension of the minimum cost flow algorithm for phase unwrapping of multitemporal differential SAR interferograms. *IEEE Trans. Geosci. Remote Sens.* **2006**, *44*, 2374–2383. [\[CrossRef\]](#)
219. Guarnieri, A.M.; Tebaldini, S. On the exploitation of target statistics for SAR interferometry applications. *IEEE Trans. Geosci. Remote Sens.* **2008**, *46*, 3436–3443. [\[CrossRef\]](#)
220. Pinel-Puysssegur, B.; Michel, R.; Avouac, J.-P. Multi-Link InSAR time series: Enhancement of a wrapped interferometric database. *IEEE J. Sel. Top. Appl. Earth Obs. Remote Sens.* **2012**, *5*, 784–794. [\[CrossRef\]](#)
221. Fornaro, G.; Verde, S.; Reale, D.; Pauciuillo, A. CAESAR: An approach based on covariance matrix decomposition to improve multibaseline-multitemporal interferometric SAR processing. *IEEE Trans. Geosci. Remote Sens.* **2015**, *53*, 2050–2065. [\[CrossRef\]](#)
222. Pepe, A.; Yang, Y.; Manzo, M.; Lanari, R. Improved EMCF-SBAS processing chain based on advanced techniques for the noise-filtering and selection of small baseline multi-look DInSAR interferograms. *IEEE Trans. Geosci. Remote Sens.* **2015**, *53*, 4394–4417. [\[CrossRef\]](#)
223. Ansari, H.; De Zan, F.; Bamler, R. Efficient phase estimation for interferogram stacks. *IEEE Trans. Geosci. Remote Sens.* **2018**, *56*, 4109–4125. [\[CrossRef\]](#)
224. Burgmann, R.; Rosen, P.A.; Fielding, E.J. Synthetic aperture radar interferometry to measure Earth’s surface topography and its deformation. *Annu. Rev. Earth Planet. Sci.* **2000**, *28*, 169–209. [\[CrossRef\]](#)
225. Pritchard, M.; Simons, M. An InSAR-based survey of volcanic deformation in the central Andes. *Geochem. Geophys. Geosyst.* **2004**, *5*, Q02002. [\[CrossRef\]](#)
226. Rott, H. Advances in interferometric synthetic aperture radar (InSAR) in earth system science. *Prog. Phys. Geogr. Earth Environ.* **2009**, *33*, 769–791. [\[CrossRef\]](#)
227. Ruch, J.; Pepe, S.; Casu, F.; Acocella, V.; Neri, M.; Solaro, G.; Sansosti, E. How do volcanic rift zones relate to flank instability? Evidence from collapsing rifts at Etna. *Geophys. Res. Lett.* **2012**, *39*, L20311. [\[CrossRef\]](#)
228. Acocella, V.; Neri, M.; Norini, G. An overview of experimental models to understand a complex volcanic instability: Application to Mount Etna, Italy. *J. Volcanol. Geotherm. Res.* **2013**, *251*, 98–111. [\[CrossRef\]](#)
229. Iglesias, R.; Aguasca, A.; Fabregas, X.; Mallorqui, J.J.; Monells, D.; Lopez-Martinez, C.; Pipia, L. Ground-Based polarimetric SAR interferometry for the monitoring of terrain displacement phenomena-part I: Theoretical description. *IEEE J. Sel. Top. Appl. Earth Observ. Remote Sens.* **2015**, *8*, 980–993. [\[CrossRef\]](#)
230. Perissin, D. Interferometric SAR Multitemporal Processing: Techniques and Applications. In *Multitemporal Remote Sensing*; Springer: Cham, Switzerland, 2016; pp. 145–176.
231. Deffontaines, B.; Chang, K.-J.; Champenois, J.; Fruneau, B.; Pathier, E.; Hu, J.-C.; Lu, S.-T.; Liu, Y.-C. Active interseismic shallow deformation of the Pingting terraces (Longitudinal Valley–Eastern Taiwan) from UAV high-resolution topographic data combined with InSAR time series. *Geomat. Nat. Hazards Risk* **2017**, *8*, 120–136. [\[CrossRef\]](#)
232. Hong, S.-H.; Wdowinski, S. A review on monitoring the everglades wetlands in the Southern Florida using space-based synthetic aperture radar (SAR) observations. *Korean J. Remote Sens.* **2017**, *33*, 377–390. [\[CrossRef\]](#)
233. Xu, X.; Sandwell, D.T.; Tymofyeyeva, E.; Gonzalez-Ortega, A.; Tong, X. Tectonic and anthropogenic deformation at the Cerro Prieto geothermal step-over revealed by Sentinel-1A InSAR. *IEEE Trans. Geosci. Remote Sens.* **2017**, *55*, 5284–5292. [\[CrossRef\]](#)
234. Gong, H.; Pan, Y.; Zheng, L.; Li, X.; Zhu, L.; Zhang, C.; Huang, Z.; Li, Z.; Wang, H.; Zhou, C. Long-term groundwater storage changes and land subsidence development in the North China Plain (1971–2015). *Hydrogeol. J.* **2018**, *26*, 1417–1427. [\[CrossRef\]](#)
235. Maghsoudi, Y.; van der Meer, F.; Hecker, C.; Perissin, D.; Saepuloh, A. Using PS-InSAR to detect surface deformation in geothermal areas of West Java in Indonesia. *Int. J. Appl. Earth Obs. Geoinf.* **2018**, *64*, 386–396. [\[CrossRef\]](#)
236. Wang, C.; Zhang, Z.; Zhang, H.; Zhang, B.; Tang, Y.; Wu, Q. Active layer thickness retrieval of Qinghai-Tibet permafrost using the TerraSAR-X InSAR technique. *IEEE J. Sel. Top. Appl. Earth Obs. Remote Sens.* **2018**, *11*, 4403–4413. [\[CrossRef\]](#)
237. Gaddes, M.E.; Hooper, A.; Bagnardi, M. Using machine learning to automatically detect volcanic unrest in a time series of interferograms. *J. Geophys. Res. Solid Earth* **2019**, *124*, 12304–12322. [\[CrossRef\]](#)
238. Wang, J.; Yu, W.; Deng, Y.; Wang, R.; Wang, Y.; Zhang, H.; Zheng, M. Demonstration of time-series InSAR processing in Beijing using a small stack of Gaofen-3 differential interferograms. *J. Sens.* **2019**, *2019*, 4204580. [\[CrossRef\]](#)
239. Albino, F.; Biggs, J.; Yu, C.; Li, Z. Automated methods for detecting volcanic deformation using Sentinel-1 InSAR time series illustrated by the 2017–2018 unrest at Agung, Indonesia. *J. Geophys. Res. Solid Earth* **2020**, *125*, e2019JB017908. [\[CrossRef\]](#)
240. Ding, J.; Zhao, Q.; Tang, M.; Calo, F.; Zamparelli, V.; Falabella, F.; Liu, M.; Pepe, A. On the characterization and forecasting of ground displacements of ocean-reclaimed lands. *Remote Sens.* **2020**, *12*, 2971. [\[CrossRef\]](#)

241. Farquharson, J.I.; Amelung, F. Extreme rainfall triggered the 2018 rift eruption at Kilauea Volcano. *Nature* **2020**, *580*, 491–495. [[CrossRef](#)] [[PubMed](#)]
242. Hoyt, A.M.; Chaussard, E.; Seppalainen, S.S.; Harvey, C.F. Widespread subsidence and carbon emissions across Southeast Asian peatlands. *Nat. Geosci.* **2020**, *13*, 435–440. [[CrossRef](#)]
243. Stephens, K.J.; Wauthier, C.; Bussard, R.C.; Higgins, M.; LaFemina, P.C. Assessment of mitigation strategies for tropospheric phase contributions to InSAR time-series datasets over two Nicaraguan Volcanoes. *Remote Sens.* **2020**, *12*, 782. [[CrossRef](#)]
244. Xu, X.; Sandwell, D.T.; Smith-Konter, B. Coseismic displacements and surface fractures from Sentinel-1 InSAR: 2019 ridgecrest earthquakes. *Seismol. Res. Lett.* **2020**, *91*, 1979–1985. [[CrossRef](#)]
245. Xue, X.; Freymueller, J.; Lu, Z. Modeling the post-eruptive deformation at Okmok based on the GPS and InSAR time series: Changes in the shallow magma storage system. *J. Geophys. Res. Solid Earth* **2020**, *125*, e2019JB017801. [[CrossRef](#)]
246. Khan, S.D.; Huang, Z.; Karacay, A. Study of ground subsidence in northwest Harris county using GPS, LiDAR, and InSAR techniques. *Nat. Hazards* **2014**, *73*, 1143–1173. [[CrossRef](#)]
247. Wang, G.; Zhou, X.; Wang, K.; Ke, X.; Zhang, Y.; Zhao, R.; Bao, Y. GOM20: A stable geodetic reference frame for subsidence, faulting, and sea-level rise studies along the coast of the Gulf of Mexico. *Remote Sens.* **2020**, *12*, 350. [[CrossRef](#)]
248. Fiaschi, S.; Wdowinski, S. Local land subsidence in Miami Beach (FL) and Norfolk (VA) and its contribution to flooding hazard in coastal communities along the US Atlantic coast. *Ocean Coast. Manag.* **2020**, *187*, 105078. [[CrossRef](#)]
249. Canova, F.; Tolomei, C.; Salvi, S.; Toscani, G.; Seno, S. Land subsidence along the Ionian coast of SE Sicily (Italy), detection and analysis via Small Baseline Subset (SBAS) multitemporal differential SAR interferometry. *Earth Surf. Process. Landf.* **2012**, *37*, 273–286. [[CrossRef](#)]
250. Aucelli, P.P.C.; Di Paola, G.; Incontri, P.; Rizzo, A.; Vilardo, G.; Benassai, G.; Buonocore, B.; Pappone, G. Coastal inundation risk assessment due to subsidence and sea level rise in a Mediterranean alluvial plain (Vulturno coastal plain—Southern Italy). *Estuar. Coast. Shelf Sci.* **2017**, *198*, 597–609. [[CrossRef](#)]
251. Da Lio, C.; Tosi, L. Land subsidence in the Friuli Venezia Giulia coastal plain, Italy: 1992–2010 results from SAR-based interferometry. *Sci. Total Environ.* **2018**, *633*, 752–764. [[CrossRef](#)]
252. Tosi, L.; Da Lio, C.; Teatini, P.; Strozzi, T. Land subsidence in coastal environments: Knowledge advance in the Venice Coastland by TerraSAR-X PSI. *Remote Sens.* **2018**, *10*, 1191. [[CrossRef](#)]
253. Syvitski, J.P.; Kettner, A.J.; Overeem, I.; Hutton, E.W.; Hannon, M.T.; Brakenridge, G.R.; Day, J.; Vörösmarty, C.; Saito, Y.; Giosan, L. Sinking deltas due to human activities. *Nat. Geosci.* **2009**, *2*, 681–686. [[CrossRef](#)]
254. Twilley, R.R.; Bentley, S.J.; Chen, Q.; Edmonds, D.A.; Hagen, S.C.; Lam, N.S.N.; Willson, C.S.; Xu, K.; Braud, D.; Peele, R.H.; et al. Co-evolution of wetland landscapes, flooding, and human settlement in the Mississippi River Delta Plain. *Sustain. Sci.* **2016**, *11*, 711–731. [[CrossRef](#)]
255. Higgins, S.; Overeem, I.; Tanaka, A.; Syvitski, J.P.M. Land subsidence at aquaculture facilities in the Yellow River delta, China. *Geophys. Res. Lett.* **2013**, *40*, 3898–3902. [[CrossRef](#)]
256. Zhang, J.-Z.; Huang, H.-j.; Bi, H.-b. Land subsidence in the modern Yellow River Delta based on InSAR time series analysis. *Nat. Hazards* **2015**, *75*, 2385–2397. [[CrossRef](#)]
257. Wang, H.; Wright, T.J.; Yu, Y.; Lin, H.; Jiang, L.; Li, C.; Qiu, G. InSAR reveals coastal subsidence in the Pearl River Delta, China. *Geophys. J. Int.* **2012**, *191*, 1119–1128. [[CrossRef](#)]
258. Brown, S.; Nicholls, R.J. Subsidence and human influences in mega deltas: The case of the Ganges-Brahmaputra-Meghna. *Sci. Total Environ.* **2015**, *527–528*, 362–374. [[CrossRef](#)]
259. Hu, J.; Shi, B.; Inyang, H.I.; Chen, J.; Sui, Z. Patterns of subsidence in the lower Yangtze Delta of China: The case of the Suzhou-Wuxi-Changzhou Region. *Environ. Monit. Assess.* **2009**, *153*, 61–72. [[CrossRef](#)] [[PubMed](#)]
260. Yu, L.; Yang, T.; Zhao, Q.; Liu, M.; Pepe, A. The 2015–2016 ground displacements of the Shanghai coastal area inferred from a combined COSMO-SkyMed/Sentinel-1 DInSAR analysis. *Remote Sens.* **2017**, *9*, 1194. [[CrossRef](#)]
261. Wang, Q.; Zhao, Q.; Ding, J.; Fedotov, A.A.; Badenko, V.; Liu, M.; Pepe, A. Investigation of the ground displacement in Saint Petersburg, Russia, using multiple-track differential synthetic aperture radar interferometry. *Int. J. Appl. Earth Obs. Geoinf.* **2020**, *87*, 102050. [[CrossRef](#)]
262. Komen, G.J.; Cavaleri, L.; Donelan, M.; Hasselmann, K.; Hasselmann, S.; Janssen, P.A.E.M. *Dynamics and Modelling of Ocean Waves*; Cambridge University Press: Cambridge, UK, 1994. [[CrossRef](#)]
263. Thompson, T.; Liu, W.; Weissman, D. Synthetic aperture radar observation of ocean roughness from rolls in an unstable marine boundary layer. *Geophys. Res. Lett.* **1983**, *10*, 1172–1175. [[CrossRef](#)]
264. Fornaro, G.; Lanari, R.; Sansosti, E.; Franceschetti, G.; Perna, S.; Gois, A.; Moreira, J. Airborne Differential Interferometry: X-Band Experiments. In Proceedings of the IGARSS 2004 IEEE International Geoscience and Remote Sensing Symposium, Anchorage, AK, USA, 20–24 September 2004; Volume 3325, pp. 3329–3332.
265. Amadori, M.; Zamparelli, V.; De Carolis, G.; Fornaro, G.; Toffolon, M.; Bresciani, M.; Giardino, C.; De Santi, F. Monitoring Lakes Surface Water Velocity with SAR: A Feasibility Study on Lake Garda, Italy. *Remote Sens.* **2021**, *13*, 2293. [[CrossRef](#)]
266. Zamparelli, V.; Perna, S.; Fornaro, G. An Improved Topography and Aperture Dependent Motion Compensation Algorithm. In Proceedings of the 2012 IEEE International Geoscience and Remote Sensing Symposium, Munich, Germany, 22–27 July 2012; pp. 5805–5808.

267. Romeiser, R.; Alpers, W. An improved composite surface model for the radar backscattering cross section of the ocean surface: 2. Model response to surface roughness variations and the radar imaging of underwater bottom topography. *J. Geophys. Res. Oceans* **1997**, *102*, 25251–25267. [[CrossRef](#)]
268. Goldstein, R.M.; Zebker, H.A.; Barnett, T.P. Remote sensing of ocean currents. *Science* **1989**, *246*, 1282–1285. [[CrossRef](#)]
269. Kudryavtsev, V.; Akimov, D.; Johannessen, J.; Chapron, B. On radar imaging of current features: 1. Model and comparison with observations. *J. Geophys. Res.-Oceans* **2005**, *110*, C07016. [[CrossRef](#)]
270. Johannessen, J.A.; Chapron, B.; Collard, F.; Kudryavtsev, V.; Mouche, A.; Akimov, D.; Dagestad, K.F. Direct ocean surface velocity measurements from space: Improved quantitative interpretation of Envisat ASAR observations. *Geophys. Res. Lett.* **2008**, *35*, L22608. [[CrossRef](#)]
271. Romeiser, R.; Runge, H.; Suchandt, S.; Kahle, R.; Rossi, C.; Bell, P.S. Quality assessment of surface current fields from TerraSAR-X and TanDEM-X along-track interferometry and doppler centroid analysis. *IEEE Trans. Geosci. Remote Sens.* **2014**, *52*, 2759–2772. [[CrossRef](#)]
272. Arduin, F.; Chapron, B.; Maes, C.; Romeiser, R.; Gommenginger, C.; Cravatte, S.; Morrow, R.; Donlon, C.; Bourassa, M. Satellite doppler observations for the motions of the oceans. *Bull. Am. Meteorol. Soc.* **2019**, *100*, ES215–ES219. [[CrossRef](#)]
273. Mouche, A.A.; Collard, F.; Chapron, B.; Dagestad, K.-F.; Guitton, G.; Johannessen, J.A.; Kerbaol, V.; Hansen, M.W. On the use of doppler shift for sea surface wind retrieval from SAR. *IEEE Trans. Geosci. Remote Sens.* **2012**, *50*, 2901–2909. [[CrossRef](#)]
274. Alpers, W.; Mouche, A.; Horstmann, J.; Ivanov, A.; Barabanov, V.; Ieee. Test of an Advanced Algorithm to Retrieve Complex Wind Fields over the Black Sea from ENVISAT SAR Images. In Proceedings of the IEEE International Geoscience and Remote Sensing Symposium (IGARSS), Melbourne, Australia, 21–26 July 2013; pp. 1262–1265.
275. Zamparelli, V.; De Santi, F.; Cucco, A.; Zecchetto, S.; De Carolis, G.; Fornaro, G. Surface currents derived from SAR doppler processing: An analysis over the Naples coastal region in South Italy. *J. Mar. Sci. Eng.* **2020**, *8*, 203. [[CrossRef](#)]
276. Pramudya, F.S.; Pan, J.; Devlin, A.T. Estimation of significant wave height of near-range traveling ocean waves using Sentinel-1 SAR images. *IEEE J. Sel. Top. Appl. Earth Obs. Remote Sens.* **2019**, *12*, 1067–1075. [[CrossRef](#)]
277. Pramudya, F.S.; Pan, J.; Devlin, A.T.; Lin, H. Enhanced Estimation of Significant Wave Height with Dual-Polarization Sentinel-1 SAR Imagery. *Remote Sens.* **2021**, *13*, 124. [[CrossRef](#)]
278. Zamparelli, V.; Jackson, C.; Cucco, A.; Fornaro, G.; Zecchetto, S. SAR based sea current estimation in the Naples coastal area. In Proceedings of the 36th IEEE International Geoscience and Remote Sensing Symposium (IGARSS), Beijing, China, 10–15 July 2016; pp. 4665–4668.
279. Biondi, F.; Addabbo, P.; Clemente, C.; Orlando, D. Measurements of surface river doppler velocities with along-track InSAR using a single antenna. *IEEE J. Sel. Top. Appl. Earth Obs. Remote Sens.* **2020**, *13*, 987–997. [[CrossRef](#)]
280. Goldstein, R.M.; Zebker, H.A. Interferometric radar measurement of ocean surface currents. *Nature* **1987**, *328*, 707–709. [[CrossRef](#)]
281. Natale, A.; Jackson, G.; Esposito, C.; Fornaro, G.; Lanari, R.; Perna, S. Sea state observation through a three-antenna hybrid XT/AT InSAR configuration: A preliminary study based on the InSAeS4 airborne system. *Remote Sens.* **2017**, *9*, 792. [[CrossRef](#)]
282. Yurovsky, Y.Y.; Kudryavtsev, V.N.; Grodsky, S.A.; Chapron, B. Sea surface Ka-band doppler measurements: Analysis and model development. *Remote Sens.* **2019**, *11*, 839. [[CrossRef](#)]
283. Cianelli, D.; Uttieri, M.; Buonocore, B.; Falco, P.; Zambardino, G.; Zambianchi, E. Dynamics of a very special Mediterranean coastal area: The Gulf of Naples. *Mediterr. Ecosyst. Dyn. Manag. Conserv.* **2012**, *7*, 129–150.
284. Jackson, G.; Fornaro, G.; Berardino, P.; Esposito, C.; Lanari, R.; Pauciuillo, A.; Reale, D.; Zamparelli, V.; Perna, S. Experiments of Sea Surface Currents Estimation with Space and Airborne SAR Systems. In Proceedings of the 2015 IEEE International Geoscience and Remote Sensing Symposium (IGARSS), Milan, Italy, 26–31 July 2015; pp. 373–376.
285. Son, V.N.; George, A.L. Satellite SAR Remote Sensing of Great Lakes Ice Cover, Part 1. Ice Backscatter Signatures at C Band. *J. Great Lakes Res.* **2007**, *33*, 722–735. [[CrossRef](#)]
286. Wu, L.; Wang, L.; Min, L.; Hou, W.; Guo, Z.; Zhao, J.; Li, N. Discrimination of Algal-Bloom Using Spaceborne SAR Observations of Great Lakes in China. *Remote Sens.* **2018**, *10*, 767. [[CrossRef](#)]
287. De Santi, F.; Luciani, G.; Bresciani, M.; Giardino, C.; Lovergine, F.P.; Pasquariello, G.; Vaiciute, D.; De Carolis, G. Synergistic Use of Synthetic Aperture Radar and Optical Imagery to Monitor Surface Accumulation of Cyanobacteria in the Curonian Lagoon. *J. Mar. Sci. Eng.* **2019**, *7*, 461. [[CrossRef](#)]
288. McKinney, P.; Holt, B.; Matsumoto, K. Small eddies observed in Lake Superior using SAR and sea surface temperature imagery. *J. Great Lakes Res.* **2012**, *38*, 786–797. [[CrossRef](#)]
289. Katona, T.; Bartsch, A. Estimation of wind speed over lakes in Central Europe using spaceborne C-band SAR. *Eur. J. Remote Sens.* **2018**, *51*, 921–931. [[CrossRef](#)]
290. Perna, S.; Esposito, C.; Amaral, T.; Berardino, P.; Jackson, G.; Moreira, J.; Pauciuillo, A.; Vaz Junior, E.; Wimmer, C.; Lanari, R. The InSAeS4 airborne X-band interferometric SAR system: A first assessment on its imaging and topographic mapping capabilities. *Remote Sens.* **2016**, *8*, 40. [[CrossRef](#)]
291. Perna, S.; Berardino, P.; Britti, F.; Cirillo, C.; Esposito, C.; Fornaro, G.; Lubeck, D.; Monaldi, G.; Moreira, J.; Pauciuillo, A.; et al. Capabilities of the Telaer Airborne SAR System Upgraded to the Multi-Antenna Mode. In Proceedings of the IEEE International Geoscience and Remote Sensing Symposium (IGARSS), Munich, Germany, 22–27 July 2012; pp. 1545–1548.
292. Williams, A.; Rangel-Buitrago, N.; Pranzini, E.; Anfuso, G. The management of coastal erosion. *Ocean Coast. Manag.* **2018**, *156*, 4–20. [[CrossRef](#)]

293. Besset, M.; Gratiot, N.; Anthony, E.J.; Bouchette, F.; Goichot, M.; Marchesiello, P. Mangroves and shoreline erosion in the Mekong River delta, Viet Nam. *Estuar. Coast. Shelf Sci.* **2019**, *226*, 106263. [[CrossRef](#)]
294. Ogorodov, S.; Aleksyutina, D.; Baranskaya, A.; Shabanova, N.; Shilova, O. Coastal erosion of the Russian Arctic: An overview. *J. Coast. Res.* **2020**, *95*, 599–604. [[CrossRef](#)]
295. Jasechko, S.; Perrone, D.; Seybold, H.; Fan, Y.; Kirchner, J.W. Groundwater level observations in 250,000 coastal US wells reveal scope of potential seawater intrusion. *Nat. Commun.* **2020**, *11*, 3229. [[CrossRef](#)]
296. Hinkel, J.; Lincke, D.; Vafeidis, A.T.; Perrette, M.; Nicholls, R.J.; Tol, R.S.J.; Marzeion, B.; Fettweis, X.; Ionescu, C.; Levermann, A. Coastal flood damage and adaptation costs under 21st century sea-level rise. *Proc. Natl. Acad. Sci. USA* **2014**, *111*, 3292–3297. [[CrossRef](#)] [[PubMed](#)]
297. Kulp, S.A.; Strauss, B.H. New elevation data triple estimates of global vulnerability to sea-level rise and coastal flooding. *Nat. Commun.* **2019**, *10*, 4844. [[CrossRef](#)] [[PubMed](#)]
298. Hanson, S.; Nicholls, R.; Ranger, N.; Hallegatte, S.; Corfee-Morlot, J.; Herweijer, C.; Chateau, J. A global ranking of port cities with high exposure to climate extremes. *Clim. Chang.* **2011**, *104*, 89–111. [[CrossRef](#)]
299. Muis, S.; Verlaan, M.; Winsemius, H.C.; Aerts, J.C.J.H.; Ward, P.J. A global reanalysis of storm surges and extreme sea levels. *Nat. Commun.* **2016**, *7*, 11969. [[CrossRef](#)]
300. Hallegatte, S.; Green, C.; Nicholls, R.J.; Corfee-Morlot, J. Future flood losses in major coastal cities. *Nat. Clim. Chang.* **2013**, *3*, 802–806. [[CrossRef](#)]
301. Shirzaei, M.; Burgmann, R. Global climate change and local land subsidence exacerbate inundation risk to the San Francisco Bay Area. *Sci. Adv.* **2018**, *4*, eaap9234. [[CrossRef](#)]
302. Nico, G.; Pappalepore, M.; Pasquariello, G.; Refice, A.; Samarelli, S. Comparison of SAR amplitude vs. coherence flood detection methods—a GIS application. *Int. J. Remote Sens.* **2000**, *21*, 1619–1631. [[CrossRef](#)]
303. Horritt, M.S.; Mason, D.C.; Luckman, A.J. Flood boundary delineation from Synthetic Aperture Radar imagery using a statistical active contour model. *Int. J. Remote Sens.* **2001**, *22*, 2489–2507. [[CrossRef](#)]
304. Bates, P.D.; Horritt, M.; Cobby, D.; Mason, D. *Flood Inundation Modelling Using LiDAR and SAR Data*; John Wiley & Sons: Hoboken, NJ, USA, 2004; pp. 79–106.
305. Pierdicca, N.; Chini, M.; Pulvirenti, L.; Macina, F. Integrating physical and topographic information into a fuzzy scheme to map flooded area by SAR. *Sensors* **2008**, *8*, 4151–4164. [[CrossRef](#)]
306. Martinis, S.; Twele, A.; Voigt, S. Towards operational near real-time flood detection using a split-based automatic thresholding procedure on high resolution TerraSAR-X data. *Nat. Hazards Earth Syst. Sci.* **2009**, *9*, 303–314. [[CrossRef](#)]
307. Van Der Knijff, J.M.; Younis, J.; De Roo, A.P.J. Lisflood: A GIS-based distributed model for river basin scale water balance and flood simulation. *Int. J. Geogr. Inf. Sci.* **2010**, *24*, 189–212. [[CrossRef](#)]
308. Wang, J.; Gao, W.; Xu, S.; Yu, L. Evaluation of the combined risk of sea level rise, land subsidence, and storm surges on the coastal areas of Shanghai, China. *Clim. Chang.* **2012**, *115*, 537–558. [[CrossRef](#)]
309. Zuo, J.; Yang, Y.; Zhang, J.; Chen, M.; Xu, Q. Prediction of china’s submerged coastal areas by sea level rise due to climate change. *J. Ocean Univ. China* **2013**, *12*, 327–334. [[CrossRef](#)]
310. Sampson, C.C.; Smith, A.M.; Bates, P.D.; Neal, J.C.; Alfieri, L.; Freer, J.E. A high-resolution global flood hazard model. *Water Resour. Res.* **2015**, *51*, 7358–7381. [[CrossRef](#)]
311. Yu, D.; Coulthard, T.J. Evaluating the importance of catchment hydrological parameters for urban surface water flood modelling using a simple hydro-inundation model. *J. Hydrol.* **2015**, *524*, 385–400. [[CrossRef](#)]
312. Teng, J.; Jakeman, A.J.; Vaze, J.; Croke, B.F.W.; Dutta, D.; Kim, S. Flood inundation modelling: A review of methods, recent advances and uncertainty analysis. *Environ. Model. Softw.* **2017**, *90*, 201–216. [[CrossRef](#)]
313. Wing, O.E.J.; Bates, P.D.; Sampson, C.C.; Smith, A.M.; Johnson, K.A.; Erickson, T.A. Validation of a 30 m resolution flood hazard model of the conterminous United States. *Water Resour. Res.* **2017**, *53*, 7968–7986. [[CrossRef](#)]
314. Yin, J.; Zhao, Q.; Yu, D.; Lin, N.; Kubanek, J.; Ma, G.; Liu, M.; Pepe, A. Long-term flood-hazard modeling for coastal areas using InSAR measurements and a hydrodynamic model: The case study of Lingang New City, Shanghai. *J. Hydrol.* **2019**, *571*, 593–604. [[CrossRef](#)]
315. Hsu, K.; Ombadi, M.; Nguyen, P.; Tran, H.; Sorooshian, S.; Andreadis, K. Improving Hydrologic Modeling Using Cloud-Free MODIS Flood Maps. *J. Hydrometeorol.* **2019**, *20*, 2203–2214. [[CrossRef](#)]
316. Tang, M.; Zhao, Q.; Pepe, A.; Devlin, A.T.; Falabella, F.; Yao, C.; Li, Z. Changes of Chinese Coastal Regions Induced by Land Reclamation as Revealed through TanDEM-X DEM and InSAR Analyses. *Remote Sens.* **2022**, *14*, 637. [[CrossRef](#)]
317. Patro, S.; Chatterjee, C.; Singh, R.; Raghuvanshi, N.S. Hydrodynamic modelling of a large flood-prone river system in India with limited data. *Hydrol. Process.* **2009**, *23*, 2774–2791. [[CrossRef](#)]
318. Schumann, G.; Bates, P.D.; Horritt, M.S.; Matgen, P.; Pappenberger, F. Progress in integration of remote sensing-derived flood extent and stage data and hydraulic models. *Rev. Geophys.* **2009**, *47*, RG4001. [[CrossRef](#)]
319. Neal, J.; Schumann, G.; Bates, P. A subgrid channel model for simulating river hydraulics and floodplain inundation over large and data sparse areas. *Water Resour. Res.* **2012**, *48*, W11506. [[CrossRef](#)]
320. Yu, D.; Yin, J.; Wilby, R.L.; Lane, S.N.; Aerts, J.C.J.H.; Lin, N.; Liu, M.; Yuan, H.; Chen, J.; Prudhomme, C.; et al. Disruption of emergency response to vulnerable populations during floods. *Nat. Sustain.* **2020**, *3*, 728–736. [[CrossRef](#)]

321. Kuenzer, C.; Guo, H.; Huth, J.; Leinenkugel, P.; Li, X.; Dech, S. Flood mapping and flood dynamics of the Mekong Delta: ENVISAT-ASAR-WSM based time series analyses. *Remote Sens.* **2013**, *5*, 687–715. [CrossRef]
322. Chan, F.K.S.; Adekola, O.A.; Cho Nam, N.; Mitchell, G.; McDonald, A.T. Coastal flood-risk management practice in Tai O, a town in Hong Kong. *Environ. Pract.* **2013**, *15*, 201–219. [CrossRef]
323. Amadio, M.; Mysiak, J.; Carrera, L.; Koks, E. Improving flood damage assessment models in Italy. *Nat. Hazards* **2016**, *82*, 2075–2088. [CrossRef]
324. Kreibich, H.; Piroth, K.; Seifert, I.; Maiwald, H.; Kunert, U.; Schwarz, J.; Merz, B.; Thieken, A.H. Is flow velocity a significant parameter in flood damage modelling? *Nat. Hazards Earth Syst. Sci.* **2009**, *9*, 1679–1692. [CrossRef]
325. Luino, F.; Cirio, C.G.; Biddoccu, M.; Agangi, A.; Giulietto, W.; Godone, F.; Nigrelli, G. Application of a model to the evaluation of flood damage. *Geoinformatica* **2009**, *13*, 339–353. [CrossRef]
326. Merz, B.; Hall, J.; Disse, M.; Schumann, A. Fluvial flood risk management in a changing world. *Nat. Hazards Earth Syst. Sci.* **2010**, *10*, 509–527. [CrossRef]
327. Arrighi, C.; Brugioni, M.; Castelli, F.; Franceschini, S.; Mazzanti, B. Urban micro-scale flood risk estimation with parsimonious hydraulic modelling and census data. *Nat. Hazards Earth Syst. Sci.* **2013**, *13*, 1375–1391. [CrossRef]
328. Brakenridge, G.; Anderson, E.; Nghiem, S. Satellite Microwave Detection and Measurement of River Floods. In Proceedings of the AGU Spring Meeting Abstracts, Baltimore, MD, USA, 1 May 2006; p. H23A-05.
329. Gianinetto, M.; Villa, P.; Lechi, G. Postflood damage evaluation using landsat TM and ETM plus data integrated with DEM. *IEEE Trans. Geosci. Remote Sens.* **2006**, *44*, 236–243. [CrossRef]
330. Nigro, J.; Slayback, D.; Policelli, F.; Brakenridge, G.R. NASA/DFO MODIS Near Real-Time (NRT) Global Flood Mapping Product Evaluation of Flood and Permanent Water Detection. 2014. Available online: https://floodmap.modaps.eosdis.nasa.gov/documents/NASAGlobalNRTEvaluationSummary_v4.pdf (accessed on 1 March 2021).
331. Yan, K.; Di Baldassarre, G.; Solomatine, D.P.; Schumann, G.J.P. A review of low-cost space-borne data for flood modelling: Topography, flood extent and water level. *Hydrol. Process.* **2015**, *29*, 3368–3387. [CrossRef]
332. Rahman, M.S.; Di, L. The state of the art of spaceborne remote sensing in flood management. *Nat. Hazards* **2017**, *85*, 1223–1248. [CrossRef]
333. Brivio, P.A.; Colombo, R.; Maggi, M.; Tomasoni, R. Integration of remote sensing data and GIS for accurate mapping of flooded areas. *Int. J. Remote Sens.* **2002**, *23*, 429–441. [CrossRef]
334. Pulvirenti, L.; Pierdicca, N.; Chini, M.; Guerriero, L. An algorithm for operational flood mapping from Synthetic Aperture Radar (SAR) data using fuzzy logic. *Nat. Hazards Earth Syst. Sci.* **2011**, *11*, 529–540. [CrossRef]
335. Mason, D.C.; Giustarini, L.; Garcia-Pintado, J.; Cloke, H.L. Detection of flooded urban areas in high resolution Synthetic Aperture Radar images using double scattering. *Int. J. Appl. Earth Obs. Geoinf.* **2014**, *28*, 150–159. [CrossRef]
336. Refice, A.; Capolongo, D.; Pasquariello, G.; D’Addabbo, A.; Bovenga, F.; Nutricato, R.; Lovergine, F.P.; Pietranera, L. SAR and InSAR for flood monitoring: Examples with COSMO-SkyMed data. *IEEE J. Sel. Top. Appl. Earth Obs. Remote Sens.* **2014**, *7*, 2711–2722. [CrossRef]
337. Schumann, G.J.P.; Moller, D.K. Microwave remote sensing of flood inundation. *Phys. Chem. Earth* **2015**, *83–84*, 84–95. [CrossRef]
338. Boni, G.; Ferraris, L.; Pulvirenti, L.; Squicciarino, G.; Pierdicca, N.; Candela, L.; Pisani, A.R.; Zoffoli, S.; Onori, R.; Proietti, C.; et al. A prototype system for flood monitoring based on flood forecast combined with COSMO-SkyMed and Sentinel-1 data. *IEEE J. Sel. Top. Appl. Earth Obs. Remote Sens.* **2016**, *9*, 2794–2805. [CrossRef]
339. Clement, M.A.; Kilsby, C.G.; Moore, P. Multi-temporal synthetic aperture radar flood mapping using change detection. *J. Flood Risk Manag.* **2018**, *11*, 152–168. [CrossRef]
340. Hapuarachchi, H.A.P.; Wang, Q.J.; Pagano, T.C. A review of advances in flash flood forecasting. *Hydrol. Process.* **2011**, *25*, 2771–2784. [CrossRef]
341. Borga, M.; Stoffel, M.; Marchi, L.; Marra, F.; Jakob, M. Hydrogeomorphic response to extreme rainfall in headwater systems: Flash floods and debris flows. *J. Hydrol.* **2014**, *518*, 194–205. [CrossRef]
342. Li, W.; Zhao, M.; Scaioni, M.; Hosseini, S.R.; Wang, X.; Yao, D.; Zhang, K.; Gao, J.; Li, X. Extreme rainfall trends of 21 typical urban areas in China during 1998–2015 based on remotely sensed data sets. *Environ. Monit. Assess.* **2019**, *191*, 709. [CrossRef] [PubMed]
343. Thomas, W.; Baier, F.; Erbertseder, T.; Kaästner, M. Analysis of the Algerian severe weather event in November 2001 and its impact on ozone and nitrogen dioxide distributions. *Tellus B Chem. Phys. Meteorol.* **2011**, *55*, 993–1006. [CrossRef]
344. Elkhachy, I. Flash flood hazard mapping using satellite images and GIS tools: A case study of Najran City, Kingdom of Saudi Arabia (KSA). *Egypt. J. Remote Sens. Space Sci.* **2015**, *18*, 261–278. [CrossRef]
345. Wright, D.B.; Mantilla, R.; Peters-Lidard, C.D. A remote sensing-based tool for assessing rainfall-driven hazards. *Environ. Model. Softw.* **2017**, *90*, 34–54. [CrossRef]
346. Ricciardelli, E.; Di Paola, F.; Gentile, S.; Cersosimo, A.; Cimini, D.; Gallucci, D.; Gerdali, E.; Larosa, S.; Nilo, S.T.; Ripepi, E.; et al. Analysis of Livorno heavy rainfall event: Examples of satellite-based observation techniques in support of numerical weather prediction. *Remote Sens.* **2018**, *10*, 1549. [CrossRef]
347. Krajewski, W.; Smith, J.A. Radar hydrology: Rainfall estimation. *Adv. Water Resour.* **2002**, *25*, 1387–1394. [CrossRef]
348. Peleg, N.; Marra, F.; Fatichi, S.; Paschalis, A.; Molnar, P.; Burlando, P. Spatial variability of extreme rainfall at radar subpixel scale. *J. Hydrol.* **2018**, *556*, 922–933. [CrossRef]
349. Williams, S.J. Sea-level rise implications for coastal regions. *J. Coast. Res.* **2013**, *63*, 184–196. [CrossRef]

350. Devlin, A.T.; Pan, J.; Lin, H. Extended water level trends at long-record tide gauges via moving window averaging and implications for future coastal flooding. *J. Geophys. Res. Oceans* **2021**, *126*, e2021JC017730. [[CrossRef](#)]
351. Devlin, A.T.; Jay, D.A.; Talke, S.A.; Zaron, E.D.; Pan, J.; Lin, H. Coupling of sea level and tidal range changes, with implications for future water levels. *Sci. Rep.* **2017**, *7*, 17021. [[CrossRef](#)] [[PubMed](#)]
352. Devlin, A.T.; Pan, J.; Lin, H. Tidal variability in the Hong Kong region. *Ocean Sci.* **2019**, *15*, 853–864. [[CrossRef](#)]
353. Woodworth, P.L. A survey of recent changes in the main components of the ocean tide. *Cont. Shelf Res.* **2010**, *30*, 1680–1691. [[CrossRef](#)]
354. Mueller, M.; Arbic, B.K.; Mitrovica, J.X. Secular trends in ocean tides: Observations and model results. *J. Geophys. Res. Oceans* **2011**, *116*, C05013. [[CrossRef](#)]
355. Haigh, I.D.; Wijeratne, E.M.S.; MacPherson, L.R.; Pattiaratchi, C.B.; Mason, M.S.; Crompton, R.P.; George, S. Estimating present day extreme water level exceedance probabilities around the coastline of Australia: Tides, extra-tropical storm surges and mean sea level. *Clim. Dyn.* **2014**, *42*, 121–138. [[CrossRef](#)]
356. Ray, R.D. Secular changes of the M2 tide in the Gulf of Maine. *Cont. Shelf Res.* **2006**, *26*, 422–427. [[CrossRef](#)]
357. Ray, R.D. Secular changes in the solar semidiurnal tide of the western North Atlantic Ocean. *Geophys. Res. Lett.* **2009**, *36*, L19601. [[CrossRef](#)]
358. Feng, X.; Tsimplis, M.N. Sea level extremes at the coasts of China. *J. Geophys. Res. Oceans* **2014**, *119*, 1593–1608. [[CrossRef](#)]
359. Feng, X.; Tsimplis, M.N.; Woodworth, P.L. Nodal variations and long-term changes in the main tides on the coasts of China. *J. Geophys. Res. Oceans* **2015**, *120*, 1215–1232. [[CrossRef](#)]
360. Rasheed, A.S.; Chua, V.P. Secular trends in tidal parameters along the coast of Japan. *Atmosphere-Ocean* **2014**, *52*, 155–168. [[CrossRef](#)]
361. Zaron, E.D.; Jay, D.A. An analysis of secular change in tides at open-ocean sites in the Pacific. *J. Phys. Oceanogr.* **2014**, *44*, 1704–1726. [[CrossRef](#)]
362. Amin, M. On perturbations of harmonic constants in the Thames Estuary. *Geophys. J. R. Astr. Soc.* **1983**, *73*, 587–603. [[CrossRef](#)]
363. Chernetsky, A.S.; Schuttelaars, H.M.; Talke, S.A. The effect of tidal asymmetry and temporal settling lag on sediment trapping in tidal estuaries. *Ocean Dyn.* **2010**, *60*, 1219–1241. [[CrossRef](#)]
364. Jay, D.A.; Leffler, K.; Degens, S. Long-Term evolution of columbia river tides. *J. Waterw. Port Coast. Ocean. Eng.* **2011**, *137*, 182–191. [[CrossRef](#)]
365. Vellinga, N.E.; Hoitink, A.J.F.; van der Vegt, M.; Zhang, W.; Hoekstra, P. Human impacts on tides overwhelm the effect of sea level rise on extreme water levels in the Rhine-Meuse delta. *Coast. Eng.* **2014**, *90*, 40–50. [[CrossRef](#)]
366. Familkhalili, R.; Talke, S.A. The effect of channel deepening on tides and storm surge: A case study of Wilmington, NC. *Geophys. Res. Lett.* **2016**, *43*, 9138–9147. [[CrossRef](#)]
367. Arbic, B.K.; Karsten, R.H.; Garrett, C. On Tidal Resonance in the Global Ocean and the Back-Effect of Coastal Tides upon Open-Ocean Tides. *Atmosphere-Ocean* **2009**, *47*, 239–266. [[CrossRef](#)]
368. Skiba, A.W.; Zeng, L.; Arbic, B.K.; Mueller, M.; Godwin, W.J. On the resonance and shelf/open-ocean coupling of the global diurnal tides. *J. Phys. Oceanogr.* **2013**, *43*, 1301–1324. [[CrossRef](#)]
369. Colosi, J.A.; Munk, W. Tales of the venerable Honolulu tide gauge. *J. Phys. Oceanogr.* **2006**, *36*, 967–996. [[CrossRef](#)]
370. Devlin, A.T.; Jay, D.A.; Talke, S.A.; Zaron, E. Can tidal perturbations associated with sea level variations in the western Pacific Ocean be used to understand future effects of tidal evolution? *Ocean Dyn.* **2014**, *64*, 1093–1120. [[CrossRef](#)]
371. Devlin, A.T.; Pan, J.; Lin, H. Extended spectral analysis of tidal variability in the North Atlantic Ocean. *J. Geophys. Res. Oceans* **2019**, *124*, 506–526. [[CrossRef](#)]
372. Devlin, A.T.; Pan, J.; Lin, H. Multi-Timescale analysis of tidal variability in the Indian Ocean using ensemble empirical mode decomposition. *J. Geophys. Res. Oceans* **2020**, *125*, e2020JC016604. [[CrossRef](#)]
373. Guo, L.; Zhu, C.; Wu, X.; Wan, Y.; Jay, D.A.; Townend, I.; Wang, Z.B.; He, Q. Strong inland propagation of low-frequency long waves in river estuaries. *Geophys. Res. Lett.* **2020**, *47*, e2020GL089112. [[CrossRef](#)]
374. Egbert, G.D.; Erofeeva, S.Y. Efficient inverse modeling of barotropic ocean tides. *J. Atmos. Ocean. Technol.* **2002**, *19*, 183–204. [[CrossRef](#)]
375. Lumbroso, D.M.; Suckall, N.R.; Nicholls, R.J.; White, K.D. Enhancing resilience to coastal flooding from severe storms in the USA: International lessons. *Nat. Hazards Earth Syst. Sci.* **2017**, *17*, 1357–1373. [[CrossRef](#)]
376. Walsh, K.J.; McBride, J.L.; Klotzbach, P.J.; Balachandran, S.; Camargo, S.J.; Holland, G.; Knutson, T.R.; Kossin, J.P.; Lee, T.c.; Sobel, A. Tropical cyclones and climate change. *Wiley Interdiscip. Rev. Clim. Chang.* **2016**, *7*, 65–89. [[CrossRef](#)]
377. Balk, D.L.; Deichmann, U.; Yetman, G.; Pozzi, F.; Hay, S.I.; Nelson, A. Determining Global Population Distribution: Methods, Applications and Data. *Adv. Parasitol.* **2006**, *62*, 119–156. [[CrossRef](#)]
378. Keim, B.D.; Muller, R.A.; Stone, G.W. Spatiotemporal patterns and return periods of tropical storm and hurricane strikes from Texas to Maine. *J. Clim.* **2007**, *20*, 3498–3509. [[CrossRef](#)]
379. Chao, Q.; Chao, J. Statistical features of tropical cyclones affecting China and its key economic zones. *Acta Meteorol. Sin.* **2012**, *26*, 758–772. [[CrossRef](#)]
380. Dokka, R.K.; Sella, G.F.; Dixon, T.H. Tectonic control of subsidence and southward displacement of southeast Louisiana with respect to stable North America. *Geophys. Res. Lett.* **2006**, *33*, L23308. [[CrossRef](#)]

381. Blum, M.D.; Roberts, H.H. The Mississippi Delta Region: Past, Present, and Future. *Annu. Rev. Earth Planet. Sci.* **2012**, *40*, 655–683. [CrossRef]
382. Blum, M.D.; Roberts, H.H. Drowning of the Mississippi Delta due to insufficient sediment supply and global sea-level rise. *Nat. Geosci.* **2009**, *2*, 488–491. [CrossRef]
383. Couvillion, B.R.; Barras, J.A.; Steyer, G.D.; Sleavin, W.; Fischer, M.; Beck, H.; Trahan, N.; Griffin, B.; Heckman, D. Land Area Change in Coastal Louisiana from 1932 to 2010: U.S. Geological Survey Scientific Investigations Map 3164, scale 1:265,000, 12 p. pamphlet. 2011. Available online: https://pubs.usgs.gov/sim/3164/downloads/SIM3164_Pamphlet.pdf (accessed on 1 December 2021).
384. Van der Wiel, K.; Kapnick, S.B.; Vecchi, G.A.; Smith, J.A.; Milly, P.C.D.; Jia, L. 100-Year lower Mississippi floods in a global climate model: Characteristics and future changes. *J. Hydrometeorol.* **2018**, *19*, 1547–1563. [CrossRef]
385. Munoz, S.E.; Dee, S.G. El Nino increases the risk of lower Mississippi River flooding. *Sci. Rep.* **2017**, *7*, 1772. [CrossRef]
386. Siverd, C.G.; Hagen, S.C.; Bilskie, M.V.; Braud, D.H.; Peele, R.H.; Foster-Martinez, M.R.; Twilley, R.R. Coastal Louisiana landscape and storm surge evolution: 1850–2110. *Clim. Chang.* **2019**, *157*, 445–468. [CrossRef]
387. Carstens, D.; Amer, R. Spatio-temporal analysis of urban changes and surface water quality. *J. Hydrol.* **2019**, *569*, 720–734. [CrossRef]
388. Carbognin, L.; Tosi, L. Interaction between climate changes, eustacy and land subsidence in the North Adriatic Region, Italy. *Mar. Ecol.-Pubbl. Stn. Zool. Napoli* **2002**, *23*, 38–50. [CrossRef]
389. Fiaschi, S.; Fabris, M.; Floris, M.; Achilli, V. Estimation of land subsidence in deltaic areas through differential SAR interferometry: The Po River Delta case study (Northeast Italy). *Int. J. Remote Sens.* **2018**, *39*, 8724–8745. [CrossRef]
390. Corbau, C.; Zambello, E.; Rodella, I.; Utizi, K.; Nardin, W.; Simeoni, U. Quantifying the impacts of the human activities on the evolution of Po delta It territory during the last 120 years. *J. Environ. Manag.* **2019**, *232*, 702–712. [CrossRef] [PubMed]
391. Marchetti, M. Environmental changes in the central Po Plain (northern Italy) due to fluvial modifications and anthropogenic activities. *Geomorphology* **2002**, *44*, 361–373. [CrossRef]
392. Erban, L.E.; Gorelick, S.M.; Zebker, H.A. Groundwater extraction, land subsidence, and sea-level rise in the Mekong Delta, Vietnam. *Environ. Res. Lett.* **2014**, *9*, 084010. [CrossRef]
393. Song, Y.; Li, D.; Hou, X. Characteristics of mainland coastline changes in Southeast Asia during the 21st century. *J. Coast. Res.* **2020**, *36*, 261–275. [CrossRef]
394. Hoang Huu, N.; Dargusch, P.; Moss, P.; Da Binh, T. A review of the drivers of 200 years of wetland degradation in the Mekong Delta of Vietnam. *Reg. Environ. Chang.* **2016**, *16*, 2303–2315. [CrossRef]
395. LEE, S.K.; Dang, T.A. Extreme rainfall trends over the Mekong Delta under the impacts of climate change. *Int. J. Clim. Change Strateg. Manag.* **2020**, *12*, 639–652. [CrossRef]
396. Leinenkugel, P.; Esch, T.; Kuenzer, C. Settlement detection and impervious surface estimation in the Mekong Delta using optical and SAR remote sensing data. *Remote Sens. Environ.* **2011**, *115*, 3007–3019. [CrossRef]
397. Chen, L.; Ren, C.; Zhang, B.; Li, L.; Wang, Z.; Song, K. Spatiotemporal dynamics of coastal wetlands and reclamation in the Yangtze Estuary during past 50 years (1960s–2015). *Chin. Geogr. Sci.* **2018**, *28*, 386–399. [CrossRef]
398. Xie, Z.; Du, Y.; Zeng, Y.; Miao, Q. Classification of yearly extreme precipitation events and associated flood risk in the Yangtze-Huaihe River Valley. *Sci. China-Earth Sci.* **2018**, *61*, 1341–1356. [CrossRef]
399. Shi, X.; Han, Z.; Fang, J.; Tan, J.; Guo, Z.; Sun, Z. Assessment and zonation of storm surge hazards in the coastal areas of China. *Nat. Hazards* **2020**, *100*, 39–48. [CrossRef]
400. Ma, P.; Wang, W.; Zhang, B.; Wang, J.; Shi, G.; Huang, G.; Chen, F.; Jiang, L.; Lin, H. Remotely sensing large- and small-scale ground subsidence: A case study of the Guangdong-Hong Kong-Macao Greater Bay Area of China. *Remote Sens. Environ.* **2019**, *232*, 111282. [CrossRef]
401. Zhang, Q.; Gu, X.; Singh, V.P.; Shi, P.; Sun, P. More frequent flooding? Changes in flood frequency in the Pearl River basin, China, since 1951 and over the past 1000 years. *Hydrol. Earth Syst. Sci.* **2018**, *22*, 2637–2653. [CrossRef]
402. Chu, Z. The dramatic changes and anthropogenic causes of erosion and deposition in the lower Yellow (Huanghe) River since 1952. *Geomorphology* **2014**, *216*, 171–179. [CrossRef]
403. Zhao, Y.M. *Forestry Development and Natural Conservation of Yellow River Delta*; China Forestry Press: Beijing, China, 1997.
404. Erwin, K.L. Wetlands and global climate change: The role of wetland restoration in a changing world. *Wetl. Ecol. Manag.* **2009**, *17*, 71–84. [CrossRef]
405. McGranahan, G.; Balk, D.; Anderson, B. The rising tide: Assessing the risks of climate change and human settlements in low elevation coastal zones. *Environ. Urban.* **2007**, *19*, 17–37. [CrossRef]
406. Yafeng, S.; Jiwen, Z.; Zhiren, X.; Zixiu, J.; Zixun, J.; Guishan, Y. Prediction and prevention of the impacts of sea level rise on the Yangtze River Delta and its adjacent areas. *Sci. China Ser. D Earth Sci.* **2000**, *43*, 412–422. [CrossRef]
407. Hoitink, A.J.F.; Jay, D.A. Tidal river dynamics: Implications for deltas. *Rev. Geophys.* **2016**, *54*, 240–272. [CrossRef]
408. Ge, Y.; Xu, W.; Gu, Z.-H.; Zhang, Y.-C.; Chen, L. Risk perception and hazard mitigation in the Yangtze River Delta region, China. *Nat. Hazards* **2011**, *56*, 633–648. [CrossRef]
409. Liu, B.; Siu, Y.L.; Mitchell, G.; Xu, W. Exceedance probability of multiple natural hazards: Risk assessment in China's Yangtze River Delta. *Nat. Hazards* **2013**, *69*, 2039–2055. [CrossRef]

410. Luan, H.L.; Ding, P.X.; Wang, Z.B.; Ge, J.Z.; Yang, S.L. Decadal morphological evolution of the Yangtze Estuary in response to river input changes and estuarine engineering projects. *Geomorphology* **2016**, *265*, 12–23. [\[CrossRef\]](#)
411. Wei, W.; Mei, X.; Dai, Z.; Tang, Z. Recent morphodynamic evolution of the largest uninhibited island in the Yangtze (Changjiang) estuary during 1998–2014: Influence of the anthropogenic interference. *Cont. Shelf Res.* **2016**, *124*, 83–94. [\[CrossRef\]](#)
412. Dong, S.; Samsonov, S.; Yin, H.; Ye, S.; Cao, Y. Time-series analysis of subsidence associated with rapid urbanization in Shanghai, China measured with SBAS InSAR method. *Environ. Earth Sci.* **2014**, *72*, 677–691. [\[CrossRef\]](#)
413. Shen, S. Geological environmental character of Lin-Gang new city and its influences to the construction (In Chinese with English abstract). *Shanghai Geol.* **2008**, *105*, 24–28.
414. Dong, S.; Samsonov, S.; Yin, H.; Huang, L. Two-Dimensional ground deformation monitoring in Shanghai based on SBAS and MSBAS InSAR methods. *J. Earth Sci.* **2018**, *29*, 960–968. [\[CrossRef\]](#)
415. Pepe, A.; Bonano, M.; Zhao, Q.; Yang, T.; Wang, H. The Use of C-/X-Band Time-Gapped SAR Data and Geotechnical Models for the Study of Shanghai's Ocean-Reclaimed Lands through the SBAS-DInSAR Technique. *Remote Sens.* **2016**, *8*, 911. [\[CrossRef\]](#)
416. Yang, M.; Yang, T.; Zhang, L.; Lin, J.; Qin, X.; Liao, M. Spatio-Temporal characterization of a reclamation settlement in the Shanghai coastal area with time series analyses of X-, C-, and L-Band SAR datasets. *Remote Sens.* **2018**, *10*, 329. [\[CrossRef\]](#)
417. Yu, Q.; Wang, Q.; Yan, X.; Yang, T.; Song, S.; Yao, M.; Zhou, K.; Huang, X. Ground deformation of the Chongming East Shoal Reclamation Area in Shanghai based on SBAS-InSAR and laboratory tests. *Remote Sens.* **2020**, *12*, 1016. [\[CrossRef\]](#)
418. Wang, J.; Yi, S.; Li, M.; Wang, L.; Song, C. Effects of sea level rise, land subsidence, bathymetric change and typhoon tracks on storm flooding in the coastal areas of Shanghai. *Sci. Total Environ.* **2018**, *621*, 228–234. [\[CrossRef\]](#)
419. Yang, S.L.; Xu, K.H.; Milliman, J.D.; Yang, H.F.; Wu, C.S. Decline of Yangtze River water and sediment discharge: Impact from natural and anthropogenic changes. *Sci. Rep.* **2015**, *5*, 12581. [\[CrossRef\]](#)
420. Tian, B.; Zhang, L.; Wang, X.; Zhou, Y.; Zhang, W. Forecasting the effects of sea-level rise at Chongming Dongtan Nature Reserve in the Yangtze Delta, Shanghai, China. *Ecol. Eng.* **2010**, *36*, 1383–1388. [\[CrossRef\]](#)
421. Li, C.X.; Fan, D.D.; Deng, B.; Korotaev, V. The coasts of China and issues of sea level rise. *J. Coast. Res.* **2004**, *43*, 36–49.
422. Weng, Q. Land use change analysis in the Zhujiang Delta of China using satellite remote sensing, GIS and stochastic modelling. *J. Environ. Manag.* **2002**, *64*, 273–284. [\[CrossRef\]](#) [\[PubMed\]](#)
423. Kang, L.; Ma, L.; Liu, Y. Evaluation of farmland losses from sea level rise and storm surges in the Pearl River Delta region under global climate change. *J. Geogr. Sci.* **2016**, *26*, 439–456. [\[CrossRef\]](#)
424. Yang, L.; Scheffran, J.; Qin, H.; You, Q. Climate-related flood risks and urban responses in the Pearl River Delta, China. *Reg. Environ. Chang.* **2015**, *15*, 379–391. [\[CrossRef\]](#)
425. Wang, X.; Wang, X.; Zhai, J.; Li, X.; Huang, H.; Li, C.; Zheng, J.; Sun, H. Improvement to flooding risk assessment of storm surges by residual interpolation in the coastal areas of Guangdong Province, China. *Quat. Int.* **2017**, *453*, 1–14. [\[CrossRef\]](#)
426. Yu, Q.; Lau, A.K.H.; Tsang, K.T.; Fung, J.C.H. Human damage assessments of coastal flooding for Hong Kong and the Pearl River Delta due to climate change-related sea level rise in the twenty-first century. *Nat. Hazards* **2018**, *92*, 1011–1038. [\[CrossRef\]](#)
427. Zhang, J.; Chen, Y. Risk assessment of flood disaster induced by typhoon rainstorms in Guangdong Province, China. *Sustainability* **2019**, *11*, 2738. [\[CrossRef\]](#)
428. Wang, H.; Feng, G.; Xu, B.; Yu, Y.; Li, Z.; Du, Y.; Zhu, J. Deriving spatio-temporal development of ground subsidence due to subway construction and operation in delta regions with PS-InSAR data: A case study in Guangzhou, China. *Remote Sens.* **2017**, *9*, 1004. [\[CrossRef\]](#)
429. Zhao, Q.; Lin, H.; Jiang, L.; Chen, F.; Cheng, S. A study of ground deformation in the Guangzhou urban area with persistent scatterer interferometry. *Sensors* **2009**, *9*, 503–518. [\[CrossRef\]](#)
430. Jiang, L.; Lin, H.; Cheng, S. Monitoring and assessing reclamation settlement in coastal areas with advanced InSAR techniques: Macao city (China) case study. *Int. J. Remote Sens.* **2011**, *32*, 3565–3588. [\[CrossRef\]](#)
431. Zhao, Q.; Lin, H.; Gao, W.; Zebker, H.A.; Chen, A.; Yeung, K. InSAR detection of residual settlement of an ocean reclamation engineering project: A case study of Hong Kong International Airport. *J. Oceanogr.* **2011**, *67*, 415–426. [\[CrossRef\]](#)
432. Xia, J.; Yan, Z.; Zhou, W.; Fong, S.K.; Leong, K.C.; Tang, I.M.; Chang, S.W.; Leong, W.K.; Jin, S. Projection of the Zhujiang (Pearl) River Delta's potential submerged area due to sea level rise during the 21st century based on CMIP5 simulations. *Acta Oceanol. Sin.* **2015**, *34*, 78–84. [\[CrossRef\]](#)
433. Huang, Z.G.; Zong, Y.Q.; Zhang, W.Q. Coastal inundation due to sea level rise in the Pearl River Delta, China. *Nat. Hazards* **2004**, *33*, 247–264. [\[CrossRef\]](#)
434. Zhang, W.; Yan, Y.; Zheng, J.; Li, L.; Dong, X.; Cai, H. Temporal and spatial variability of annual extreme water level in the Pearl River Delta region, China. *Glob. Planet. Chang.* **2009**, *69*, 35–47. [\[CrossRef\]](#)
435. Kong, D.; Miao, C.; Borthwick, A.G.L.; Duan, Q.; Liu, H.; Sun, Q.; Ye, A.; Di, Z.; Gong, W. Evolution of the Yellow River Delta and its relationship with runoff and sediment load from 1983 to 2011. *J. Hydrol.* **2015**, *520*, 157–167. [\[CrossRef\]](#)
436. Nguyen, T.T.X.; Woodroffe, C.D. Assessing relative vulnerability to sea-level rise in the western part of the Mekong River Delta in Vietnam. *Sustain. Sci.* **2016**, *11*, 645–659. [\[CrossRef\]](#)
437. Arias, M.E.; Cochrane, T.A.; Kummu, M.; Lauri, H.; Holtgrieve, G.W.; Koponen, J.; Piman, T. Impacts of hydropower and climate change on drivers of ecological productivity of Southeast Asia's most important wetland. *Ecol. Model.* **2014**, *272*, 252–263. [\[CrossRef\]](#)

438. Chea, R.; Grenouillet, G.; Lek, S. Evidence of water quality degradation in lower Mekong Basin revealed by self-organizing map. *PLoS ONE* **2016**, *11*, e0145527. [[CrossRef](#)]
439. Dang, T.D.; Cochrane, T.A.; Arias, M.E.; Van, P.D.T.; de Vries, T.T. Hydrological alterations from water infrastructure development in the Mekong floodplains. *Hydrol. Process.* **2016**, *30*, 3824–3838. [[CrossRef](#)]
440. Dang, T.D.; Cochrane, T.A.; Arias, M.E. Quantifying suspended sediment dynamics in mega deltas using remote sensing data: A case study of the Mekong floodplains. *Int. J. Appl. Earth Obs. Geoinf.* **2018**, *68*, 105–115. [[CrossRef](#)]
441. Bhuiyan, M.J.A.N.; Dutta, D. Assessing impacts of sea level rise on river salinity in the Gorai river network, Bangladesh. *Estuar. Coast. Shelf Sci.* **2012**, *96*, 219–227. [[CrossRef](#)]
442. Carbognin, L.; Teatini, P.; Tosi, L.; Strozzi, T.; Tomasin, A. Present Relative Sea Level Rise in the Northern Adriatic Coastal Area. In *Coastal and Marine Spatial Planning*; Brugnoli, E., Cavarretta, G., Mazzola, S., Trincardi, F., Ravaioli, M., Santoleri, R., Eds.; CNR—Dipartimento Scienze del Sistema Terra e Tecnologie: Roma, Italy, 2011; pp. 1147–1162.
443. Tosi, L.; Da Lio, C.; Strozzi, T.; Teatini, P. Combining L- and X-Band SAR Interferometry to Assess Ground Displacements in Heterogeneous Coastal Environments: The Po River Delta and Venice Lagoon, Italy. *Remote Sens.* **2016**, *8*, 308. [[CrossRef](#)]
444. Antonioli, F.; Anzidei, M.; Amorosi, A.; Lo Presti, V.; Mastronuzzi, G.; Deiana, G.; De Falco, G.; Fontana, A.; Fontolan, G.; Lisco, S.; et al. Sea-level rise and potential drowning of the Italian coastal plains: Flooding risk scenarios for 2100. *Quat. Sci. Rev.* **2017**, *158*, 29–43. [[CrossRef](#)]
445. Bondesanf, M.; Castiglioni, G.; Elmis, C.; Gabbianellis, G.; Marocco, R.; Pirazzolift, P.; Tomasin, A. Coastal areas at risk from storm surges and sea-level rise in northeastern Italy. *J. Coast. Res.* **1995**, *11*, 1354–1379.
446. Zanchettin, D.; Traverso, P.; Tomasino, M. Observations on future sea level changes in the Venice lagoon. *Hydrobiologia* **2007**, *577*, 41–53. [[CrossRef](#)]
447. Da Lio, C.; Tosi, L. Vulnerability to relative sea-level rise in the Po river delta (Italy). *Estuar. Coast. Shelf Sci.* **2019**, *228*, 106379. [[CrossRef](#)]
448. Cavaleri, L.; Bajo, M.; Barbariol, F.; Bastianini, M.; Benetazzo, A.; Bertotti, L.; Chiggiato, J.; Ferrarin, C.; Trincardi, F.; Umgiesser, G.; et al. The 2019 flooding of Venice and its implications for future predictions. *Oceanography* **2020**, *33*, 42–49. [[CrossRef](#)]
449. Niroumand-Jadidi, M.; Bovolo, F.; Bruzzone, L.; Gege, P. Physics-based Bathymetry and water quality retrieval using planetscope imagery: Impacts of 2020 COVID-19 lockdown and 2019 extreme flood in the Venice Lagoon. *Remote Sens.* **2020**, *12*, 2381. [[CrossRef](#)]
450. Popov, S.K.; Lobov, A.L. Hydrodynamic modeling of floods in Saint Petersburg considering the operating dam. *Russ. Meteorol. Hydrol.* **2017**, *42*, 267–274. [[CrossRef](#)]
451. Karatygin, P. *Chronicle of Petersburg Floods 1703–1879*; Publishing House of Suvorin: St. Petersburg, Russia, 1888.
452. Lavrov, L.; Sementsov, S. Flood risk in Saint Petersburg, Russia: History and modern times. *Proc. Inst. Civ. Eng.-Civ. Eng.* **2015**, *168*, 3–16. [[CrossRef](#)]
453. Shirshova, V. The experience of monitoring the land subsidence in urban areas by radar satellite interferometry on the example of St. Petersburg. *Geod. Aerophotosurveying* **2020**, *64*, 399–408. [[CrossRef](#)]
454. Frihy, O.E. Some proposals for coastal management of the Nile delta coast. *Ocean Coast. Manag.* **1996**, *30*, 43–59. [[CrossRef](#)]
455. Frihy, O.E.; Dewidar, K.M.; Nasr, S.M.; El Raey, M.M. Change detection of the northeastern Nile delta of Egypt: Shoreline changes, Spit evolution, margin changes of Manzala lagoon and its islands. *Int. J. Remote Sens.* **1998**, *19*, 1901–1912. [[CrossRef](#)]
456. Saleh, M.; Becker, M. New estimation of Nile Delta subsidence rates from InSAR and GPS analysis. *Environ. Earth Sci.* **2018**, *78*, 6. [[CrossRef](#)]
457. Aly, M.H.; Giardino, J.R.; Klein, A.G.; Zebker, H.A. InSAR study of shoreline change along the Damietta Promontory, Egypt. *J. Coast. Res.* **2012**, *28*, 1263–1269. [[CrossRef](#)]
458. Milliman, J.D.; Meade, R.H. World-wide delivery of river sediment to the oceans. *J. Geol.* **1983**, *91*, 1–21. [[CrossRef](#)]
459. Jervey, M. *Quantitative Geological Modeling of Siliciclastic Rock Sequences and Their Seismic Expression*; GeoScienceWorld: McLean, VA, USA, 1988. [[CrossRef](#)]
460. Gagliano, S.M.; Meyer-Arendt, K.J.; Wicker, K.M. Land loss in the Mississippi River deltaic plain. *GCAGS Trans.* **1981**, *31*, 295–300.
461. Britsch, L.D.; Dunbar, J.B. Land Loss Rates: Louisiana Coastal Plain. *J. Coast. Res.* **1993**, *9*, 324–338.
462. Barras, J.A.; Bernier, J.C.; Morton, R.A. *Land Area Change in Coastal Louisiana, a Multidecadal Perspective (from 1956 to 2006)*; U.S. Geological Survey Scientific Investigations Map 3019, scale 1:250,000, 14 p. pamphlet; U.S. Geological Survey: Reston, VA, USA, 2008.
463. Morton, R.A.; Bernier, J.C.; Kelso, K.W.; Barras, J.A. Quantifying large-scale historical formation of accommodation in the Mississippi Delta. *Earth Surf. Process. Landf.* **2010**, *35*, 1625–1641. [[CrossRef](#)]
464. Walker, N.D.; Wiseman, W.J.; Rouse, L.J.; Babin, A. Effects of river discharge, wind stress, and slope eddies on circulation and the satellite-observed structure of the Mississippi River plume. *J. Coast. Res.* **2005**, *21*, 1228–1244. [[CrossRef](#)]
465. Allen, Y.C.; Couvillion, B.R.; Barras, J.A. Using multitemporal remote sensing imagery and inundation measures to improve land change estimates in coastal wetlands. *Estuaries Coasts* **2012**, *35*, 190–200. [[CrossRef](#)]
466. Jung, H.C.; Jasinski, M.; Kim, J.-W.; Shum, C.K.; Bates, P.; Neal, J.; Lee, H.; Alsdorf, D. Calibration of two-dimensional floodplain modeling in the central Atchafalaya Basin Floodway System using SAR interferometry. *Water Resour. Res.* **2012**, *48*, W07511. [[CrossRef](#)]

467. Kolker, A.S.; Li, C.; Walker, N.D.; Pilley, C.; Ameen, A.D.; Boxer, G.; Ramatchandirane, C.; Ullah, M.; Williams, K.A. The impacts of the great Mississippi/Atchafalaya River flood on the oceanography of the Atchafalaya Shelf. *Cont. Shelf Res.* **2014**, *86*, 17–33. [[CrossRef](#)]
468. Sun, S.; Hu, C.; Garcia-Pineda, O.; Kourafalou, V.; Le Henaff, M.; Androulidakis, Y. Remote sensing assessment of oil spills near a damaged platform in the Gulf of Mexico. *Mar. Pollut. Bull.* **2018**, *136*, 141–151. [[CrossRef](#)]
469. Richey, J.E.; Mertes, L.A.; Dunne, T.; Victoria, R.L.; Forsberg, B.R.; Tancredi, A.C.; Oliveira, E. Sources and routing of the Amazon River flood wave. *Glob. Biogeochem. Cycles* **1989**, *3*, 191–204. [[CrossRef](#)]
470. Dunne, T.; Mertes, L.A.K.; Meade, R.H.; Richey, J.E.; Forsberg, B.R. Exchanges of sediment between the flood plain and channel of the Amazon River in Brazil. *Geol. Soc. Am. Bull.* **1998**, *110*, 450–467. [[CrossRef](#)]
471. Wilson, M.; Bates, P.; Alsdorf, D.; Forsberg, B.; Horritt, M.; Melack, J.; Frappart, F.; Famiglietti, J. Modeling large-scale inundation of Amazonian seasonally flooded wetlands. *Geophys. Res. Lett.* **2007**, *34*, L15404. [[CrossRef](#)]
472. Alsdorf, D.; Han, S.-C.; Bates, P.; Melack, J. Seasonal water storage on the Amazon floodplain measured from satellites. *Remote Sens. Environ.* **2010**, *114*, 2448–2456. [[CrossRef](#)]
473. Mertes, L.A.; Daniel, D.L.; Melack, J.M.; Nelson, B.; Martinelli, L.A.; Forsberg, B.R. Spatial patterns of hydrology, geomorphology, and vegetation on the floodplain of the Amazon River in Brazil from a remote sensing perspective. *Geomorphology* **1995**, *13*, 215–232. [[CrossRef](#)]
474. Trigg, M.A.; Wilson, M.D.; Bates, P.D.; Horritt, M.S.; Alsdorf, D.E.; Forsberg, B.R.; Vega, M.C. Amazon flood wave hydraulics. *J. Hydrol.* **2009**, *374*, 92–105. [[CrossRef](#)]
475. Park, E.; Latrubesse, E.M. The hydro-geomorphologic complexity of the lower Amazon River floodplain and hydrological connectivity assessed by remote sensing and field control. *Remote Sens. Environ.* **2017**, *198*, 321–332. [[CrossRef](#)]
476. Collischonn, B.; Collischonn, W.; Tucci, C.E.M. Daily hydrological modeling in the Amazon basin using TRMM rainfall estimates. *J. Hydrol.* **2008**, *360*, 207–216. [[CrossRef](#)]
477. Peixoto, J.M.A.; Nelson, B.W.; Wittmann, F. Spatial and temporal dynamics of river channel migration and vegetation in central Amazonian white-water floodplains by remote-sensing techniques. *Remote Sens. Environ.* **2009**, *113*, 2258–2266. [[CrossRef](#)]
478. Azarderakhsh, M.; Rossow, W.B.; Papa, F.; Norouzi, H.; Khanbilvardi, R. Diagnosing water variations within the Amazon basin using satellite data. *J. Geophys. Res. Atmos.* **2011**, *116*, D24107. [[CrossRef](#)]
479. Cao, M.K.; Marshall, S.; Gregson, K. Global carbon exchange and methane emissions from natural wetlands: Application of a process-based model. *J. Geophys. Res. Atmos.* **1996**, *101*, 14399–14414. [[CrossRef](#)]
480. Granberg, G.; Mikkela, C.; Sundh, I.; Svensson, B.H.; Nilsson, M. Sources of spatial variation in methane emission from mires in northern Sweden: A mechanistic approach in statistical modeling. *Glob. Biogeochem. Cycles* **1997**, *11*, 135–150. [[CrossRef](#)]
481. Potter, C.S. An ecosystem simulation model for methane production and emission from wetlands. *Glob. Biogeochem. Cycles* **1997**, *11*, 495–506. [[CrossRef](#)]
482. Walter, B.P.; Heimann, M. A process-based, climate-sensitive model to derive methane emissions from natural wetlands: Application to five wetland sites, sensitivity to model parameters, and climate. *Glob. Biogeochem. Cycles* **2000**, *14*, 745–765. [[CrossRef](#)]
483. Bartlett, K.B.; Crill, P.M.; Sebacher, D.I.; Harriss, R.C.; Wilson, J.O.; Melack, J.M. Methane flux from the central Amazonian floodplain. *J. Geophys. Res.* **1988**, *93*, 1571–1582. [[CrossRef](#)]
484. Melack, J.M.; Hess, L.L.; Gastil, M.; Forsberg, B.R.; Hamilton, S.K.; Lima, I.B.T.; Novo, E. Regionalization of methane emissions in the Amazon Basin with microwave remote sensing. *Glob. Change Biol.* **2004**, *10*, 530–544. [[CrossRef](#)]
485. Frappart, F.; Seyler, F.; Martinez, J.M.; Leon, J.G.; Cazenave, A. Floodplain water storage in the Negro River basin estimated from microwave remote sensing of inundation area and water levels. *Remote Sens. Environ.* **2005**, *99*, 387–399. [[CrossRef](#)]
486. Bourrel, L.; Phillips, L.; Moreau, S. The dynamics of floods in the Bolivian Amazon Basin. *Hydrol. Process.* **2009**, *23*, 3161–3167. [[CrossRef](#)]
487. Hess, L.L.; Melack, J.M.; Affonso, A.G.; Barbosa, C.; Gastil-Buhl, M.; Novo, E.M.L.M. Wetlands of the lowland Amazon Basin: Extent, vegetative cover, and dual-season inundated area as mapped with JERS-1 synthetic aperture radar. *Wetlands* **2015**, *35*, 745–756. [[CrossRef](#)]
488. Kandus, P.; Gail Minotti, P.; Soledad Morandeira, N.; Grimson, R.; Gonzalez Trilla, G.; Belen Gonzalez, E.; San Martin, L.; Patricia Gayol, M. Remote sensing of wetlands in South America: Status and challenges. *Int. J. Remote Sens.* **2018**, *39*, 993–1016. [[CrossRef](#)]
489. Jenson, S.K.; Domingue, J.O. Extracting Topographic Structure from Digital Elevation Data for Geographic Information-System Analysis. *Photogramm. Eng. Remote Sens.* **1988**, *54*, 1593–1600.
490. Brauer, M.; Hoek, G.; van Vliet, P.; Meliefste, K.; Fischer, P.; Gehring, U.; Heinrich, J.; Cyrus, J.; Bellander, T.; Lewne, M.; et al. Estimating long-term average particulate air pollution concentrations: Application of traffic indicators and geographic information systems. *Epidemiology* **2003**, *14*, 228–239. [[CrossRef](#)] [[PubMed](#)]
491. Sieber, R. Public Participation Geographic Information Systems: A Literature Review and Framework. *Ann. Assoc. Am. Geogr.* **2006**, *96*, 491–507. [[CrossRef](#)]